

The IceCube Neutrino Observatory

Contributions to ICRC 2017 Part III: Cosmic Rays

Contents

1 Combined Analysis of Cosmic-Ray Anisotropy with IceCube and HAWC		
PoS (ICRC2017) 539		arXiv:1708.03005
2 Search for PeV Gamma-Ray Point Sources with IceCube		6
PoS (ICRC2017) 715		
3 Search for diffuse gamma-ray emission from the Galactic plane with IceCube — PoS (ICRC2017) 705		14
4 A composition sensitive log-likelihood ratio for cosmic rays and gamma rays — PoS (ICRC2017) 514		22
5 Cosmic-Ray Anisotropy with Seven Years of Data from IceCube and IceTop		30
PoS (ICRC2017) 474		
6 Sensitivity of IceCube Cosmic-Ray measurements to the hadronic interaction models — PoS (ICRC2017) 319		38
7 GeV Solar Energetic Particle Observation and Search by IceTop from 2011 to 2016 — PoS (ICRC2017) 132		46
8 Impulsive Increase of Galactic Cosmic Ray Flux Observed by IceTop		54
PoS (ICRC2017) 133		
9 Performance of IceTop as a veto for IceCube — PoS (ICRC2017) 967		61
10 Solar atmospheric neutrino search with IceCube — PoS (ICRC2017) 965		69
11 High-Energy Atmospheric Muons in IceCube and IceTop		77
PoS (ICRC2017) 317		

35th International Cosmic Ray Conference — ICRC2017
10–20 July, 2017
Bexco, Busan, Korea

IceCube Collaboration Member List

M. G. Aartsen², M. Ackermann⁵², J. Adams¹⁶, J. A. Aguilar¹², M. Ahlers²⁰, M. Ahrens⁴⁴, I. Al Samarai²⁵, D. Altmann²⁴, K. Andeen³³, T. Anderson⁴⁹, I. Anseau¹², G. Anton²⁴, C. Argüelles¹⁴, J. Auffenberg¹, S. Axani¹⁴, H. Bagherpour¹⁶, X. Bai⁴¹, J. P. Barron²³, S. W. Barwick²⁷, V. Baum³², R. Bay⁸, J. J. Beatty^{18,19}, J. Becker Tjus¹¹, K.-H. Becker⁵¹, S. BenZvi⁴³, D. Berley¹⁷, E. Bernardini⁵², D. Z. Besson²⁸, G. Binder^{9,8}, D. Bindig⁵¹, E. Blaufuss¹⁷, S. Blot⁵², C. Boehm⁴⁴, M. Börner²¹, F. Bos¹¹, D. Bose⁴⁶, S. Böser³², O. Botner⁵⁰, J. Bourbeau³¹, F. Bradascio⁵², J. Braun³¹, L. Brayeur¹³, M. Brenzke¹, H.-P. Bretz⁵², S. Bron²⁵, J. Brostean-Kaiser⁵², A. Burgman⁵⁰, T. Carver²⁵, J. Casey³¹, M. Casier¹³, E. Cheung¹⁷, D. Chirkin³¹, A. Christov²⁵, K. Clark²⁹, L. Classen³⁶, S. Coenders³⁵, G. H. Collin¹⁴, J. M. Conrad¹⁴, D. F. Cowen^{49,48}, R. Cross⁴³, M. Day³¹, J. P. A. M. de André²², C. De Clercq¹³, J. J. DeLaunay⁴⁹, H. Dembinski³⁷, S. De Ridder²⁶, P. Desiati³¹, K. D. de Vries¹³, G. de Wasseige¹³, M. de With¹⁰, T. DeYoung²², J. C. Díaz-Vélez³¹, V. di Lorenzo³², H. Dujmovic⁴⁶, J. P. Dumm⁴⁴, M. Dunkman⁴⁹, B. Eberhardt³², T. Ehrhardt³², B. Eichmann¹¹, P. Eller⁴⁹, P. A. Evenson³⁷, S. Fahey³¹, A. R. Fazely⁷, J. Felde¹⁷, K. Filimonov⁸, C. Finley⁴⁴, S. Flis⁴⁴, A. Franckowiak⁵², E. Friedman¹⁷, T. Fuchs²¹, T. K. Gaisser³⁷, J. Gallagher³⁰, L. Gerhardt⁹, K. Ghorbani³¹, W. Giang²³, T. Glauch¹, T. Glüsenskamp²⁴, A. Goldschmidt⁹, J. G. Gonzalez³⁷, D. Grant²³, Z. Griffith³¹, C. Haack¹, A. Hallgren⁵⁰, F. Halzen³¹, K. Hanson³¹, D. Hebecker¹⁰, D. Heereman¹², K. Helbing⁵¹, R. Hellauer¹⁷, S. Hickford⁵¹, J. Hignight²², G. C. Hill², K. D. Hoffman¹⁷, R. Hoffmann⁵¹, B. Hokanson-Fasig³¹, K. Hoshina^{31,a}, F. Huang⁴⁹, M. Huber³⁵, K. Hultqvist⁴⁴, M. Hünnefeld²¹, S. In⁴⁶, A. Ishihara¹⁵, E. Jacobi⁵², G. S. Japaridze⁵, M. Jeong⁴⁶, K. Jero³¹, B. J. P. Jones⁴, P. Kalaczynski¹, W. Kang⁴⁶, A. Kappes³⁶, T. Karg⁵², A. Karle³¹, U. Katz²⁴, M. Kauer³¹, A. Keivani⁴⁹, J. L. Kelley³¹, A. Kheirandish³¹, J. Kim⁴⁶, M. Kim¹⁵, T. Kintscher⁵², J. Kiryluk⁴⁵, T. Kittler²⁴, S. R. Klein^{9,8}, G. Kohnen³⁴, R. Koirala³⁷, H. Kolanoski¹⁰, L. Köpke³², C. Kopper²³, S. Kopper⁴⁷, J. P. Koschinsky¹, D. J. Koskinen²⁰, M. Kowalski^{10,52}, K. Krings³⁵, M. Kroll¹¹, G. Krückl³², J. Kunnen¹³, S. Kunwar⁵², N. Kurahashi⁴⁰, T. Kuwabara¹⁵, A. Kyriacou², M. Labare²⁶, J. L. Lanfranchi⁴⁹, M. J. Larson²⁰, F. Lauber⁵¹, D. Lennarz²², M. Lesiak-Bzdak⁴⁵, M. Leuermann¹, Q. R. Liu³¹, L. Lu¹⁵, J. Lünemann¹³, W. Luszczak³¹, J. Madsen⁴², G. Maggi¹³, K. B. M. Mahn²², S. Mancina³¹, R. Maruyama³⁸, K. Mase¹⁵, R. Maunu¹⁷, F. McNally³¹, K. Meagher¹², M. Medici²⁰, M. Meier²¹, T. Menne²¹, G. Merino³¹, T. Meures¹², S. Miarecki^{9,8}, J. Micallef²², G. Momenté³², T. Montaruli²⁵, R. W. Moore²³, M. Moulai¹⁴, R. Nahnauer⁵², P. Nakarmi⁴⁷, U. Naumann⁵¹, G. Neer²², H. Niederhausen⁴⁵, S. C. Nowicki²³, D. R. Nygren⁹, A. Obertacke Pollmann⁵¹, A. Olivás¹⁷, A. O'Murchadha¹², T. Palczewski^{9,8}, H. Pandya³⁷, D. V. Pankova⁴⁹, P. Peiffer³², J. A. Pepper⁴⁷, C. Pérez de los Heros⁵⁰, D. Pieloth²¹, E. Pinat¹², M. Plum³³, P. B. Price⁸, G. T. Przybylski⁹, C. Raab¹², L. Rädcl¹, M. Rameez²⁰, K. Rawlins³, I. C. Rea³⁵, R. Reimann¹, B. Relethford⁴⁰, M. Relich¹⁵, E. Resconi³⁵, W. Rhode²¹, M. Richman⁴⁰, S. Robertson², M. Rongen¹, C. Rott⁴⁶, T. Ruhe²¹, D. Ryckbosch²⁶, D. Rysewyk²², T. Sälzer¹, S. E. Sanchez Herrera²³, A. Sandrock²¹, J. Sandroos³², S. Sarkar^{20,39}, S. Sarkar²³, K. Satalecka⁵², P. Schlunder²¹, T. Schmidt¹⁷, A. Schneider³¹, S. Schoenen¹, S. Schöneberg¹¹, L. Schumacher¹, D. Seckel³⁷, S. Seunarine⁴², J. Soedingrekso²¹, D. Soldin⁵¹, M. Song¹⁷, G. M. Spiczak⁴²,

C. Spiering⁵², J. Stachurska⁵², M. Stamatikos¹⁸, T. Stanev³⁷, A. Stasik⁵², J. Stettner¹, A. Steuer³², T. Stezelberger⁹, R. G. Stokstad⁹, A. Stöbl¹⁵, N. L. Strotjohann⁵², G. W. Sullivan¹⁷, M. Sutherland¹⁸, I. Taboada⁶, J. Tatar^{9,8}, F. Tenholt¹¹, S. Ter-Antonyan⁷, A. Terliuk⁵², G. Tešić⁴⁹, S. Tilav³⁷, P. A. Toale⁴⁷, M. N. Tobin³¹, S. Toscano¹³, D. Tosi³¹, M. Tselengidou²⁴, C. F. Tung⁶, A. Turcati³⁵, C. F. Turley⁴⁹, B. Ty³¹, E. Unger⁵⁰, M. Usner⁵², J. Vandenbroucke³¹, W. Van Driessche²⁶, N. van Eijndhoven¹³, S. Vanheule²⁶, J. van Santen⁵², M. Vehring¹, E. Vogel¹, M. Vraeghe²⁶, C. Walck⁴⁴, A. Wallace², M. Wallraff¹, F. D. Wandler²³, N. Wandkowsky³¹, A. Waza¹, C. Weaver²³, M. J. Weiss⁴⁹, C. Wendt³¹, J. Werthebach²¹, S. Westerhoff³¹, B. J. Whelan², S. Wickmann¹, K. Wiebe³², C. H. Wiebusch¹, L. Wille³¹, D. R. Williams⁴⁷, L. Wills⁴⁰, M. Wolf³¹, J. Wood³¹, T. R. Wood²³, E. Woolsey²³, K. Woschnagg⁸, D. L. Xu³¹, X. W. Xu⁷, Y. Xu⁴⁵, J. P. Yanez²³, G. Yodh²⁷, S. Yoshida¹⁵, T. Yuan³¹, M. Zoll⁴⁴

¹III. Physikalisches Institut, RWTH Aachen University, D-52056 Aachen, Germany

²Department of Physics, University of Adelaide, Adelaide, 5005, Australia

³Dept. of Physics and Astronomy, University of Alaska Anchorage, 3211 Providence Dr., Anchorage, AK 99508, USA

⁴Dept. of Physics, University of Texas at Arlington, 502 Yates St., Science Hall Rm 108, Box 19059, Arlington, TX 76019, USA

⁵CTSPS, Clark-Atlanta University, Atlanta, GA 30314, USA

⁶School of Physics and Center for Relativistic Astrophysics, Georgia Institute of Technology, Atlanta, GA 30332, USA

⁷Dept. of Physics, Southern University, Baton Rouge, LA 70813, USA

⁸Dept. of Physics, University of California, Berkeley, CA 94720, USA

⁹Lawrence Berkeley National Laboratory, Berkeley, CA 94720, USA

¹⁰Institut für Physik, Humboldt-Universität zu Berlin, D-12489 Berlin, Germany

¹¹Fakultät für Physik & Astronomie, Ruhr-Universität Bochum, D-44780 Bochum, Germany

¹²Université Libre de Bruxelles, Science Faculty CP230, B-1050 Brussels, Belgium

¹³Vrije Universiteit Brussel (VUB), Dienst ELEM, B-1050 Brussels, Belgium

¹⁴Dept. of Physics, Massachusetts Institute of Technology, Cambridge, MA 02139, USA

¹⁵Dept. of Physics and Institute for Global Prominent Research, Chiba University, Chiba 263-8522, Japan

¹⁶Dept. of Physics and Astronomy, University of Canterbury, Private Bag 4800, Christchurch, New Zealand

¹⁷Dept. of Physics, University of Maryland, College Park, MD 20742, USA

¹⁸Dept. of Physics and Center for Cosmology and Astro-Particle Physics, Ohio State University, Columbus, OH 43210, USA

¹⁹Dept. of Astronomy, Ohio State University, Columbus, OH 43210, USA

²⁰Niels Bohr Institute, University of Copenhagen, DK-2100 Copenhagen, Denmark

²¹Dept. of Physics, TU Dortmund University, D-44221 Dortmund, Germany

²²Dept. of Physics and Astronomy, Michigan State University, East Lansing, MI 48824, USA

²³Dept. of Physics, University of Alberta, Edmonton, Alberta, Canada T6G 2E1

²⁴Erlangen Centre for Astroparticle Physics, Friedrich-Alexander-Universität Erlangen-Nürnberg,

D-91058 Erlangen, Germany

²⁵Département de physique nucléaire et corpusculaire, Université de Genève, CH-1211 Genève, Switzerland

²⁶Dept. of Physics and Astronomy, University of Gent, B-9000 Gent, Belgium

²⁷Dept. of Physics and Astronomy, University of California, Irvine, CA 92697, USA

²⁸Dept. of Physics and Astronomy, University of Kansas, Lawrence, KS 66045, USA

²⁹SNOLAB, 1039 Regional Road 24, Creighton Mine 9, Lively, ON, Canada P3Y 1N2

³⁰Dept. of Astronomy, University of Wisconsin, Madison, WI 53706, USA

³¹Dept. of Physics and Wisconsin IceCube Particle Astrophysics Center, University of Wisconsin, Madison, WI 53706, USA

³²Institute of Physics, University of Mainz, Staudinger Weg 7, D-55099 Mainz, Germany

³³Department of Physics, Marquette University, Milwaukee, WI, 53201, USA

³⁴Université de Mons, 7000 Mons, Belgium

³⁵Physik-department, Technische Universität München, D-85748 Garching, Germany

³⁶Institut für Kernphysik, Westfälische Wilhelms-Universität Münster, D-48149 Münster, Germany

³⁷Bartol Research Institute and Dept. of Physics and Astronomy, University of Delaware, Newark, DE 19716, USA

³⁸Dept. of Physics, Yale University, New Haven, CT 06520, USA

³⁹Dept. of Physics, University of Oxford, 1 Keble Road, Oxford OX1 3NP, UK

⁴⁰Dept. of Physics, Drexel University, 3141 Chestnut Street, Philadelphia, PA 19104, USA

⁴¹Physics Department, South Dakota School of Mines and Technology, Rapid City, SD 57701, USA

⁴²Dept. of Physics, University of Wisconsin, River Falls, WI 54022, USA

⁴³Dept. of Physics and Astronomy, University of Rochester, Rochester, NY 14627, USA

⁴⁴Oskar Klein Centre and Dept. of Physics, Stockholm University, SE-10691 Stockholm, Sweden

⁴⁵Dept. of Physics and Astronomy, Stony Brook University, Stony Brook, NY 11794-3800, USA

⁴⁶Dept. of Physics, Sungkyunkwan University, Suwon 440-746, Korea

⁴⁷Dept. of Physics and Astronomy, University of Alabama, Tuscaloosa, AL 35487, USA

⁴⁸Dept. of Astronomy and Astrophysics, Pennsylvania State University, University Park, PA 16802, USA

⁴⁹Dept. of Physics, Pennsylvania State University, University Park, PA 16802, USA

⁵⁰Dept. of Physics and Astronomy, Uppsala University, Box 516, S-75120 Uppsala, Sweden

⁵¹Dept. of Physics, University of Wuppertal, D-42119 Wuppertal, Germany

⁵²DESY, D-15738 Zeuthen, Germany

^aEarthquake Research Institute, University of Tokyo, Bunkyo, Tokyo 113-0032, Japan

Acknowledgment: The authors gratefully acknowledge the support from the following agencies and institutions: USA - U.S. National Science Foundation-Office of Polar Programs, U.S. National Science Foundation-Physics Division, University of Wisconsin Alumni Research Foundation, the Center for High Throughput Computing (CHTC) at the University of Wisconsin - Madison, the Open Science Grid (OSG) grid infrastructure and the Extreme Science and Engineering Discovery Environment (XSEDE); U.S. Department of Energy, and National Energy Research Scientific Computing Center; Particle Astrophysics research computing center at the University of Maryland; Institute for Cyber-Enabled Research at Michigan State University; Astroparticle Physics Computational Facility at Marquette University; Belgium - Funds for Scientific Research (FRS-FNRS and FWO), FWO Odysseus and Big Science programs, Belgian Federal Science Policy Office (Belspo); Germany - Bundesministerium für Bildung und Forschung (BMBF), Deutsche Forschungsgemeinschaft (DFG), Helmholtz Alliance for Astroparticle Physics (HAP), Initiative and Networking Fund of the Helmholtz Association; Deutsches Elektronen Synchrotron (DESY); Cluster of Excellence (PRISMA ? EXC 1098); High Performance Computing Cluster of the IT-Center of the RWTH Aachen; Sweden - Swedish Research Council, Swedish Polar Research Secretariat, Swedish National Infrastructure for Computing (SNIC), and Knut and Alice Wallenberg Foundation; Canada - Natural Sciences and Engineering Research Council of Canada, Calcul Québec, Compute Ontario, WestGrid and Compute Canada; Denmark - Villum Fonden, Danish National Research Foundation (DNRF); New Zealand - Marsden Fund, New Zealand; Australian Research Council; Japan - Japan Society for Promotion of Science (JSPS) and Institute for Global Prominent Research (IGPR) of Chiba University; Korea - National Research Foundation of Korea (NRF); Switzerland - Swiss National Science Foundation (SNSF).

Search for PeV Gamma-Ray Point Sources with IceCube

The IceCube Collaboration[†]

[†] http://icecube.wisc.edu/collaboration/authors/icrc17_icecube

E-mail: zachary.griffith@icecube.wisc.edu

We present results of a search for PeV gamma-ray point sources with the IceCube Neutrino Observatory, presently the most sensitive facility for PeV gamma-ray sources in the southern hemisphere. This includes a general search over IceCube's field of view, as well as tests for correlations with TeV sources detected by H.E.S.S. and neutrino events from IceCube's high-energy starting event sample. As the attenuation length of PeV gamma rays limits observational distances to within the Galaxy, one of the goals of the analysis is to constrain the Galactic component of the astrophysical neutrino flux observed by IceCube.

Corresponding authors: Zachary Griffith^{*1}, Hershhal Pandya²

¹ *Wisconsin IceCube Particle Astrophysics Center (WIPAC) and Department of Physics, University of Wisconsin-Madison, Madison, WI 53706, USA*

² *Dept. of Physics and Astronomy, University of Delaware, Newark, DE 19711, USA.*

*35th International Cosmic Ray Conference — ICRC2017
10–20 July, 2017
Bexco, Busan, Korea*

^{*}Speaker.

1. Introduction

IceCube previously set the most stringent limit on PeV gamma-ray emission in the southern hemisphere at $(E/\text{TeV})^2 d\Phi/dE \approx 10^{-18} - 10^{-17} \text{ cm}^{-2}\text{s}^{-1}\text{TeV}^{-1}$ using one year of data taken with a partial detector during construction [1]. We present here an updated PeV gamma-ray analysis with IceCube using five years of data and an enhanced event selection. We use this analysis to perform an all-sky scan for point sources of PeV gamma rays as well as correlation tests with known Galactic TeV gamma-ray sources and IceCube's high-energy starting event (HESE) sample of neutrinos.

All known Galactic TeV gamma-ray sources in IceCube's field of view have been detected by the High Energy Stereoscopic System (H.E.S.S.) [2]. Of these sources, 15 have steady emission with no evidence of a spectral break or cutoff [3]. Of those with extended emission, none approach the median angular resolution of this analysis of $\sim 0.5^\circ$ and the sources are treated as point-like. Each source is treated individually in addition to a stacked catalog. This analysis is the first to test for a signal from these sources at higher energies, and an extension up to PeV energies from many of these sources can be constrained by this analysis.

If the HESE neutrinos include a galactic component, an associated PeV gamma-ray flux has been predicted by several studies ([4], [5]). This is due to the fact that the same hadronic interactions that produce PeV neutrinos most likely also produce gamma rays from the decay of neutral pions. However, PeV gamma rays can only be observed over Galactic distances due to pair-production with the cosmic microwave background (CMB) radiation field [6]. Therefore, a measurement or limit on the flux of gamma rays at PeV energies constrains the Galactic component of the neutrino flux observed by IceCube.

2. Dataset

The IceCube Neutrino Observatory, located at the geographic South Pole, is comprised of two components. The cubic-kilometer neutrino detector IceCube [7] is installed in the ice between depths of 1450 m and 2450 m. Its companion surface air shower array, IceTop [8], is located on top of the ice sheet, corresponding to an altitude of 2835 meters above sea level. Both components were completed in 2011. This analysis uses IceTop data for event energy and direction, while both IceTop and IceCube information is used in the classification of gamma rays. The greatest difference between gamma-ray and hadronic air showers that IceCube is capable of exploiting is the number of muons present in the air shower. Gamma-ray air showers do have muons from the decay of pions and kaons due to photoproduction processes in addition to muon pair production [9]. However, these processes are three orders of magnitude more rare, per shower, than the nucleus-nucleus interactions which produce muons in hadronic showers [10].

To ensure good data quality (energy determination, angular resolution), the following cuts were applied. Good fits to the shower lateral distribution and core location are required for each event, and events are restricted to have passed inside the IceTop area. A zenith-dependent minimum energy cut of $\sim 0.6\text{-}0.7$ PeV is applied to ensure adequate trigger efficiency in IceTop, while a maximum energy cut of 100 PeV is set above which no Monte Carlo was simulated and where there are few events in data. A maximum zenith angle cut of $\sim 37^\circ$ is also applied.

After quality cuts, an additional event selection is applied to create an event sample rich in gamma rays. Features are selected in IceTop and IceCube that are correlated with muon content and shower age. These features are used in random forest classification to create the final event sample. The classification is implemented using the open source python software Scikit-learn [11].

IceCube is a muon detector, which means the total number of photoelectrons recorded in IceCube’s photomultipliers is proportional to the high-energy (>276 GeV) muons in the air shower for events coincident in IceTop and IceCube. Rather than a veto of all showers which have signal in IceCube as was done in Ref. [1], the number of photoelectrons is used as one parameter in a random forest classification, along with a parameter that describes the containment of the shower axis within IceCube.

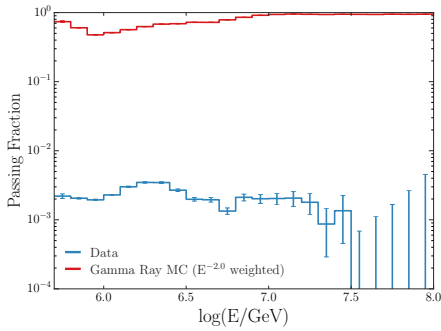


Figure 1: The fraction of events which pass the random forest classification cut from the quality cut level event sample for a section of data from the 2012 observing year and gamma-ray simulation weighted to an $E^{-2.0}$ spectrum and detector response using October 2012 snow heights.

Lower-energy muons that are laterally separate from the shower core produce a charge signature in IceTop tanks that is prominent for muon-rich cosmic-ray air showers. In addition, gamma-ray air showers interact deeper in the atmosphere than hadronic air showers, resulting in a difference in shower front curvature. The following is a brief description of the parameter developed to encapsulate this information.

Three sets of likelihood tables are constructed using information from hits in IceTop tanks: charge against distance from the shower core, hit time against distance from the shower core, and charge against time. Hadronic likelihood tables are built from data, rather than Monte Carlo simulation of cosmic rays, in order to abstain from making any composition assumption. Existing limits place the expected fraction of gamma rays to be less than 10^{-4} of the total cosmic ray flux [12], so the influence of signal events in the data is small.

Gamma-ray tables are built from Monte Carlo simulation of gamma rays. During event selection, the tank information of each event is used to sample from the likelihood tables and calculate a total likelihood from the hadronic shower hypothesis as well as the gamma-ray hypothesis. The parameter used for classification is the ratio of these total likelihoods, such that higher values indicate a more hadron-like shower. A full description of this technique is documented in Ref. [13]. Utilizing IceTop for event selection allows for the inclusion of events that do not pass through IceCube, which significantly boosts the acceptance to gamma rays for inclined showers.

The random forests are trained using experimental data as the background and Monte Carlo simulation of gamma rays as the signal. Two random forests were trained for this analysis: one using gamma-ray simulation weighted to an $E^{-2.0}$ spectrum and one with simulation weighted to $E^{-2.7}$. These comprise reasonable bounds for an observable point source in the dataset. The final event sample consists of data events with a random forest score of greater than 0.7 in either of the classifiers. The fraction of data and gamma-ray simulation that survive from the quality cut event samples after applying the random forest cut is shown in Fig. 1.

Five years of data from the completed detector are included in the dataset, from May 2011 to

May 2016. Snow has continuously accumulated on the IceTop tanks over this time, which attenuates the electromagnetic component of air showers, significantly decreasing the effective area to gamma rays. Snow measurements are performed twice per year to account for the effect on IceTop data. In order to account for these variations over time, the detector response to simulated gamma-rays was repeated for each year of data, with the fall measurement of snow used as the simulated IceTop snow heights. Classifiers are trained for each year of data and dedicated simulation independently. The complete dataset at the final cut level is comprised of a total livetime of 1,576 days and 471,461 events.

3. Search Methods

The following section describes the statistical methods and three different source hypotheses tested in this analysis. We use a maximum likelihood test with the following likelihood function

$$L = \prod_i \prod_{j \in i} \left(\frac{n_s^j}{N} S(|\mathbf{x}_j - \mathbf{x}_S|, E_j, \sigma_j; \gamma) + \left(1 - \frac{n_s^j}{N}\right) B(\delta_j, E_j) \right). \quad (3.1)$$

This likelihood L is a product over j events in each of i datasets, where each dataset is comprised of one year of data. Each event has a direction \mathbf{x}_j (including declination δ_j), energy E_j , and angular uncertainty σ_j . The events are compared to a point-source hypothesis comprised of a direction \mathbf{x}_S and a spectral index γ . The terms S and B are the signal and background probability distribution functions (PDFs), respectively. For the all-sky scan they are defined as:

$$S_i = \frac{1}{2\pi\sigma_i^2} e^{-\frac{|\mathbf{x}_j - \mathbf{x}_S|^2}{2\sigma_i^2}} \mathcal{E}_{S,i}(E_i, \delta_i, \gamma) \quad \text{and} \quad B_i = \frac{1}{2\pi} B_{\text{exp}}(\delta_i) \mathcal{E}_{B,i}(E_i, \delta_i), \quad (3.2)$$

where a Gaussian uncertainty is assumed for the signal PDF, B_{exp} is the spatial acceptance to cosmic rays derived from data, and $\mathcal{E}_{S,i}, \mathcal{E}_{B,i}$ are the normalized energy distributions for signal and background, respectively. The background PDF is uniform in right ascension and constructed from data.

To test for a correlation with H.E.S.S. sources in the analysis field of view, the signal PDF is modified to include M source locations each with a Gaussian uncertainty that is event dependent:

$$S_i = \frac{\sum_m^M \frac{R(\delta_m)}{2\pi\sigma_i^2} e^{-\frac{|\mathbf{x}_j - \mathbf{x}_S|^2}{2\sigma_i^2}}}{\sum_m^M R(\delta_m)}, \quad (3.3)$$

where R_m is the relative detector acceptance to gamma rays at the location of the source m .

To test for a correlation with IceCube HESE sample of neutrinos, the event sample is split into "cascade"-like events, which have relatively poor angular resolution ($\sim 8^\circ$ - 10°), and "track"-like events with angular resolution $< 1.2^\circ$. There are a total of 11 events in the 4-year HESE sample [14] with a reconstructed direction (within 1σ uncertainty) within the field of view of this analysis. Of those, 10 are cascade events, with a single "track"-like event at a declination of $\delta = -86.77^\circ$. The single track event is treated as a source with the signal PDF reformulated to be:

$$S_i = \frac{1}{2\pi\sigma_{i,S}^2} e^{-\frac{|x_j - x_S|^2}{2\sigma_{i,S}^2}} \mathcal{E}_{S,i}(E_i, \delta_i, \gamma) \quad \text{and} \quad \sigma_{i,S} = \sqrt{\sigma_i^2 + \sigma_S^2}, \quad (3.4)$$

where σ_S is the angular uncertainty of the track event.

As the cascade events have large angular uncertainties, to properly account for the change in acceptance over the field of view a template likelihood method is used. The template is constructed by defining each cascade event to have a signal PDF as Eq. 3.4. These signal PDFs are combined and renormalized to form a signal template, which is then convolved with the detector acceptance to gamma rays. A full description of the template likelihood method is included in [15].

In all cases, the likelihood is maximized in n_s and γ , and the ratio of the optimal likelihood to the null hypothesis ($n_s = 0$) yields the test statistic. To model the expected output of background-only events this process is repeated many times, with each trial using a random (scrambled) set of right ascension values. The p-value of an observed test statistic is then obtained from a comparison to the ensemble of test statistic values returned by the background trials.

4. Results

4.1 All-Sky Point Source Search

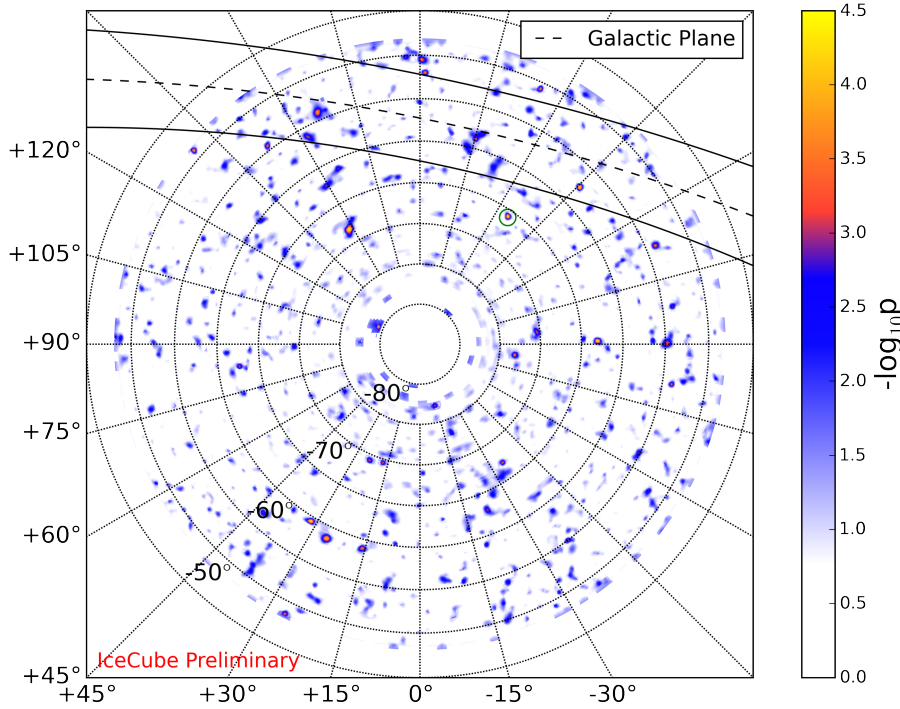


Figure 2: An equatorial polar map of the all-sky scan pre-trial p-values. The solid and dashed black line represents the Galactic plane region $\pm 10^\circ$. The location of the lowest p-value is circled in green.

The all sky search is accomplished by a scan over each pixel in a HEALPIX [16] map ($n_{\text{side}}=512$) with a pixel diameter of $\sim 0.11^\circ$. For each pixel, the test statistic is evaluated given a source hy-

pothesis at the position of the pixel. Fig. 2 shows the results of the all-sky point source search over the entire field of view, excluding the region within 5° of the pole where scrambling in right ascension is insufficient to build independent background trials. The color scale corresponds to a pre-trial p-value that for each position is determined through a comparison of the test statistic value of the true event locations to that of an ensemble of background trials, each with event locations scrambled in right ascension.

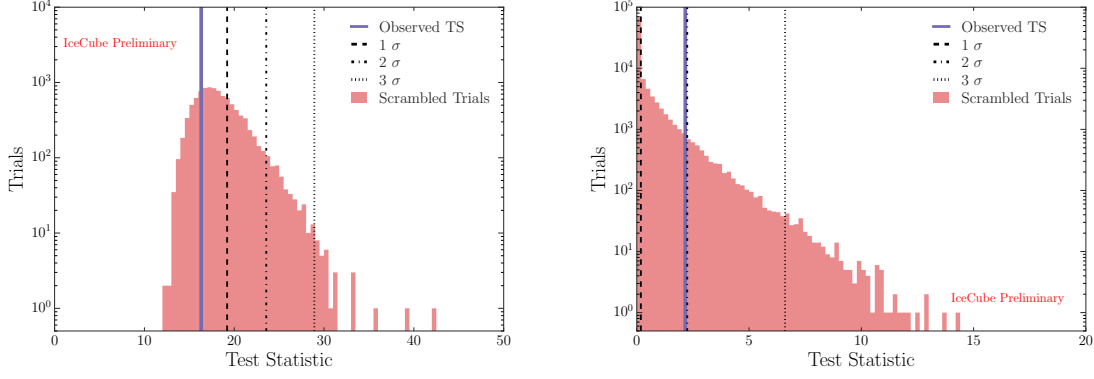


Figure 3: Left: the highest test statistic found in data compared to an ensemble of background scrambled trials. Right: result of a stacking analysis on the H.E.S.S. source catalog.

The cluster in the sky with the lowest p-value is at -70.9° declination and 214.7° right ascension, with $n_s = 24.03$, a spectral index of 1.87, and a test statistic of 16.32. Fig. 3 (left) shows this test statistic compared to a distribution of the highest test statistic in trials of right ascension scrambled event samples, which gives a post-trial p-value of 77.4%, compatible with background expectation.

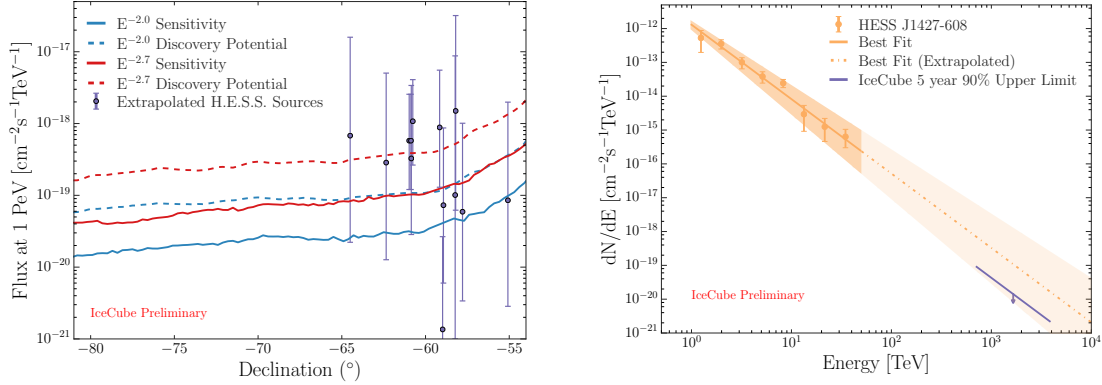


Figure 4: Left: sensitivity and discovery potential to $E^{-2.0}$ and $E^{-2.7}$ sources at 1 PeV. Shown in purple are the extrapolation up to 1 PeV of H.E.S.S. sources in the analysis field of view under an optimistic scenario of no energy spectrum breaks and zero absorption. Right: the measured and best fit flux of H.E.S.S. J1427-608 [17] along with the 90% upper limit set by this analysis.

4.2 H.E.S.S. Sources

Fig. 4 (left) shows the integral flux sensitivity and discovery potential as a function of decli-

nation for the full five-year sample, along with the extrapolated flux of H.E.S.S. sources assuming no break in the energy spectrum and no absorption from radiation fields. Recent modeling has shown Galactic sources can be significantly attenuated depending on the distance from Earth and line of sight proximity to the Galactic center [18]. The points therefore represent an optimistic flux prediction for each source. Not present on the plot are two sources, SNR G292.2-00.5 and SNR G318.2+00.1, which have no reported flux values. The sensitivity of this analysis is defined as the signal flux at which 90% of experiments yield a test statistic at or above the median of an ensemble of background-only trials. This is equivalent to the Neyman construction of 90% confidence level upper limits. The discovery potential is reached with a signal flux that achieves a 5σ post-trial p-value in 50% of experiments.

A particularly interesting source in the analysis field of view is H.E.S.S. J1427-608, which remains of an unidentified class. Guo et al. [19] reported on a counterpart seen in Fermi-LAT data at GeV energies with a best fit including H.E.S.S. data of E^{-2} over four orders of magnitude in energy with no break in the spectrum, a property unique among currently known TeV sources. The extrapolated, non-attenuated flux of the source H.E.S.S. J1427-608 is shown in Fig. 4 (right) as a function of energy along with the 90% integral flux upper limit set by this analysis, for which the energy bounds are the 5% and 95% quantiles of the data energy distribution. The upper limit set by this analysis rejects this optimistic scenario and can help constrain models of the source class.

Fig. 5 shows the H.E.S.S. sources included in this analysis, which were selected from the TeVCat catalog. The source with the lowest pre-trial p-value, H.E.S.S. J1026-582, has a post-trial p-value of 44.7%. A test statistic of 2.16 is returned by the stacking analysis, which is shown compared to the background trial test statistic distribution in Fig. 3 (right). The resulting p-value is 5.4%.

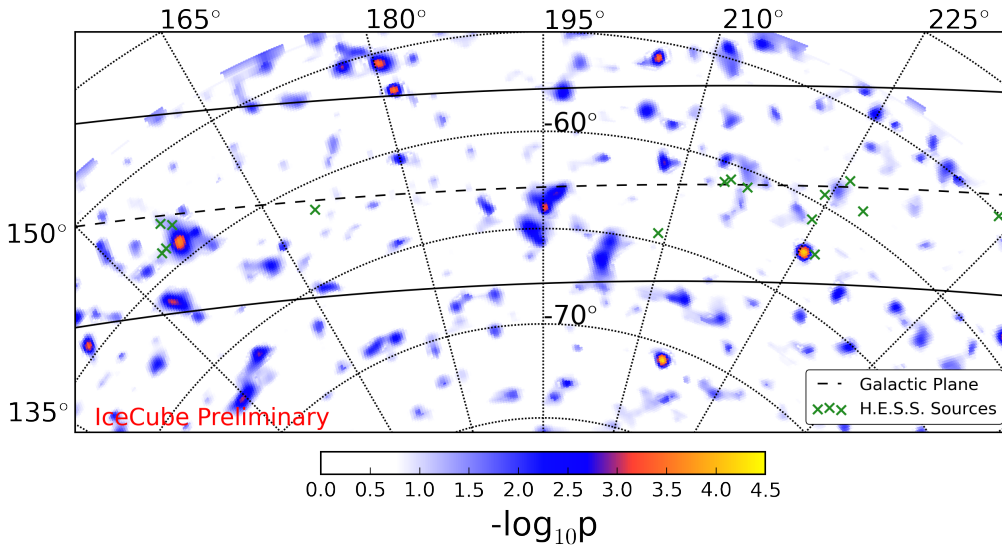


Figure 5: Map of p values from the all-sky scan with H.E.S.S. source directions overlaid.

4.3 Correlation with IceCube HESE Sample of Neutrinos

The cascade sample likelihood test returned a test statistic value of zero, which sets a lower bound on the p-value of 49% and is consistent with no signal. The track event lies within the polar cap region $\delta < -85^\circ$ where scrambling in right ascension only does not provide independent background trials. However, as the event rate as a function of $\sin(\delta)$ is quite flat within this region, events with $\delta < -85^\circ$ were scrambled in both right ascension and declination. The test statistic returned by the likelihood analysis is zero, again consistent with no signal. The lower bound on the p-value is 71%.

5. Summary

In this analysis, five years of data from IceTop and IceCube were used to search for PeV photons through maximum likelihood analyses: an all-sky scan, a correlation test with H.E.S.S. sources, and a correlation test with the IceCube 4-year HESE neutrino sample. For all cases, no evidence of significant signal was observed. The obtained sensitivity to point sources is the most stringent for PeV gamma rays yet reported. A search for a diffuse flux of PeV gamma rays correlated with the Galactic plane was also performed, which is covered in Ref. [15].

References

- [1] **IceCube** Collaboration, M. Aartsen *et al.*, *Phys. Rev. D* **13** (2013) 062002.
- [2] **H.E.S.S.** Collaboration, F. Aharonian *et al.*, *ApJ* **636** (2006) 777.
- [3] The TeVCat catalog, <http://tevcat.uchicago.edu>.
- [4] M. Ahlers and K. Murase, *Phys. Rev.* **D90** (2014) 023010.
- [5] N. Gupta, *Astropart. Phys.* **48** (2013) 75-77.
- [6] R. J. Protheroe and P. L. Biermann, *Astropart. Phys.* **6** (1996) 45.
- [7] **IceCube** Collaboration, M. Aartsen *et al.*, *JINST* **12** (2017) 03012.
- [8] **IceCube** Collaboration, R. Abbasi *et al.*, *NIM* **700** (2013) 188.
- [9] F. Halzen, A. Kappes, and A. Ó Murchadha, *Phys. Rev. D* **80** (2009) 083009.
- [10] **KASCADE** Collaboration, D. Kang *et al.*, *J. Phys.: Conf. Ser.* **632** (2015) 012013.
- [11] Pedregosa *et al.*, *JMLR* **12** (2011) 2825.
- [12] **CASA-MIA** Collaboration, A. Borione *et al.*, *ApJ* **493** (1998) 175.
- [13] **IceCube** Collaboration, **PoS (ICRC2017) 514** (these proceedings).
- [14] **IceCube** Collaboration, **PoS (ICRC2015) 1098** (2016).
- [15] **IceCube** Collaboration, **PoS (ICRC2017) 705** (these proceedings).
- [16] K. Gorski *et al.*, *Astrophys. J.* **622** (2005) 759.
- [17] **H.E.S.S.** Collaboration, F. Aharonian *et al.*, *A&A* **477** (2008) 353.
- [18] S. Vernetto, and P. Lipari, *EpJ* **136** (2017) 03015.
- [19] Guo *et al.*, *ApJ* **835** (2017) 42.

Search for diffuse gamma-ray emission from the Galactic plane with IceCube

The IceCube Collaboration[†]

[†] http://icecube.wisc.edu/collaboration/authors/icrc17_icecube

E-mail: hershal@udel.edu

We present a search for diffuse PeV gamma-rays arising from interactions of cosmic rays with the interstellar gas in the Galactic plane. We analyze air shower data recorded by the IceCube Observatory from May 2011 to May 2016 in the energy range of 0.6 PeV to 100 PeV for the presence of gamma-ray showers. Muon poor gamma-ray induced air showers are discriminated from the cosmic ray showers using the characteristics of signals recorded by IceTop as well as the in-ice IceCube array. We carry out an unbinned maximum likelihood analysis on the Galactic plane region ($270^\circ \lesssim l \lesssim 335^\circ$) located in the IceCube field of view. The pion decay component of the Fermi-LAT diffuse emission model is used as the spatial template for the analysis. No statistically significant evidence for diffuse gamma-ray emission was found. We derive an upper limit of $3.88 \times 10^{-9} \text{ GeV cm}^{-2} \text{ s}^{-1}$ (90% confidence limit) on the normalization of the spectral energy distribution at 2 PeV assuming an E^{-3} spectrum.

Corresponding authors: Hershhal Pandya^{*1}, Zachary Griffith²

¹*Dept. of Physics and Astronomy, University of Delaware, Newark, DE 19711, USA.*

²*Wisconsin IceCube Particle Astrophysics Center (WIPAC) and Department of Physics, University of Wisconsin-Madison, Madison, WI 53706, USA.*

*35th International Cosmic Ray Conference — ICRC2017
10–20 July, 2017
Bexco, Busan, Korea*

*Speaker.

1. Introduction

Cosmic ray interactions with the interstellar gas produce neutral pions that further decay into gamma-rays. Hence, high energy gamma-rays can be used for measuring the spectral density of the Galactic cosmic rays and probing their propagation. Diffuse gamma-ray emission from the Galactic plane has been measured up to TeV energies but it has not been observed in the PeV energy range. Along with the significant decrease in their flux as compared to TeV gamma-rays, there is yet another process that makes the observation of PeV gamma-rays challenging. PeV gamma-rays are significantly attenuated by interactions with the cosmic microwave background radiation. This limits the observable source distance to few tens of kiloparsecs [1] and hence within the Galaxy. The same cosmic ray interactions that are responsible for producing neutral pions, also produce charged pions that decay into neutrinos. Therefore, measurement of diffuse gamma-rays could also provide insight into a Galactic origin for some of the astrophysical neutrinos observed by IceCube [2, 3].

PeV gamma-rays can be detected via the extensive air showers of particles generated from their interaction with nuclei in the Earth's atmosphere. Air showers generated by photon primaries differ from cosmic ray air showers in their longitudinal shower development (shower age) as well as the muon content. Based on showers simulated using CORSIKA [4] with hadronic interaction models FLUKA [5] and SIBYLL 2.1 [6], cosmic ray showers have roughly ten times the number of GeV muons as compared to gamma-ray showers, whereas for muons with energy greater than 100 GeV this ratio increases to about a hundred. Photon showers are also younger since their shower maximum occurs deeper in the atmosphere than the cosmic ray showers. We use IceCube to measure these properties and discriminate gamma-ray showers from the highly abundant cosmic ray showers.

In search of diffuse gamma-ray emission from the Galactic plane, we carry out an unbinned maximum likelihood analysis. We improve upper limits on diffuse PeV gamma-ray emission at Galactic longitudes $270^\circ \lesssim l \lesssim 335^\circ$ by one order of magnitude.

2. Detector

IceCube [7], as shown in Fig. 1, is a cubic kilometer array of 5160 optical sensors arranged on 86 strings, embedded in the Antarctic ice at a depth between 1450 m to 2450 m under the surface. The strings have a horizontal spacing of 125 m with the optical sensors vertically separated by 17 m on each string. The optical sensors, digital optical modules (DOMs), detect Cherenkov radiation emitted by relativistic charged particles traversing the ice. The charged particles may be downward-going high energy muons from cosmic ray air showers or from neutrino interactions in the surrounding ice or the bedrock. IceCube has an additional component called IceTop, which is located on the surface at an altitude of 2835 m above sea level and triggers on extensive air showers. IceTop is sensitive to air showers from cosmic rays with primary energies in the range of 300 TeV to 1 EeV. It consists of 81 pairs of ice tanks that cover an area of about one square kilometer, with two DOMs within each tank. IceTop DOMs are calibrated using the vertical muons from low energy air showers and the signals are measured in units of vertical equivalent muons (VEM). The direction of the primary particle, the shower size, and the location of the shower core

on the surface, are reconstructed by simultaneously fitting a lateral distribution function (LDF) to measured charge depositions, and a shower curvature function to the signal times. The lateral distribution function, describing the signal distribution as a function of the lateral distance from the shower axis, is defined as

$$S(R) = S_{125} \left(\frac{R}{125 \text{ m}} \right)^{-\beta - 0.303 \log_{10} \left(\frac{R}{125 \text{ m}} \right)}, \quad (2.1)$$

where $S(R)$ is the signal measured at a lateral distance R from the shower axis, β is the slope of the logarithmic LDF at 125 m, and the signal measured at 125 m, S_{125} , is the shower size.

The energy of the primary particle is calculated by using a $\log_{10}(S_{125})$ to $\log_{10}(E)$ conversion obtained from simulated cosmic ray showers [8]. Snow accumulates on top of the IceTop tanks with time, and attenuation of the signal due to snow is accounted for while reconstructing the shower size [9].

3. Analysis

The current analysis can be divided into two parts: first an enriched sample of gamma-ray like events from the observed data is obtained. In a second step, this enriched sample is used for a maximum likelihood analysis to search for diffuse emission from the Galactic plane. We analyze air shower events recorded by IceCube between May 2011 and May 2016 with sufficient energy to trigger ten IceTop tanks or more. For identifying gamma-ray air showers, we rely on simulated showers generated using CORSIKA [4] with low- and high-energy hadronic interaction models FLUKA [5] and SIBYLL 2.1 [6], respectively. The detector response to gamma-ray showers was simulated for each of the five years with different snow heights on top of the tanks as recorded during October or November of each year. To avoid any bias and to maintain blindness to the source, the subsequent event selection as well as the maximum likelihood analysis was developed using only 10% of the available data. Various quality cuts were placed on both data as well as simulations to obtain a sample of well reconstructed air showers.

3.1 Event Selection

Using IceTop observables, we construct three two-dimensional probability distribution functions (PDFs) that incorporate different shower characteristics. For example, Fig. 2 shows the two-dimensional PDF constructed using the measured charge in tanks, and their lateral distance from the shower axis. This PDF represents the lateral distribution of charges. One of the important features in this PDF is the ~ 1 VEM signal due to GeV muons emerging at large lateral distances for cosmic ray showers (highlighted using dashed lines in Fig. 2). This feature is absent for the

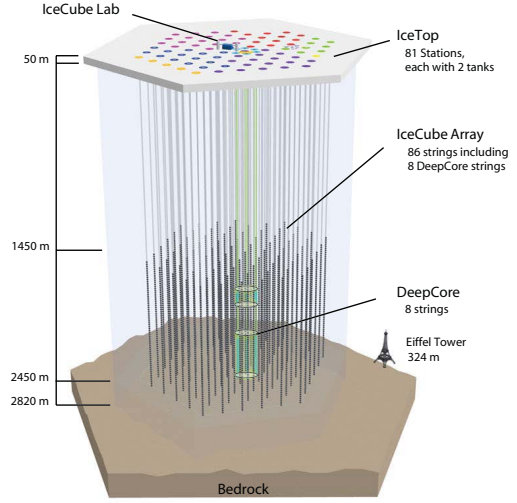


Figure 1: The IceCube Detector with its components DeepCore and IceTop.

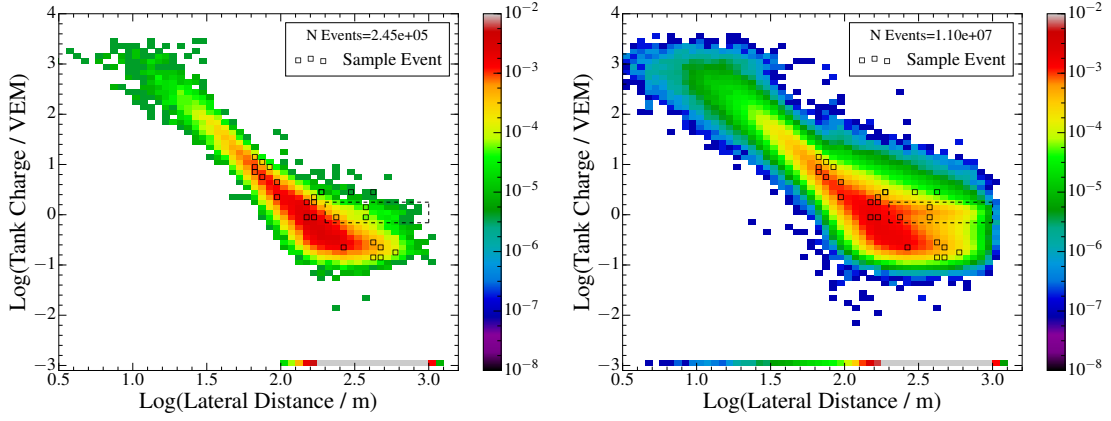


Figure 2: PDFs for photon (left) and cosmic ray (right) events, based on lateral distribution of charges, with $0.3 \leq \log_{10}(S_{125}) < 0.4$ and $0.9 \leq \cos(\theta) < 0.95$. Hit tanks for a typical cosmic-ray event are shown as hollow boxes and the signal due to GeV muons is highlighted using dashed lines.

gamma-ray showers. The likelihood defined as the product of probabilities for all tanks, is computed for each event, using either a gamma-ray or a cosmic ray shower PDF. A log-likelihood ratio is the difference of log-likelihoods obtained from gamma-ray and cosmic ray PDFs. A typical cosmic-ray event overlaid on the PDFs in Fig. 2, will have a large log-likelihood ratio due to contribution from the muon feature at large distances. Other features such as the steepness and thickness of the LDF, which correlate with the shower age and hadronic content, also contribute to the log-likelihood ratio. We calculate two more log-likelihood ratios for every event, from PDFs based on the time distribution of charges and the shower front shape [10]. All three ratios are added to form a single variable, IceTop LLH ratio, used in the final event selection.

For coincident events with the reconstructed axis passing through the in-ice detector, the measurement of IceCube charges provides a strong handle on the number of high energy muons. High energy muons ($E_\mu > 300$ GeV) can reach deep inside the ice and deposit energy in DOMs via radiation from ionization losses, stochastic losses, as well as direct Cherenkov radiation. To estimate the energy deposited by muons, cleaned in-ice charge is computed by adding charges from selected DOMs. The selection of DOMs is optimized to remove hits uncorrelated to air shower muons. The quality of separation from both, IceTop LLH ratio and cleaned in-ice charges, increases with increasing shower size (primary energy), as shown in Fig. 3.

Events with reconstructed zenith angle $0^\circ < \theta < 37^\circ$, and reconstructed energy between 0.6 PeV and 100 PeV, are included in the current analysis. The event selection was done by using a random forest algorithm trained to discriminate gamma-ray events from cosmic ray events. The machine learning algorithm was implemented using the open source python package scikit-learn [11]. The random forest was trained using the following features: IceTop LLH ratio, cleaned in-ice charge, S_{125} , zenith angle, and a measure of geometric containment of the shower track in IceCube. Gamma-ray events used for training were weighted according to an E^{-3} spectrum. Finally, signal and background events with a classifier score above a cut value were used for the maximum likelihood analysis. Of all the selected events, 5% of the events are below 0.68 PeV,

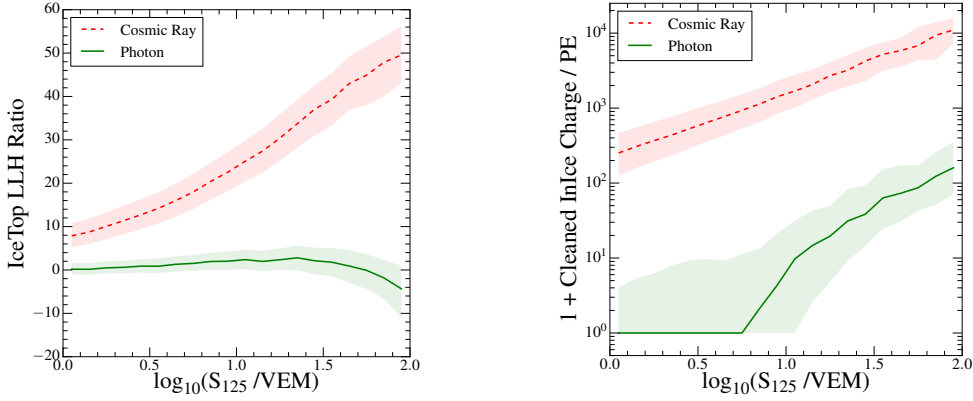


Figure 3: IceTop LLH ratio as a function of $\log_{10}(S_{125})$ for all events (left). Cleaned in-ice charge as a function of $\log_{10}(S_{125})$ for coincident events (right). Shaded regions delimit 50% of the distribution around the median.

and 95% of the events are below 2.73 PeV. Roughly 0.2% of the background events pass the cut between 0.68 PeV and 2.73 PeV while retaining 57% of the signal events.

3.2 Unbinned Maximum Likelihood Analysis

We implement a modified version of the usual unbinned likelihood analysis [12] that utilizes a spatial template for the expected diffuse signal and depends on constructing the background hypothesis from observed data. The usual likelihood function is defined as

$$L(n_s, \gamma) = \prod_{i=1}^N \left(\frac{n_s}{N} S_i(\mathbf{x}_i, \sigma_i, E_i; \gamma) + \left(1 - \frac{n_s}{N}\right) B_i(\sin \delta_i, E_i) \right), \quad (3.1)$$

where n_s is the number of signal events for a flux following spectral index γ ; N is the total number of events in the sample; S_i is the signal PDF for the i^{th} event, located at sky coordinates $\mathbf{x}_i = (\alpha_i, \delta_i)$, with energy E_i , and angular resolution σ_i . The background PDF B_i , for declination δ_i and energy E_i , is usually approximated by the event density of the real data integrated over right ascension. But unlike a point source, the signal from the Galactic plane may extend over the entire field of view. Hence for the assumption where $n_s > 0$, the signal present in the event density of the real data is not negligible. Thus, a modified likelihood function employing the signal-subtracted background is given by,

$$L(n_s, \gamma) = \prod_{i=1}^N \left(\frac{n_s}{N} S_i(\mathbf{x}_i, \sigma_i, E_i; \gamma) + \tilde{D}_i(\sin \delta_i, E_i) - \frac{n_s}{N} \tilde{S}_i(\sin \delta_i, E_i) \right), \quad (3.2)$$

where \tilde{D} and \tilde{S} are the event densities of the real data and simulated signal, respectively, integrated over right ascension. The signal PDF is constructed from the π^0 decay template (Fig. 4a) of the Fermi-LAT diffuse emission model [13]. To obtain a true signal PDF as it would be observed by IceCube (Fig. 4b), the spatial template is multiplied by the detector's acceptance to gamma-rays. The angular uncertainty of the events is incorporated in the likelihood by convolving the map with the point spread function (PSF) of the event, which is described by a Gaussian distribution of width σ (Fig. 4c).

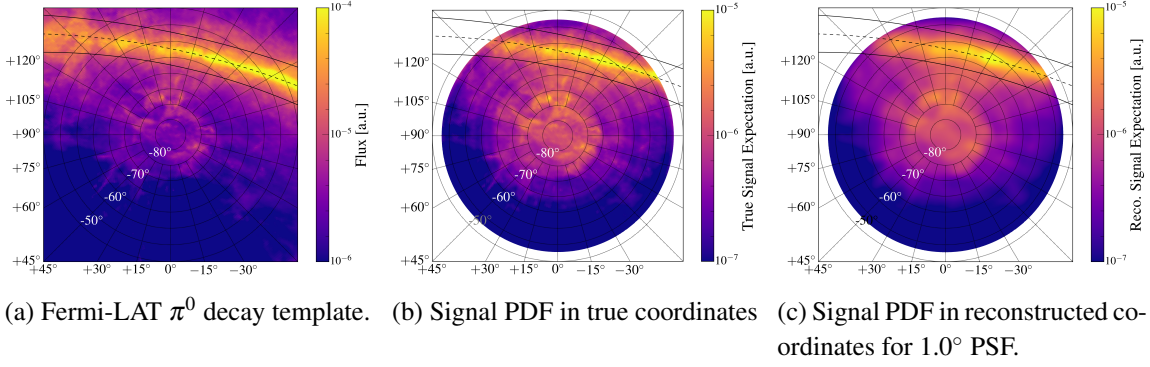


Figure 4: Steps for construction of signal PDF. Maps are plotted in equatorial coordinates and the dashed line shows the Galactic plane along with $|b| < 5$ bounds as solid lines.

The test statistic is then defined as the log-likelihood ratio of the best-fit signal strength and the null hypothesis, which corresponds to no Galactic diffuse emission. We have validated that the test statistic distribution for the null hypothesis $n_s = 0$ follows a χ^2 -distribution with one degree of freedom. The template analysis yields an angular-integrated flux ϕ' from the diffuse source region within the field of view. The spectral energy distribution defined as the flux scaled by E^2 , is given by the equation

$$E^2\phi'(E) = A \left(\frac{E}{E_0} \right)^{2-\gamma}, \quad (3.3)$$

where γ is the assumed source spectral index, A is the normalization constant, and E_0 is the reference energy. The median upper limit, as reported in Sec. 4, is the normalization A corresponding to a signal flux $\phi'(E)$ that generates a test statistic distribution with 90% of trials above the median of the null hypothesis distribution.

3.3 Spectral Index Assumption

Uncertainties in the Galactic cosmic ray spectrum, interstellar gas distribution, and flux attenuation between the source and the observer, result in an uncertainty in the observed spectral index for the diffuse emission. Calculations predict the unattenuated flux in the PeV energy range to follow a spectrum as hard as E^{-3} [14, 15], and the spectrum could be as soft as $E^{-3.4}$ [15] for the attenuated flux. Hence it becomes important to investigate the effect of the choice of spectral index on our analysis. We carry out the maximum likelihood analysis with various spectral index assumptions with the results shown in Fig. 3.2. The analysis is least sensitive to the spectral index assumption at about 2 PeV. Hence we quote the final median upper limit on the normalization A for $E_0 = 2 \text{ PeV}$ and $\gamma = 3$.

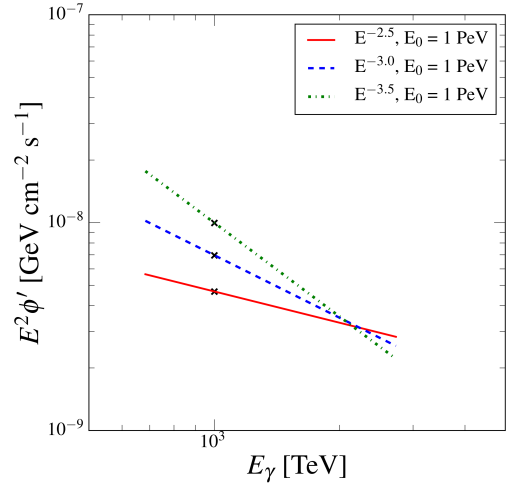
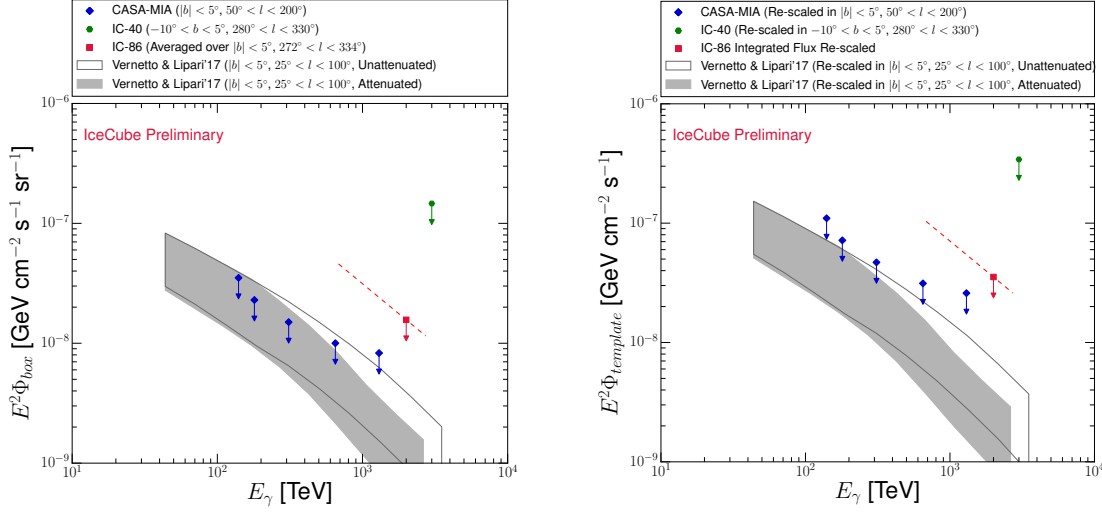


Figure 5: 90% C.L. upper limit spectral energy distribution with normalization at 1 PeV assuming different spectral indices.



(a) Flux from a boxed region around the Galactic plane. For IC-86, it is an average flux from the boxed region.

(b) Angular-integrated flux rescaled by the observed Galactic plane fraction calculated using the Fermi template.

Figure 6: IceCube 90% C.L. upper limit on the diffuse gamma-ray emission from the Galactic plane in our FOV as compared with the previous IceCube analysis using a partial detector IC-40 [16] and CASA-MIA [17]. The result from this analysis was obtained by using the Fermi-LAT π^0 decay spatial template [13] as compared to IC-40 and CASA-MIA which define a boxed region around the Galactic plane. Dotted lines show the E^{-3} spectrum, used for obtaining IceCube upper limits, over the energy range containing 5% to 95% events in the final sample. Also shown are unattenuated and attenuated flux predictions from Ref. [14].

4. Results And Discussion

We find no significant evidence for diffuse PeV gamma-rays from the Galactic plane. The observed test statistic corresponds to a p-value of 20.1%, and hence we do not exclude the null hypothesis of no diffuse emission. We place a 90% confidence level upper limit of 3.88×10^{-9} $\text{GeV cm}^{-1} \text{s}^{-1}$ on the normalization of the spectral energy distribution described in Eq. 3.3 for $E_0 = 2 \text{ PeV}$ and $\gamma = 3$. We have yet to gauge the dependence of current results on the choice of spatial template.

Typically, results of TeV-PeV gamma-ray emission along the Galactic plane are quoted as a diffuse flux within a box-shaped region in latitude b and longitude l . In order to compare our template based result to these observations, we use the following procedures. At first, we compare the flux from a boxed region (Φ_{box}) around the Galactic plane (Fig. 6a). To calculate the approximate Φ_{box} for this analysis, we use the Fermi template to find the fraction of the angular-integrated flux from this region: ($|b| < 5^\circ, 272^\circ < l < 334^\circ$); and divide it by the corresponding solid angle. For the second comparison (Fig. 6b), we propose an angular-integrated scaled flux as

$$\Phi_{\text{template}} = \Phi_{\Delta\Omega} \frac{\int_{\text{all sky}} S_{\text{Fermi}} d\Omega}{\int_{\Delta\Omega} S_{\text{Fermi}} d\Omega}, \quad (4.1)$$

where $\Phi\Delta\Omega$ gives the angular-integrated flux from the observed region, and the second term scales this flux by the fraction of Galactic plane, present in the observed region, as given by the Fermi template S_{Fermi} . In general, a template based analysis provides a more conservative upper limit than the analysis performed with the assumption of uniform emission from a boxed region.

In summary, the emission of PeV gamma-rays from the Galactic plane provides a measure of the Galactic distribution of cosmic rays in the knee region. The observation can provide valuable information for the modeling of cosmic ray propagation in, and escape from, our Galaxy (e.g., Ref. [18]). Our results complement the other strong limits derived by CASA-MIA, by placing competitive upper limits on the flux from a distinct portion of the Galactic plane. Result from this analysis corresponds to the strongest upper limit in the Southern Hemisphere, improving the previous limits by one order of magnitude.

References

- [1] S. Vernetto and P. Lipari, *Phys. Rev. D* **94** (2016) 063009.
- [2] **IceCube** Collaboration, M. G. Aartsen et al., *Phys. Rev. Lett.* **113** (2014) 101101.
- [3] M. Ahlers and K. Murase., *Phys. Rev. D* **90** (2014) 023010.
- [4] D. Heck, G. Schatz, T. Thouw, J. Knapp, and J. N. Capdevielle, *Report No. FZKA 6019* (1998) .
- [5] A. Ferrari, P.R. Sala, A. Fasso, and J. Ranft, *CERN-2005-10 (2005)*, *INFN/TC_05/11*, *SLAC-R-773*.
- [6] E. J. Ahn, R. Engel, T. K. Gaisser, P. Lipari, and T. Stanev , *Phys. Rev. D* **80** (2009) 094003.
- [7] **IceCube** Collaboration, Aartsen et al., *J. Inst.* **12** (2017) P03012.
- [8] **IceCube** Collaboration, T. Feusels, [PoS \(ICRC2015\) 334](#) (2015).
- [9] **IceCube** Collaboration, R. Abbasi et al., *Nucl. Instrum. Meth. A* **700** (2013) 188.
- [10] **IceCube** Collaboration, H. Pandya et al., [PoS \(ICRC2017\) 514](#) (these proceedings).
- [11] F. Pedregosa et al., *J. Mach. Learn. Res.* **12** (2011) 2825.
- [12] **IceCube** Collaboration, C. Haack et al., [PoS \(ICRC2017\) 1011](#) (these proceedings).
- [13] M. Ackermann et al., *Astrophys. J.* **750** (2012) 3.
- [14] S. Vernetto and P. Lipari, *EPJ Web of Conf.* **136** (2017) 03015.
- [15] G. Ingleman and M. Thunman, *arXiv* (1996) hep-ph/9604286.
- [16] **IceCube** Collaboration, M. G. Aartsen et al., *Phys. Rev. D* **87** (2013) 062002.
- [17] A. Borione et al., *Astrophys. J.* **493** (1998) 175.
- [18] D. Gaggero et al., *Astrophys. J. Lett.* **815** (2015) L25.

A composition sensitive log-likelihood ratio for cosmic rays and gamma rays

The IceCube Collaboration[†]

[†] http://icecube.wisc.edu/collaboration/authors/icrc17_icecube

E-mail: hershal@udel.edu

IceTop, the surface component of the IceCube Neutrino Observatory detects extensive air showers (EAS) initiated by cosmic rays and gamma rays in the energy range of PeV to EeV. IceTop is sensitive to air shower characteristics such as the muon content, local fluctuations and shower-front curvature. These characteristics correlate with the mass of the primary particle for a given energy and arrival direction. Using IceTop observables, we construct three two-dimensional probability distribution functions (PDFs) that reflect these shower-front properties. A log-likelihood ratio is constructed using these PDFs, assuming a pair of hypotheses corresponding to primaries with distinct mass. We show the effectiveness of this parameter for discriminating gamma rays from cosmic rays and heavy from light cosmic ray primaries.

Corresponding author: Hershhal Pandya^{*1}

¹*Dept. of Physics and Astronomy, University of Delaware, Newark, DE 19711, USA*

*35th International Cosmic Ray Conference — ICRC2017
10–20 July, 2017
Bexco, Busan, Korea*

*Speaker.

1. Introduction

High energy cosmic rays and gamma rays arriving at Earth, interact in the atmosphere creating cascades of secondary particles. These particle air showers can be detected using ground based air Cherenkov telescopes, fluorescence telescopes, or surface particle detectors. The sources of high energy cosmic rays and the mechanism responsible for accelerating them are still not fully understood. Measurement of the cosmic ray composition across the whole cosmic ray spectrum is important in order to constrain models for the cosmic ray acceleration and propagation. Cosmic ray composition is also important input for deciphering cosmic ray spectrum features such as the knee, the ankle, and the transitions between various cosmic ray populations which are expected to produce these features [1]. Cosmic ray interactions in their source environment or in the interstellar medium lead to emission of gamma rays and neutrinos. Hence, the detection of high energy gamma rays [2, 3] can give valuable insight into the cosmic ray acceleration mechanisms as well as the sources of the IceCube astrophysical neutrinos [4]. In this work, we present a method to discriminate between different primary particle types, based on the shower signals detected by an array of surface particle detectors. Although this method was developed for analysis of IceTop data, it is generally possible to adapt this technique for other surface arrays.

Surface particle detectors are able to reconstruct the energy and direction of the primary particle, but the challenge lies in reconstruction of the mass of the primary particle based on the shower imprint. Extensive air showers generated by photons, protons, and heavier cosmic rays differ mainly in two aspects for a given altitude: the shower age and the hadronic content. The approximate shower maxima, for example, for 2 PeV showers generated by iron, protons, and photons occur at 460, 580 and 620 g/cm^2 respectively [5]. Hence, lighter particles generate younger showers at the detector altitude. In addition, these showers differ in the hadronic content of the cascades, which can be derived from the local fluctuations and muon content of the shower-front. Muon content comparison for photons, protons, and iron is shown in Fig. 1. Measurement of these properties is contingent on the geometry of the array, and response of the detectors to electrons, photons, and muons within the EAS.

The mapping from detector observables to the mass of the primary particle depends on the hadronic interaction models used during simulation of the air showers. For this work, air showers were simulated with CORSIKA [6], using SIBYLL 2.1 [8] for high energy, and FLUKA [7] for low energy hadronic interactions.

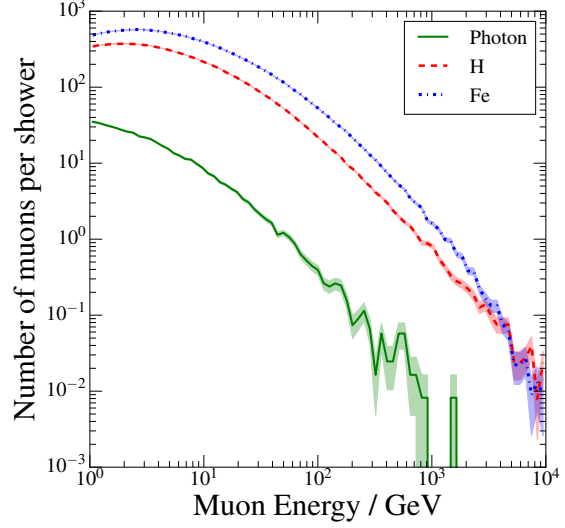


Figure 1: Muon spectra for near vertical 1 PeV photon, proton, and iron CORSIKA showers simulated using SIBYLL 2.1.

2. IceTop

IceTop is the surface component of the IceCube neutrino observatory which is located at the geographic South Pole. As shown in Fig. 2, it is a square kilometer array of 162 ice tanks, each equipped with two digital optical modules (DOMs). The DOMs detect Cherenkov radiation emitted by relativistic charged particles passing through the tank. A pair of tanks forms a station, and spacing between two neighboring stations is 125 m on average, with an additional denser in-fill region in the center of the array. IceTop is located at an altitude of 2835 m above sea level which corresponds to an atmospheric depth of around 692 g/cm^2 . IceTop is most sensitive to air showers generated by cosmic rays in the energy range of roughly 1 PeV to 1 EeV. IceTop triggers at a rate of about 30 Hz, with a rate of successfully reconstructed events above 1 PeV of about 3 Hz.

IceTop DOMs are calibrated using vertical muons from low energy air showers. Muons deposit roughly the same amount of energy, characterized by their constant ionization loss in ice and their path length inside the tank. Thus, the signals are measured in the units of vertical equivalent muons (VEM). Shower direction, core location, and shower energy are reconstructed by simultaneously fitting the measured charges with an LDF, and signal times with a function which describes the shower-front curvature. The lateral distribution function is defined as [9]

$$S(R) = S_{125} \left(\frac{R}{125 \text{ m}} \right)^{-\beta - 0.303 \log_{10} \left(\frac{R}{125 \text{ m}} \right)}, \quad (2.1)$$

where $S(R)$ is the signal measured at a lateral distance R from shower axis, β is the slope of the logarithmic LDF at 125 m. The signal measured at 125 m, S_{125} , is the shower size or energy proxy. Snow accumulates on top of the IceTop tanks over time, which reduces the measured signal in the tank. This attenuation is accounted for while reconstructing the shower size, by taking the snow height on each tank into account.

The simulation datasets used in this work are generated using snow heights measured in October of 2012, and the observed data used for testing is a randomly selected 10% subsample of the IceTop data recorded between May 2012 and May 2013. We restrict our analysis to the $\log_{10}(S_{125})$ range of 0 to 2, which corresponds to energy range of roughly 1 PeV to 78 PeV for vertical showers. Quality cuts are applied to all events to ensure that the events used in the final sample are successfully reconstructed.

3. Construction of Probability Distribution Functions

For every successfully reconstructed IceTop event, the following observables are available: a.) measured tank charge, signal time with respect to core arrival time, and lateral distance of the tanks

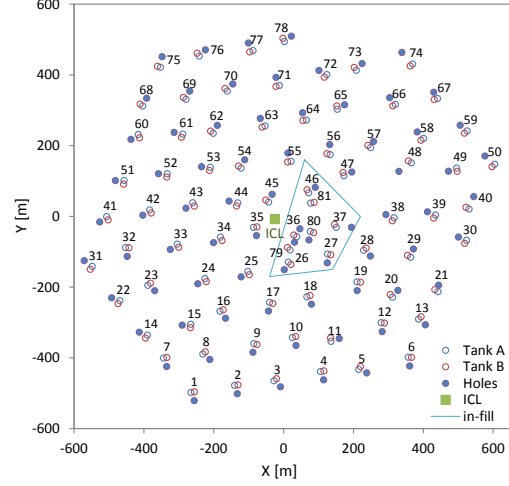


Figure 2: IceTop array geometry [9].

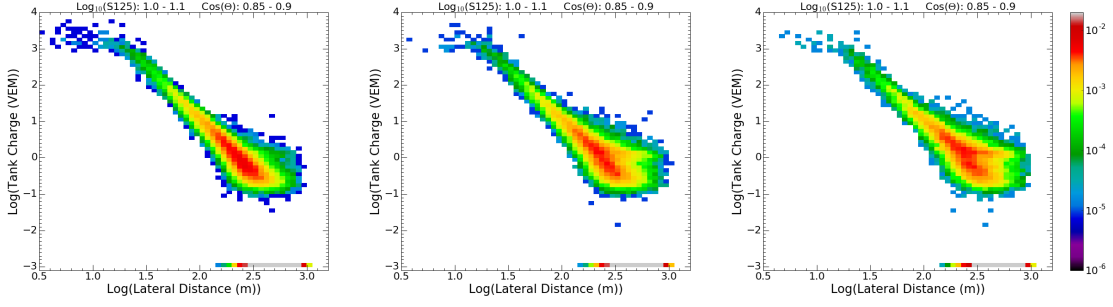


Figure 3: PDF based on lateral distribution of charges for photons, protons, and iron (left to right). For events with $1.0 \leq \log_{10}(S_{125}) < 1.1$ and $0.85 \leq \cos \theta < 0.9$.

hit by the shower-front, b.) lateral distance for tanks that did not record any signal (unhit tanks). The residual time ΔT for each tank is obtained by subtracting the expected signal time, according to a median shower curvature, from the observed signal time. Thus for each event, we obtain the following observables:

$$\begin{aligned} & \{(Q_i, \Delta T_i, R_i)\}, \forall \text{ Hit tank,} \\ & \{R_i\}, \forall \text{ Unhit tank,} \\ & N_{\text{Hit}} + N_{\text{UnHit}} = 162, \end{aligned} \quad (3.1)$$

where Q_i is the charge measured, ΔT_i is the residual time, and R_i is the lateral distance of i^{th} tank. Using these observables we construct three two-dimensional probability distribution functions (PDFs). Since different events have varying number of tanks hit by the shower-front, we include the unhit tanks in the PDF by assigning them with a false charge of 10^{-3} VEM and a false residual time of 10^{-2} ns. This ensures a correct normalization for the PDF. The shower properties vary with energy of the primary particle as well as the zenith angle. Hence, the PDFs are generated separately for various $\log_{10}(S_{125})$ and $\cos \theta$ bins. The values of $\log_{10}(S_{125})$ range from 0.0 to 2.0 in steps of 0.1, and $\cos \theta$ from 0.8 to 1.0 in steps of 0.05.

3.1 Lateral Distribution of Charges

As discussed in Sec. 2, muons going through a tank deposit around 1 VEM energy depending on their path length inside the tank. The signal in tanks near the shower core is dominated by the electromagnetic component of the air shower. Beyond a large lateral distance, the electromagnetic LDF falls off, exposing the roughly 1 VEM signal from GeV muons. This muon feature is visible in the PDF based on the lateral distribution of charges as shown in Fig. 3. The muon signal far from the shower core gets more prominent for heavier masses, whereas it is almost absent for the photon induced air showers. The PDF shown in Fig. 3 also contains information on the shower age and hadronic content. The slope of the LDF correlates with the shower age, and the width of the charge distribution for a given radius, arising from local fluctuations, is correlated with the hadronic content of the shower.

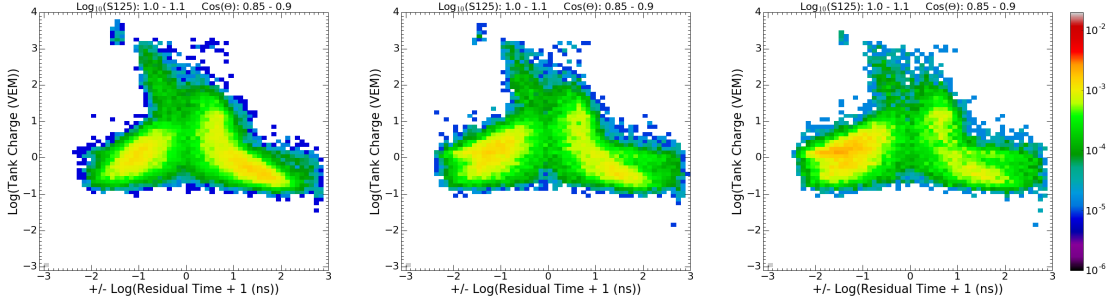


Figure 4: PDF based on tank charge versus residual time for photons, protons, and iron (left to right). For events with $1.0 \leq \log_{10}(S_{125}) < 1.1$ and $0.85 \leq \cos \theta < 0.9$.

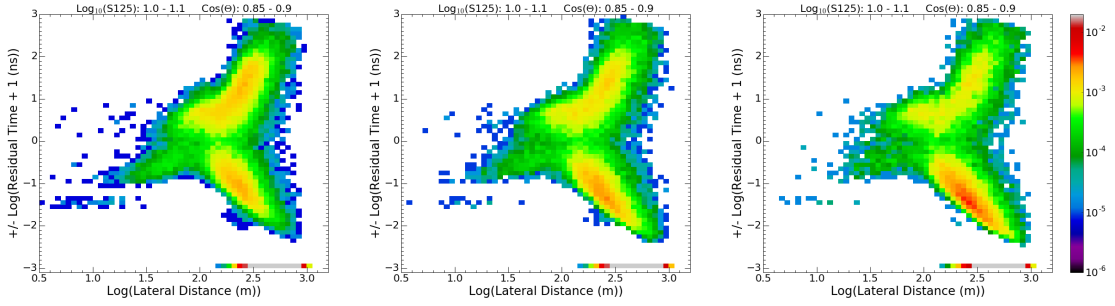


Figure 5: PDF based on shower-front shape after shower curvature subtraction for photons, protons, and iron (left to right). For events with $1.0 \leq \log_{10}(S_{125}) < 1.1$ and $0.85 \leq \cos \theta < 0.9$.

3.2 Time Distribution

In addition to the PDF described in Sec. 3.1, we construct two more PDFs that utilize the temporal distribution of the shower particles. The time residuals ΔT_i can have negative (early) as well as positive (late) values. Hence, the transformation of residual time to the logarithmic scale is done as $\text{Sign}(\Delta T) \log_{10}(|\Delta T| + 1)$. From Fig. 4 one can observe that muons arrive relatively early at the detector surface from their signature 1 VEM charge accumulation at negative times. PDFs shown in Fig. 5 represent the shower-front of three primary masses with an average proton shower curvature subtracted out of all of them. It can be noted that heavier masses have a larger fraction of particles arriving earlier in time.

3.3 Log-Likelihood Ratio

For a given pair of hypotheses, H_1 and H_2 , a log-likelihood ratio is calculated based on one of the three PDFs, described in the previous section. The pair of hypothesis could be H_γ and H_{CR} for the purpose of separating gamma ray air showers from hadronic showers or it could be H_H and H_{Fe} for the aim of cosmic ray composition. The log-likelihood ratio using lateral distribution of charges, for example, is calculated as

$$\lambda_{QR} = \log_{10} \left(\frac{L(\{(Q_i, R_i)\} | H_2)}{L(\{(Q_i, R_i)\} | H_1)} \right), \quad (3.2)$$

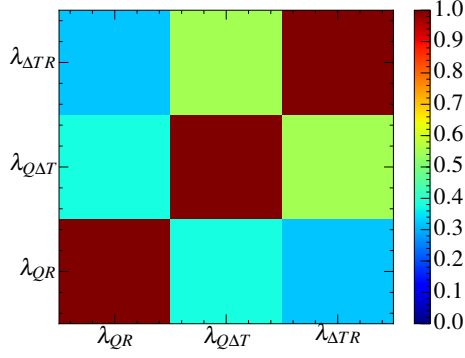


Figure 6: Pearson correlation coefficient matrix for log-likelihood ratios obtained using three PDFs as described in Sec. 3.

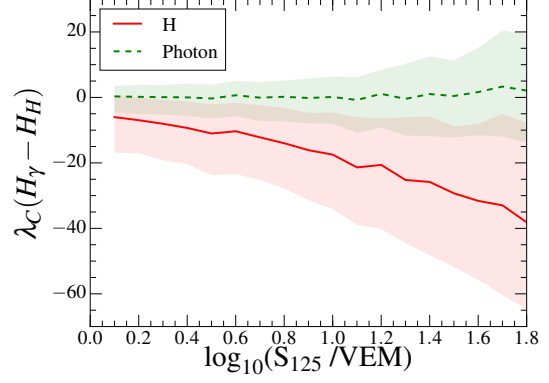


Figure 7: $\lambda_C(H_\gamma - H_H)$ versus $\log_{10}(S_{125})$ for simulated gamma ray and proton showers with $0.8 \leq \cos \theta < 1.0$. Shaded regions contain 95% of the events.

where the likelihood L is defined as

$$L(\{(Q_i, R_i)\} | H) = \prod_{i=1}^{162} P(Q_i, R_i | H), \quad (3.3)$$

with $P(Q_i, R_i | H)$ being the probability of having a tank with measured charge Q_i (VEM), at a lateral distance R_i (m) from the shower axis, for the hypothesis H . Similarly, one can calculate $\lambda_{Q\Delta T}$ and $\lambda_{\Delta TR}$ from the PDFs based on the time distribution of charges and the shower-front shape.

Infrequently it may be possible that $P(Q_i, R_i | H)$, $P(\Delta T_i, R_i | H)$, or $P(Q_i, \Delta T_i | H)$ for the i^{th} tank, may not be defined in a PDF for a particular event. This may occur due to less number of events used for generating the PDF or due to shower-to-shower fluctuations. For such tanks, the P value is obtained by extrapolation. After the extrapolation, the PDF is re-normalized and the log-likelihood ratio for the event is calculated.

4. Results and Discussion

The log-likelihood ratios $\lambda_{Q\Delta T}$, $\lambda_{\Delta TR}$, and λ_{QR} , are expected to be correlated to each other. The Pearson correlation coefficient matrix for the three ratios is shown in Fig. 6. To fully utilize classification power from all three log-likelihood ratios, a dimension reduction technique such as linear discriminant analysis, or a classification algorithm like the decision tree needs to be implemented. However, as a first estimate one can define a combined log-likelihood ratio as

$$\lambda_C = \lambda_{QR} + \lambda_{\Delta TR} + \lambda_{Q\Delta T}, \quad (4.1)$$

which is equivalent to taking a simultaneous log-likelihood ratio, for a given event, using all three PDFs.

One of the applications of this method is to search for PeV gamma rays in the IceTop data. We calculate the λ_C for simulated proton and gamma ray showers, using the hypothesis pair $H_\gamma -$

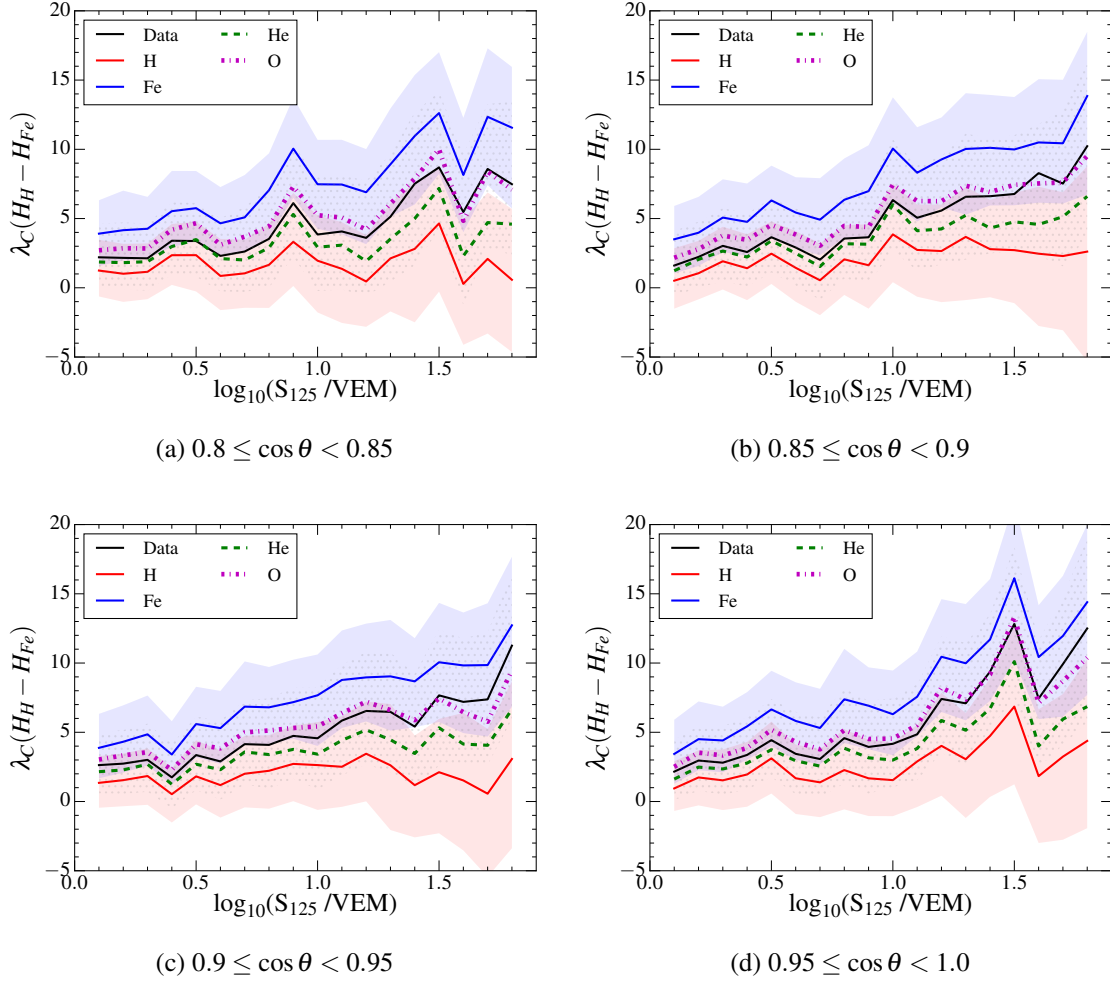


Figure 8: $\lambda_C(H_H - H_{Fe})$ versus $\log_{10}(S_{125})$ for simulated proton, helium, oxygen, and iron, as well as observed IceTop data. Blue and red shaded regions confine 68.27% λ_C distribution for Fe and H, while the dotted region confines 68.27% of data λ_C distribution. The four sub plots correspond to four different zenith angle bins.

H_H , to show the performance of this method (Fig. 7). As shown in Fig. 3, Fig. 4, and Fig. 5, the differences between photon and proton PDFs are rather pronounced, as compared to differences between proton and iron. Since the expected flux of PeV gamma rays is of the order of 10^{-4} of the cosmic ray flux or less, the final sample of gamma rays needs to have a high degree of purity. Hence, we show a 95% error region around the median in Fig. 7. The quality of separation using λ_C improves with $\log_{10}(S_{125})$. This is partly due to an improvement of the angular resolution, and partly due to increasing differences in the shower properties.

The goal in the case of cosmic ray composition is to separate four different mass groups with comparable fluxes but fairly close shower properties. For the purpose of demonstration, we calculate the λ_C using the hypothesis pair $H_H - H_{Fe}$. The resulting distributions are shown in Fig. 8. The distributions for helium and oxygen are placed between proton and iron, and helium is placed below oxygen, as expected. The data is close to Helium at $\log_{10}(S_{125}) = 0.1$, it crosses Oxygen

at intermediate energies, and is placed above Oxygen for $\log_{10}(S_{125}) = 1.8$. This indicates that the fraction of heavier mass primaries is increasing in the data with increasing primary energy. Inclined showers pass through more atmosphere resulting in decay of particles before they reach the detector. This affects heavier primaries more than lighter primaries. A trend of data getting lighter towards larger zenith angles can be seen in Fig. 8. Although none of these are statistically significant results, they are indicators of this method's capability to classify cosmic ray primaries.

In conclusion, we present this new log-likelihood ratio as a mass sensitive parameter for extensive air showers detected by surface particle detectors. Analyses described in Refs. [2, 3] utilize this technique for discriminating gamma ray showers from cosmic ray showers. An implementation of this technique is underway for an event-by-event determination of cosmic ray mass composition using IceTop data. In principle, it is possible to adapt this technique for other surface detectors, like the HAWC observatory [10] and the surface detector component of the Pierre-Auger observatory [11]. The choice of variables and PDFs would depend on the detector response to various components of the EAS, detector geometry, and resolution of the reconstructed shower parameters.

References

- [1] T. K. Gaisser, T. Stanev, S. Tilav, *Front. Phys.* **8** (2013) 748.
- [2] **IceCube** Collaboration, H. Pandya et al., [PoS\(ICRC2017\) 705](#) (these proceedings).
- [3] **IceCube** Collaboration, Z. Griffith et al., [PoS\(ICRC2017\) 715](#) (these proceedings).
- [4] **IceCube** Collaboration, M. G. Aartsen et al., *Phys. Rev. Lett.* **113** (2014) 101101.
- [5] M. Risse and P. Homola, *Mod. Phys. Lett. A* **22** (2007) 749.
- [6] D. Heck, G. Schatz, T. Thouw, J. Knapp, and J. N. Capdevielle, *Report No. FZKA 6019* (1998) .
- [7] A. Ferrari, P.R. Sala, A. Fasso, and J. Ranft, *CERN-2005-10 (2005)*, *INFN/TC_05/11*, *SLAC-R-773*.
- [8] E. J. Ahn, R. Engel, T. K. Gaisser, P. Lipari, and T. Stanev , *Phys. Rev. D* **80** (2009) 094003.
- [9] **IceCube** Collaboration, R. Abbasi et al., *Nucl. Instrum. Meth. A* **700** (2013) 188.
- [10] A.U. Abeysekara et al., *arXiv* (2017) 1701.01778.
- [11] The Pierre Auger collaboration, *Nucl. Instrum. Meth. A* **798** (2015) 172.

Cosmic-Ray Anisotropy with Seven Years of Data from IceCube and IceTop

The IceCube Collaboration[†]

[†] http://icecube.wisc.edu/collaboration/authors/icrc17_icecube

E-mail: james.bourbeau@icecube.wisc.edu

With data collected over the last seven years, the IceCube Neutrino Observatory at the South Pole has measured both the large- and small-scale anisotropy in the cosmic-ray arrival direction distribution with a high level of significance. In addition to the sidereal anisotropy, we have also measured the solar dipole caused by the orbital motion of the Earth around the Sun. We present the cosmic-ray anisotropy measurement with a full seven years of data and a systematic study of both the sidereal anisotropy and solar dipole.

Corresponding authors: James Bourbeau^{*1}, P. Desiati¹, J.C. Díaz-Vélez¹, and S. Westerhoff¹

¹ *Wisconsin IceCube Particle Astrophysics Center (WIPAC) and Department of Physics, University of Wisconsin–Madison, Madison, WI 53706, USA*

*35th International Cosmic Ray Conference - ICRC217-
10-20 July, 2017
Bexco, Busan, Korea*

*Speaker.

1. Introduction

Over the last few decades, a number of surface and underground experiments have observed a statistically significant anisotropy in the arrival direction distribution of cosmic rays in the energy range from tens of GeV to tens of PeV. In the TeV to PeV range, measurements of anisotropy have been published by a number of experiments using different detection and analysis techniques, including the Tibet AS γ [1], Super-Kamiokande [2, 3], Milagro [4, 5], EAS-TOP [6], MINOS [7], ARGO-YBJ [8], and HAWC [9] experiments in the Northern Hemisphere and IceCube [10, 11, 12, 13] and its surface air shower array IceTop [14] in the Southern Hemisphere.

The angular power spectrum of the arrival direction distribution shows that while most of the power is in the low multipole terms ($\ell \leq 4$, corresponding to angular scales greater than 45°), features of smaller angular scale down to a few degrees are also present. The relative intensity of the large-scale anisotropy ($\ell \leq 4$) is at the level of 10^{-3} , an order of magnitude larger than the intensity of the small-scale structure. Observations below 100 TeV show a structurally consistent large-scale anisotropy with wide relative excess and deficit regions. This structure strongly depends on energy. The amplitude of the anisotropy decreases from 50 TeV to 100 TeV. Above 100 TeV the phase of the anisotropy changes and the sky maps now show a wide relative deficit in right ascension with an amplitude that increases with energy until at least 5 PeV, where statistics become poor. Recent measurements with the Pierre Auger Observatory at EeV energies show a significant dipole at energies above 8 EeV, but no deviation from isotropy at any other scale or at lower energies [15].

While the source of the anisotropy remains unknown, it has been shown that standard diffusive propagation of cosmic rays in the Galaxy from stochastically distributed sources can qualitatively explain the large-scale structure. The phase shift at higher energies potentially indicates a change in the location of the dominant source(s). The small-scale structure can be produced by the interaction of cosmic rays with the turbulent interstellar magnetic field. For a further discussion of possible explanations for the large- and small-scale structure as well as for the energy-dependence of the anisotropy, we refer to the summary and discussion section in [13] and a recent review article [16].

In the Southern Hemisphere, the IceCube Neutrino Observatory has accumulated one of the largest cosmic-ray data sets to date, allowing for a detailed study of the morphology and the time- and energy-dependence of the anisotropy from TeV to PeV energies. Located at the geographic South Pole, IceCube comprises a neutrino detector buried in the deep ice (hereafter referred to as the in-ice component) and a surface air shower array, IceTop. IceCube [17] consists of 86 vertical strings containing a total of 5,160 optical sensors, called Digital Optical Modules (DOMs), which are frozen in the ice at depths from 1450 to 2450 m below the surface. The total instrumented volume is about a cubic kilometer. IceTop [18] consists of 81 surface stations spread over an area of 1 km^2 . Each station consists of two light-tight tanks with a 1.82 m inner diameter that are filled with ice to a height of 0.90 m. Each tank hosts two DOMs to detect the Cherenkov light generated by the relativistic particles of the air shower reaching the detector level and traversing the tanks.

With its two components, IceCube detects cosmic rays over a wide range of energies. The in-ice component detects downward-going muons created in air showers initiated by cosmic-ray primaries. According to simulations, the energy of the primary cosmic rays ranges from approximately 10 TeV to 5 PeV, where current statistics becomes poor. The trigger rate is modulated by seasonal variations and ranges between 2 and 2.4 kHz. The IceTop air shower array detects cosmic

rays above 400 TeV. The median energy is 1.6 PeV. This enables IceTop, which mainly measures the electromagnetic component of the air showers, to provide an independent measurement at the high-energy end of the range of the in-ice detector. The trigger rate is 30 Hz.

A detailed study of the large- and small-scale anisotropy with IceCube and IceTop based on six years of data was recently published [13]. Here, we report updated results including an additional year of data, bringing the total data set size to 368 billion cosmic-ray events observed by the in-ice component and 196 million events observed with IceTop. The data were taken between May 2009 and May 2016. In the first two years, the detector was operated in partial detector configurations with 59 and 79 active strings, respectively (IC59/IC79). Subsequent years with the full 86 string detector are labeled IC86-I to IC86-V. The seven year period covered by this analysis allows for a study of a possible time dependence during the first part of the current (24th) solar cycle.

2. Analysis and Results

Details about the analysis methods used in this work have been published previously [11, 14, 13]. All sky maps shown here were made using the HEALPix [19] mapping program to pixelize the sky into bins of equal solid-angle. Here, we use a pixel size of $(0.84^\circ)^2$ ($N_{side} = 64$). The maps are top-hat smoothed with a 5° angular radius (each pixel's value is replaced with the sum of all pixels within a 5 radius.).

Following [13], we split the in-ice data in nine energy bins according to the number of DOMs hit in the event and the cosine of the reconstructed zenith angle. This results in a sequence of maps with increasing median energy, ranging from 13 TeV for the lowest energy bin to 5.4 PeV for the highest energy bin. For the IceTop data, we only use one energy bin with a median energy of 1.6 PeV. Figure 1 shows the sky maps in relative intensity for all nine energy bins in equatorial coordinates. The median energy of the data shown in each map is indicated in the upper left. The maps clearly show the strong dependence of the anisotropy on energy and the change in the morphology above about 100 TeV, where the sky maps now show a wide relative deficit from 30° - 120° in right ascension. The amplitude increases with energy.

To illustrate the energy dependence of the phase and the amplitude of the anisotropy, we fit the set of harmonic functions with $n \leq 3$ to the projection of the two-dimensional relative intensity map in right ascension α ,

$$\sum_{n=0}^3 A_n \cos[n(\alpha - \phi_n)] , \quad (2.1)$$

where A_n is the amplitude and ϕ_n is the phase of the n^{th} harmonic term. Figure 2 shows the amplitude (*left*) and phase (*right*) of the dipole moment as a function of energy. The red data point is based on the IceTop data. While the phase agrees well with that of the IceCube data at similar energies, the amplitude of the anisotropy is larger for the IceTop data than for any IceCube energy bin. A possible explanation for the difference could be the different chemical composition of the IceCube and IceTop data sets (see Table 4 in [13]). If the anisotropy is predominantly caused by protons, the lighter composition of the IceTop data could lead to a stronger dipole amplitude.

The data used in this analysis were recorded over a period of seven years, from 2009 to 2016. This period covers a large fraction of the current (24th) solar cycle, which started in January 2008

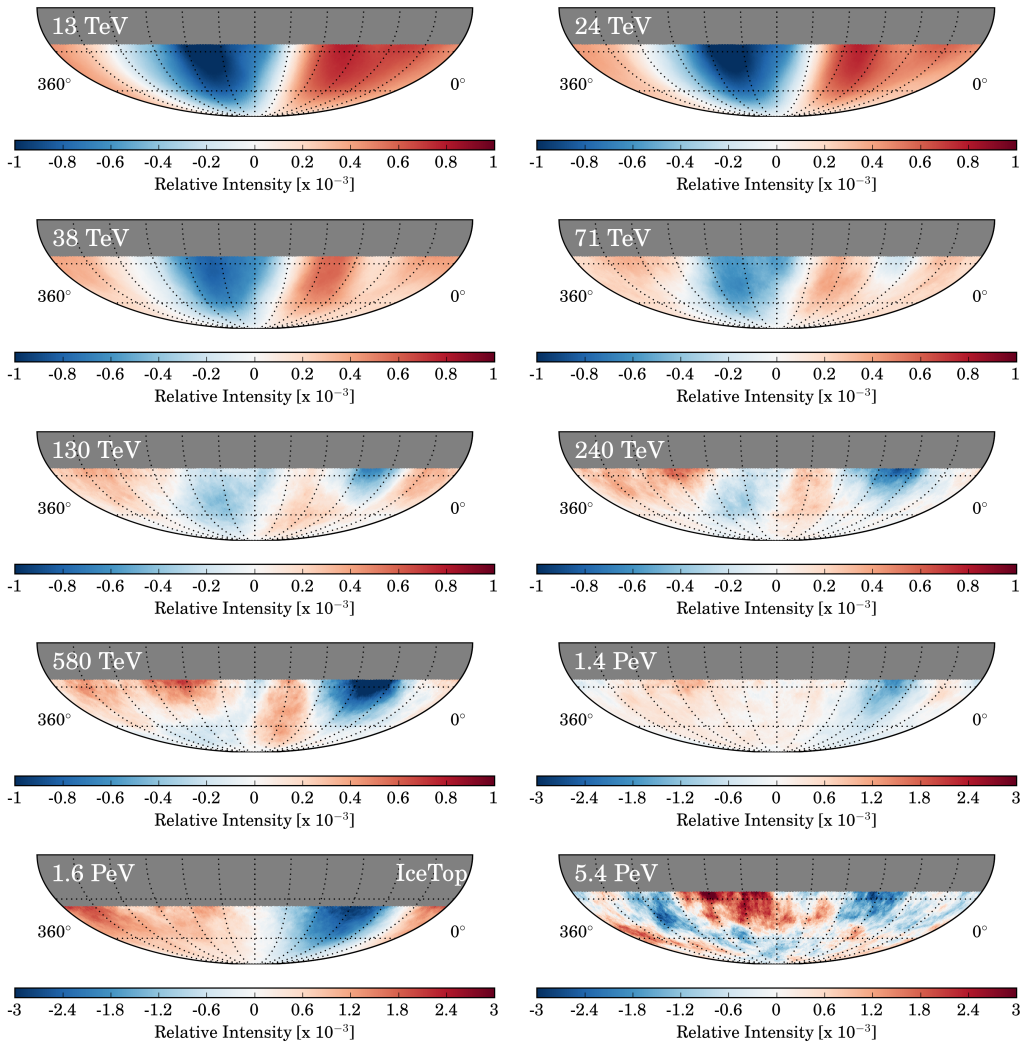


Figure 1: Equatorial maps of the relative intensity of the cosmic-ray flux. An angular smoothing with 20° radius is applied to all maps. Note that the three highest-energy maps have a different intensity scale.

and reached a maximum in April 2014. Figure 3 shows the one-dimensional projection of the relative intensity in right ascension for each year of data. The yearly data points are placed side by side in time sequence, with the different right ascension bins delineated by vertical lines. The shaded areas indicate systematic errors, estimated using the anti-sidereal frame for each year as described in [13]. We conclude that the large-scale structure is stable over the data period considered here. The Tibet experiment also did not observe significant time variation in the large-scale anisotropy in the northern hemisphere between 1999 and 2008 [20]. In addition, no time-dependence of the large-scale anisotropy is seen in data taken with the AMANDA-II detector at the South Pole between 2000 and 2006 [21]. In contrast, Milagro reported an increase in the amplitude of the large-scale structure between 2000 and 2007 [5]. In a separate analysis [13], we also found that the smaller structure shows no significant dependence on time. The ARGO-YBJ experiment also observed a steadiness in the small-scale structure of their measured anisotropy [8].

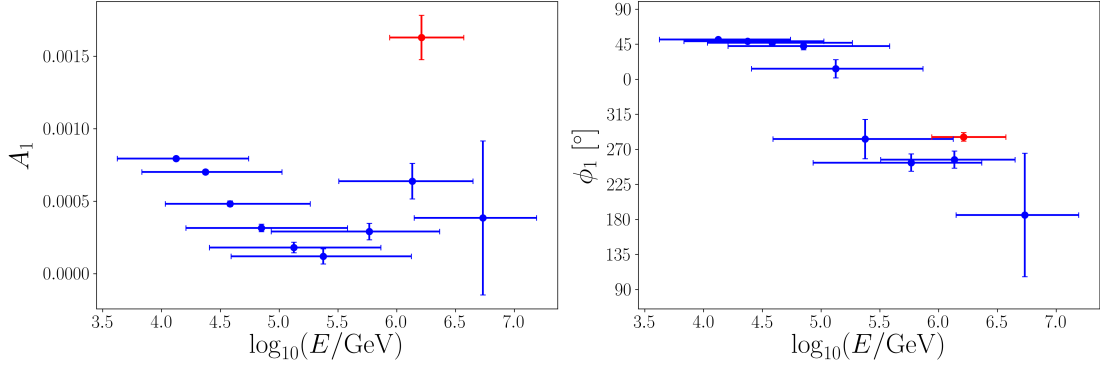


Figure 2: Amplitude (*left*) and phase (*right*) of dipole fit to IceCube (*blue*) and IceTop (*red*) sky maps for various energy bins. Data points indicate the median energy of each energy bin, with error bars showing the 68% containment interval.

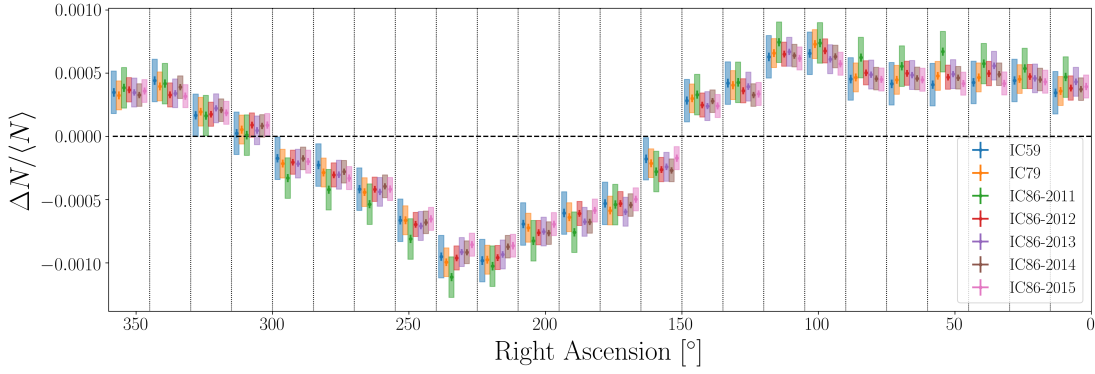


Figure 3: Projection of relative intensity for all declinations as a function of right ascension for each configuration of the IceCube detector from IC59 to the fifth year of IC86. The yearly data points are placed side by side in time sequence, and the different right ascension bins are delineated by vertical lines. The shaded areas indicate systematic errors, calculated using the anti-sidereal frame for each year independently.

3. Solar Dipole

An important systematic check of the reliability of the anisotropy analysis is the study of the solar dipole, i.e., the dipole in the cosmic-ray arrival direction distribution caused by the motion of the Earth around the Sun. This dipole appears when the cosmic-ray arrival directions are plotted in a frame where the position of the Sun is at a fixed location. The projection of the relative intensity in right ascension for the sidereal and solar frame are shown in Fig. 4. For the solar frame, the “right ascension” axis shows the difference between the right ascension of the event and the right ascension of the Sun. Note that the Sun is located at 0° and the direction of motion (and thus the dipole maximum) is at 270° . The fit of the projection to a dipole results in an amplitude of $(2.231 \pm 0.031) \times 10^{-4}$ and a phase of $(267.58 \pm 0.78)^\circ$. The χ^2 -probability of the fit is 0.45 ($\chi^2 = 21.60$ for 23 degrees of freedom). The measured amplitude of the projection agrees well with expectations.

Currently, we are studying possible seasonal variations of the solar dipole and the sidereal

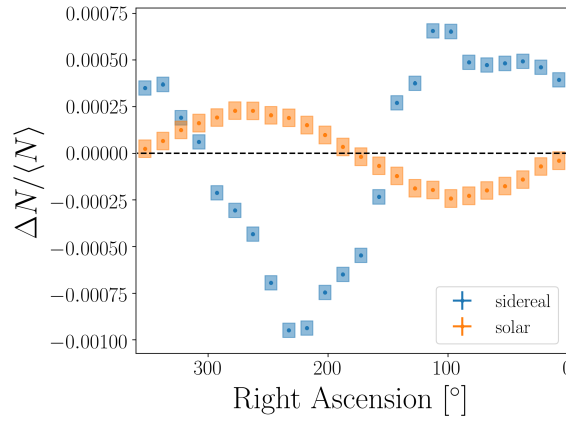


Figure 4: Projection of relative intensity in right ascension for solar and sidereal time. Error boxes indicate systematic errors. For the solar frame, the right ascension axis shows the difference between the right ascension of the event and the right ascension of the Sun.

anisotropy. Seasonal variations in the solar dipole can manifest themselves as an anisotropy in the sidereal frame and vice versa, so this study will help to understand possible systematic effects on the amplitude and phase of the sidereal anisotropy. In addition, physical effects, for example the Compton-Getting effect (apparent dipole due to the relative motion between the solar system and the cosmic-ray rest frame) [22] could manifest themselves in a faint seasonal variation of the solar dipole and the sidereal anisotropy.

4. Summary and Outlook

The analysis of seven years of cosmic-ray data observed with the IceCube Neutrino Observatory reveals a strongly energy-dependent anisotropy in the arrival direction distribution. The anisotropy is most significant at the low-order multipoles of the angular power spectrum (dipole, quadrupole, and octupole), but it is observed on scales down to a few degrees, close to the angular resolution of the detector. At the highest energy, around a few PeV, the IceTop air-shower array provides an independent measurement of the anisotropy. The dipole amplitude is significantly larger in IceTop, a discrepancy possibly caused by the different chemical composition of the IceCube and IceTop data sets. Since IceTop provides additional shower parameters that are sensitive to the chemical composition, this effect can be investigated in more detail in the future. We are currently studying whether the anisotropy shows significant differences for data sets containing mostly light (proton and helium) or mostly heavy elements (up to iron).

The IceCube detector only covers parts of the southern hemisphere. In the northern hemisphere, the High Altitude Water Cherenkov (HAWC) Observatory in Mexico now provides cosmic-ray data at an unprecedented rate [9]. The combination of IceCube and HAWC cosmic-ray data produces a data set that covers almost the entire sky and helps to overcome some of the shortcomings of analyses with partial sky coverage [23]. A combined analysis using HAWC and IceCube data is also presented at this conference [24].

References

- [1] **Tibet AS γ** Collaboration, M. Amenomori et al., *Large-Scale Sidereal Anisotropy of Galactic Cosmic-Ray Intensity Observed by the Tibet Air Shower Array*, *Astrophys. J.* **626** (2005) L29.
- [2] **Kamiokande** Collaboration, K. Munakata et al., *Large-Scale Anisotropy of the Cosmic-Ray Muon Flux in Kamiokande*, *Phys. Rev. D* **56** (1997) 23.
- [3] **Super-Kamiokande** Collaboration, G. Guillian et al., *Observation of the Anisotropy of 10 TeV Primary Cosmic Ray Nuclei Flux with the Super-Kamiokande-I Detector*, *Phys. Rev. D* **75** (2007) 062003.
- [4] **Milagro** Collaboration, A.A. Abdo et al., *Discovery of Localized Regions of Excess 10-TeV Cosmic Rays*, *Phys. Rev. Lett.* **101** (2008) 221101.
- [5] **Milagro** Collaboration, A.A. Abdo et al., *The Large-Scale Cosmic-Ray Anisotropy as Observed with Milagro*, *Astrophys. J.* **698** 2121 2009.
- [6] **EAS-TOP** Collaboration, M. Aglietta et al., *Evolution of the Cosmic-Ray Anisotropy Above 10^{14} eV*, *Astrophys. J.* **692** (2009) L130.
- [7] **MINOS** Collaboration, J.K. deJong et al., *Observations of Large Scale Sidereal Anisotropy in 1 and 11 TeV Cosmic Rays from the MINOS Experiment*, *Proc. 32nd ICRC*, Beijing, China (2011) [arXiv:1201.2621].
- [8] **ARGO-YBJ** Collaboration, B. Bartoli et al., *Medium Scale Anisotropy in the TeV Cosmic Ray Flux Observed by ARGO-YBJ*, *Phys. Rev. D* **88** (2013) 082001.
- [9] **HAWC** Collaboration, A.U. Abeysekara et al., *Observation of Small-Scale Anisotropy in the Arrival Direction Distribution of TeV Cosmic Rays with HAWC*, *Astrophys. J.* **796** (2014) 108.
- [10] **IceCube** Collaboration, R.U. Abbasi et al., *Measurement of the Anisotropy of Cosmic-Ray Arrival Directions with IceCube*, *Astrophys. J.* **718** (2010) L194.
- [11] **IceCube** Collaboration, R.U. Abbasi et al., *Observation of Anisotropy in the Arrival Directions of Galactic Cosmic Rays at Multiple Angular Scales with IceCube*, *Astrophys. J.* **740** (2011) 16.
- [12] **IceCube** Collaboration, R.U. Abbasi et al., *Observation of Anisotropy in the Galactic Cosmic-Ray Arrival Directions at 400 TeV with IceCube*, *Astrophys. J.* **746** (2012) 33.
- [13] **IceCube** Collaboration, M.G. Aartsen et al., *Anisotropy in Cosmic-Ray Arrival Directions in the Southern Hemisphere Based on Six Years of Data from the IceCube Detector*. *Astrophys. J.* **826** (2016) 220.
- [14] **IceCube** Collaboration, M.G. Aartsen et al., *Observation of Cosmic-Ray Anisotropy with the IceTop Air Shower Array*, *Astrophys. J.* **765** (2013) 55.
- [15] **Pierre Auger** Collaboration, A. Aab et al., *Multi-Resolution Anisotropy Studies of Ultrahigh-Energy Cosmic Rays Detected at the Pierre Auger Observatory*, submitted to *Journal of Cosmology and Astroparticle Physics*. [arXiv:1611.06812].
- [16] M. Ahlers and P. Mertsch, *Origin of Small-Scale Anisotropies in Galactic Cosmic Rays*, *Progress in Particle and Nuclear Physics*, **94** (2017) 184.
- [17] **IceCube** Collaboration, M.G. Aartsen et al., *The IceCube Neutrino Observatory: Instrumentation and Online Systems*, *Journal of Instrumentation* **12** (2017) P03012.

- [18] **IceCube** Collaboration, R.U. Abbasi et al., *IceTop: The Surface Component of IceCube*, *Nucl. Instr. Meth. A* **700** (2013) 188.
- [19] K.M. Górski et al., *HEALPix - a Framework for High Resolution Discretization, and Fast Analysis of Data Distributed on the Sphere*, *Astrophys. J.* **622** (2005) 759.
- [20] **Tibet AS γ** Collaboration, M. Amenomori et al., *On Temporal Variations of the Multi-TeV Cosmic Ray Anisotropy Using the Tibet III Air Shower Array*, *Astrophys. J.* **711** (2010) 119.
- [21] **IceCube** Collaboration, M.G. Aartsen et al., *Study of the Time-Dependence of the Cosmic-Ray Anisotropy with AMANDA and IceCube*, *Proc. 33rd ICRC*, Rio de Janeiro, Brazil (2013) [arXiv:1309.7006].
- [22] A.H. Compton and I.A. Getting, *An Apparent Effect of Galactic Rotation on the Intensity of Cosmic Rays*, *Phys. Rev.* **47** (1935) 817.
- [23] M. Ahlers, S.Y. BenZvi, P. Desiati, J.C. Díaz-Vélez, D.W. Fiorino, and S. Westerhoff, *A New Maximum-Likelihood Technique for Reconstructing Cosmic-Ray Anisotropy at All Angular Scales*, *Astrophys. J.* **823** (2016) 10.
- [24] **IceCube** Collaboration, J.C. Díaz-Vélez, [PoS \(ICRC2017\) 539](#) (these proceedings).

Sensitivity of IceCube Cosmic-Ray measurements to the hadronic interaction models

The IceCube Collaboration[†]

[†] http://icecube.wisc.edu/collaboration/authors/icrc17_icecube

E-mail: sam.deridder@ugent.be

The IceCube Neutrino Observatory measures cosmic-ray air showers with both its surface array IceTop and its 1.5-2.5 km deep in-ice array. IceTop measures the charge deposited by electromagnetic particles and low-energy muons. The highly abundant electromagnetic particles mainly determine the cosmic ray primary energy, while the low-energy muons, visible at the edge of the shower, add a sensitivity to the primary composition. The high-energy (>300 GeV) muon bundle is studied through its energy loss profile in the in-ice detector. These muons provide information about the early interactions of the cosmic ray in the atmosphere and thus to the mass of the primary particle. In this work we combine all three pieces of information. Since the yield of low- and high-energy muons differs significantly among existing hadronic interaction models, this provides a unique sensitivity to model dependent variations in cosmic-ray air shower studies.

Corresponding authors: Sam De Ridder¹, Emily Dvorak², Tom Gaisser³

¹ *Dept. of Physics and Astronomy, University of Gent, B-9000 Gent, Belgium*

² *Physics Department, South Dakota School of Mines and Technology, Rapid City, SD 57701, USA*

³ *Bartol Research Institute and Dept. of Physics and Astronomy, University of Delaware, Newark, DE 19716, USA*

*35th International Cosmic Ray Conference — ICRC2017
10–20 July, 2017
Bexco, Busan, Korea*

*Speaker.

1. Introduction

Indirect measurements of cosmic rays (CR) with energies > 1 PeV require a good understanding of the propagation of extensive air showers (EAS) in the atmosphere. This is a complex process with millions of particle interactions, so one needs to rely on simulations to relate experimental observables to the properties of the primary cosmic ray. Cosmic-ray interactions with nuclei in the atmosphere however occur around and above the highest energies that can be reached in present-day accelerators. The Large Hadron Collider (LHC) operates at a center-of-mass energy of 14 TeV, which corresponds to a lab-frame energy of roughly 100 PeV. On top of this, the very forward region with small transverse momenta of the secondary products of a collision is not well covered in the CMS and ATLAS detectors, while it is the most important region in cosmic ray physics. Air shower simulations thus need to rely on extrapolations of LHC data and fixed-target experiments at lower energies. This of course induces uncertainties in the interaction cross-sections, secondary particle type, multiplicity, particle momenta, etc. The assumptions and approximations used will influence the measurements of EAS properties by experiments.

Experiments reconstructing the cosmic-ray energy and mass use the variations between models used in simulations as a systematic uncertainty on their measurement. However, composition results between various experiments diverge significantly even with these systematic errors included. In particular, IceCube observes a rather heavy composition above 100 PeV to 1 EeV ([1]), while other experiments obtain a more light composition. In view of the uncertainties within the hadronic interactions, it is important to consider that these experiments measure different parts of the EAS. IceCube used the number of high-energy (> 300 GeV) muons as composition probe, while other experiments relate the muon content on the surface or the depth of the shower maximum to the primary mass.

In this work we study the extent to which varying results could arise from the fact that different experiments use different EAS observables. By comparing multiple observables within one single measurement, the internal (in)-consistencies concerning composition results within models can be examined. Here we will specifically focus on the comparison between a composition reconstruction using the surface detector array and in-ice measurements from the IceCube Neutrino Observatory (described in Sections 2 and 3). In particular, a composition estimation using the slope of the lateral distribution function at the surface is compared to the high-energy (HE) muon bundle information. The results obtained from these variables highly depend on the muon spectra produced in simulations, which differ among the hadronic interaction models (Section 4). The corresponding implications for the observables under study are shown in Section 5. In Section 6 data is added to compare whether the observables predict a similar composition behaviour under a given hadronic model.

2. Cosmic ray measurements with the IceCube Neutrino Observatory

The IceCube Neutrino Observatory [2] consists of a deep in-ice component "IceCube" (IC), together with a surface array called "IceTop" (IT) [3] (Figure 1). It is located at the geographic South Pole, at about 1 km from the Amundsen-Scott South Pole station. The in-ice component consists of 86 strings of which 78 have a standard inter-string spacing of 125 m. At depths between

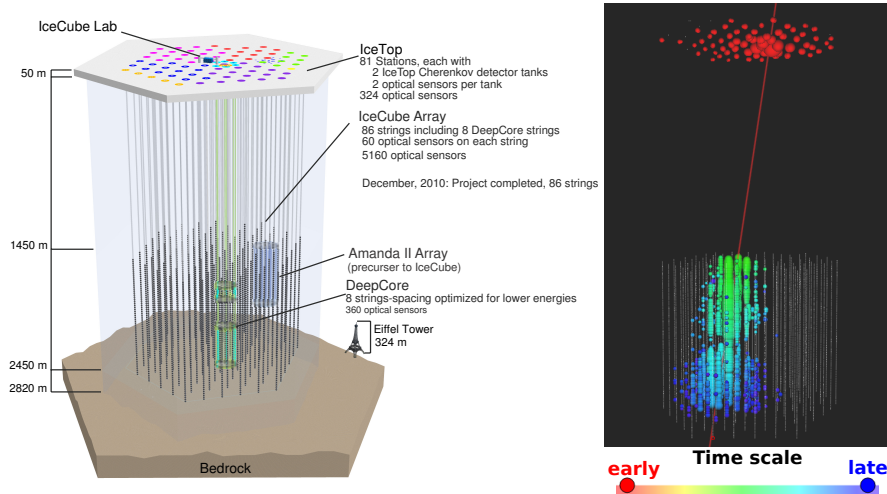


Figure 1: Schematic view of the IceCube Neutrino Observatory and its components, together with an illustration of the signal deposition by a real air shower event in both IceTop and IceCube.

1450 and 2450 meter below the Antarctic surface 60 digital optical modules (DOMs) are deployed on each string. In total IceCube covers a volume of 1 km^3 , which makes it very well suited for its primary goal: neutrino astronomy. At the surface above the in-ice detector 81 IceTop stations are deployed. Most stations are located close to the top of an IceCube string and hence they are spread over 1 km^2 with an inter-station distance of $\sim 125 \text{ m}$. Each IceTop station consists of two ice Cherenkov tanks with a 10 m separation. Operating these tanks in coincidence reduces a significant fraction of the background noise. In this work we only use the tank signals if such a coincident requirement between both tanks is fulfilled (called "hard local coincidence" or HLC hits). Calibration of the tanks is performed using the equivalent signal produced by a vertical muon going through the tank (VEM). The tanks themselves contain two DOMs which operate at different gains to increase the dynamic range for the detection of EAS ($O(0.1) - O(1000)$ VEM). The right plot of Figure 1 shows an example of a large EAS detection using IT and IC. Since IceTop is located at a height of 2835 m above sea level, its average atmospheric depth of 692 g/cm^2 is rather close to the depth of shower maximum for showers between 1 PeV and 1 EeV. This results in a large amount of EM particles, and accordingly, smaller statistical fluctuations. The abundant electromagnetic (EM) component and the low-energy muons first create a footprint on the IceTop array. The bundle of HE muons ($> 300 \text{ GeV}$), created in the first EAS interactions, travels 1.5 km through the ice and deposits energy along its track. The IceCube Neutrino Observatory is operational in its full configuration since May 2011. In this work only one month of data will be used to avoid influence of seasonal variations, being April 2013. This is a month from the second full year of data-taking for IceCube (May 2012 - May 2013), which corresponds to the data-taking year in the used simulations. The energy threshold at which cosmic ray detection becomes fully efficient for this data-taking year is $\log_{10}(E/\text{GeV}) = 6.4$. This threshold is slowly increasing with energy due to the accumulation of snow on top of the tanks. The effective detector area becomes too small for a detection of a significant rate of cosmic rays with energies $> 1 \text{ EeV}$. However, this work only focuses on the energy region up to $\sim 100 \text{ PeV}$.

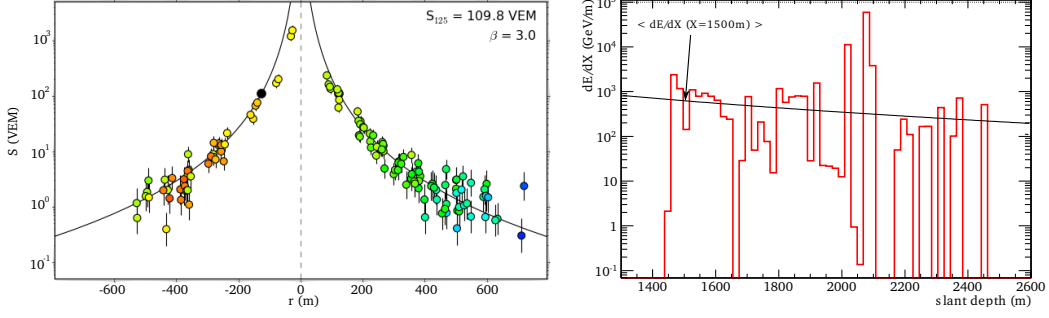


Figure 2: Left: Fit to the lateral charge distribution (LDF) in IceTop. Colours again indicate the time of the tank signal. Right: Fit to the energy loss profile along the track of the muon bundle in the ice.

3. EAS reconstruction

The air shower reconstruction performed here is very similar to the standard method used in IceTop analyses [3]. If 5 stations with HLC pulses survive after noise removal algorithms, a loglikelihood minimization technique tries to find the core position, direction (with zenith angle θ) and several parameters describing the shower. A lateral distribution function (LDF) is fitted to the charge as function of distance to the shower axis (R) (Figure 2), in combination with a curvature function describing the shower front time. The LDF used to fit the measured charges (S_{meas}) is a double logarithmic parabola:

$$S_{\text{meas}}(R) [\text{VEM}] = S_{125} \cdot \left(\frac{R}{125 \text{ m}} \right)^{-\beta - 0.303 \log_{10} \left(\frac{R}{125 \text{ m}} \right)} \cdot \exp \left(\frac{-d_{\text{snow}} \sec \theta}{\lambda} \right) \quad (3.1)$$

The two free parameters of this LDF are S_{125} and β , which are respectively the signal size and slope of the LDF at 125 m. The last part of Eq. 3.1 handles the attenuation of the signal due to the snow (with height d_{snow}) on top of each tank. The attenuation length λ is an effective attenuation length correcting both the muonic signal and EM signal, and its value is found to be 2.25 ± 0.2 m for this data-taking year. Next to the requirement of having at least 5 HLC stations after event cleaning, additional cuts are applied in order to ensure a set of properly described events on the surface. These cuts mainly concern the reconstruction quality and containment within the IceTop array. When the IceTop related cuts are fulfilled, the EAS trajectory reconstructed on the surface is used as muon bundle trajectory in the ice. Only hits that are related to the muon bundle track in time and space are selected to remove noise and random coincidences. If more than 8 in-ice HLC hits pass this procedure, a reconstruction of the energy loss profile along the track is performed, using the method described in [4] (Figure 2). A fit to this energy loss profile is performed in order to obtain a reliable energy loss reconstruction. The reconstructed energy loss at a slant depth of 1500 m in the ice (dE/dX_{1500}) is a good measure for the number of HE muons in the air shower. More cuts are applied to the in-ice energy loss reconstruction to ensure that the track traverses a significant part of the detector and that the reconstructed energy loss profile describes the measured light yield well. Furthermore, the fit to the energy loss profile must have converged.

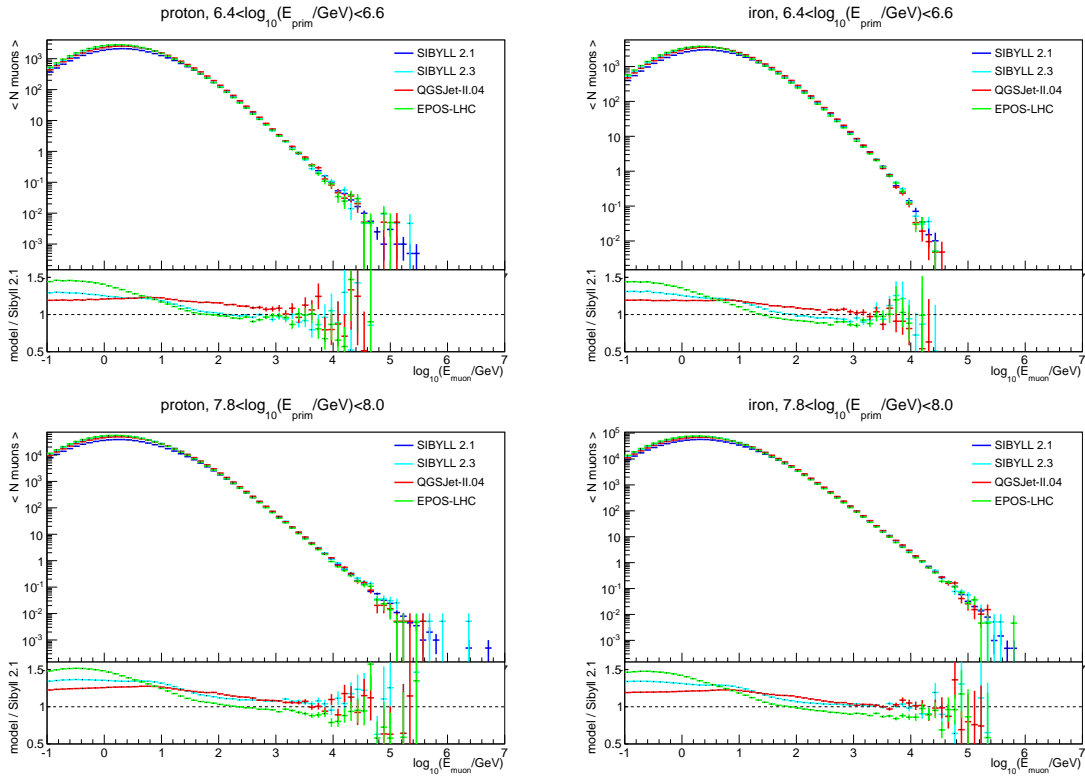


Figure 3: Spectrum of surface muons at South Pole altitude (692 g/cm^2 , April 2011 South Pole atmosphere) for proton and iron showers with zenith angles $< 40^\circ$ in two energy ranges. The spectra obtained with various hadronic models are shown, together with the ratio with respect to SIBYLL 2.1.

4. Hadronic interaction models

The simulation of the EAS development in the atmosphere is performed using the standard CORSIKA simulation package [5]. The atmospheric profile used in these simulations is the average South Pole atmosphere of April 2011, which represents the mean profile of an entire data-taking year. The propagation of the EM component is treated using EGS4, while hadronic interactions with energies $< 80 \text{ GeV}$ are modelled using FLUKA [6]. At higher energies, the hadronic interactions are modelled with SIBYLL 2.1 [7] in the standard dataset (with the largest statistics). The other hadronic models under study are the post-LHC models: SIBYLL 2.3 [8], QGSJet-II.04 [9] and EPOS-LHC [10]. These models are mainly tuned on the latest LHC data, but the most observable change for EAS measurements with IT-IC is their enhancement of muons. Figure 3 shows the resulting muon spectra that are obtained after simulations down to an atmospheric depth corresponding to the IceTop altitude (692 g/cm^2). The spectra are plotted for proton and iron primaries in two energy bins, and the various colors represent the different hadronic models. The bottom of each plot shows the muon number increase relative to SIBYLL 2.1. The curves show the average over many showers and error bars describe the error on the average. The number of low-energy muons increases for all new hadronic models, for both primaries and energy bins. The largest increase in LE (surface) muon number is observed for EPOS-LHC ($> 40\%$). This number increases

by $\sim 30\%$ and $\sim 20\%$ for respectively SIBYLL 2.3 and QGSJet-II.04. The change in the number of HE muons (> 300 GeV) is smaller. On average there seems to be a decrease of 5 – 10% for simulations using EPOS-LHC, while both QGSJet-II.04 and SIBYL 2.3 only show a very small, nearly negligible, increase in HE muon number relative to SIBYLL 2.1.

5. Parameter description and model sensitivity

The shower size parameter S_{125} scales with the number of (EM) particles in the shower and thus the energy of the primary particle. In this work, $\log_{10}(S_{125}/\text{VEM})$ ranges between 0.4 and 2, which roughly translates to a primary energy range of $6.4 < \log_{10}(E_{\text{prim}}/\text{GeV}) < 8$. 125 m as reference distance was chosen in order to minimize the dependence of this parameter to the primary composition. β , the slope of the LDF at this same radius, on the other hand does show sensitivity to the mass of the primary particle. EAS induced by heavier nuclei generally interact higher in the atmosphere and develop faster, or are older in terms of shower age, therefore the shower will be more spread out and the slope of the LDF is smaller. Additionally EAS initiated by heavier CRs contain more muons (both LE and HE) compared to lighter nuclei, which also results in a flatter LDF. Both these effects thus result in a composition sensitivity of β , where β is smaller for higher masses. The number of HE muons contained in the muon bundle is parametrized using the $\log_{10}(dE/dX_{1500})$ observable. Since the number of HE muons in a shower increases with primary composition, also this variable shows a composition sensitivity. Both variables change linearly with $\log(A)$, where A is the mass number of the primary particle. The variables are clearly complementary in a reconstruction of the primary cosmic ray composition, since they are sensitive to various parts of the EAS. The distributions of both variables β and $\log_{10}(dE/dX_{1500})$ within a certain $\log_{10}(S_{125})$ bin are fitted with a gaussian distribution. For both variables, the spread decreases with energy. The mean values of these gaussian fits are shown in Figure 4 as function of $\log_{10}(S_{125})$ for both β and $\log_{10}(dE/dX_{1500})$. Again, the error bars show the error on the mean. The solid (dashed) lines show proton (iron) and the separation between the two indicates a clear composition sensitivity of both variables.

The results obtained with the various hadronic models are shown as the various colours, and the difference with SIBYLL 2.1 is plotted on the bottom. The difference between QGSJet-II.04, SIBYLL 2.3 and SIBYLL 2.1 concerning HE muons is small (Figure 3), which results in a negligible change in the measured energy loss in the ice. For EPOS-LHC on the other hand a significant reduction can be observed. The decrease in β with regard to SIBYLL 2.1 is observable for all post-LHC hadronic interaction models. Again EPOS-LHC shows the largest shift. This decrease is mostly correlated with the increased number of surface muons discussed in Section 4.

The observed light yield, and thus the reconstructed energy loss, highly depends on the properties of the ice. The uncertainty on those properties will result in a systematic error on $\log_{10}(dE/dX_{1500})$. In this work the systematic errors caused by scattering and absorption uncertainties in the main ice, the scattering length of the refrozen ice surrounding the strings, and the efficiency of the DOMs are combined into a general light yield error of -12.5% and + 9.6%. The uncertainty of the snow attenuation length (0.2 m) is combined with the systematic error due to the uncertainty of the calibration of the tanks ($\pm 3\%$). Both of these mainly influence the signal size S_{125} , while the composition sensitive variables are almost unaffected.

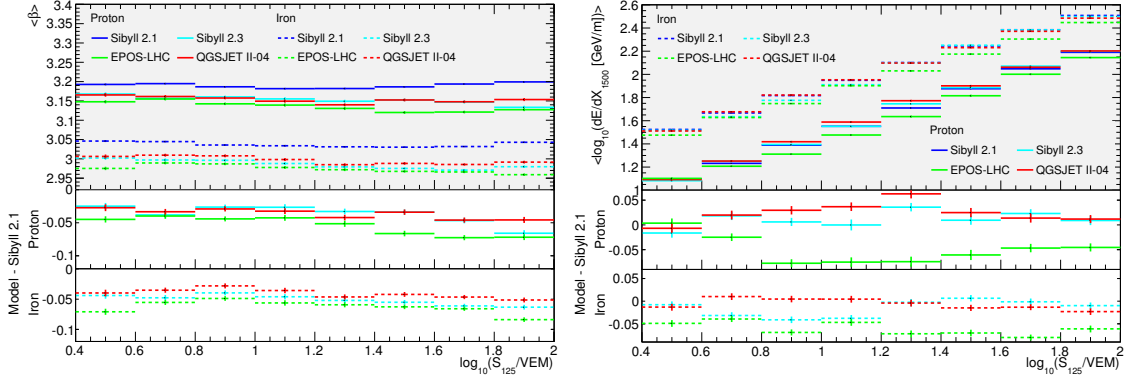


Figure 4: Evolution of the average β and dE/dX_{1500} as function of S_{125} for proton and iron simulations with the various hadronic interaction models. On the bottom the shift with respect to SIBYLL 2.1 is shown.

6. Results and discussion

When the simulations describe the data well, measured data curves should be somewhere in between simulated proton and iron curves, or at least very close to them. To compare the data results of the two variables (β and $\log_{10}(dE/dX_{1500})$), we plot the relative position of data within the proton-iron space for each variable. When data is similar to proton (iron) for a certain variable, it has a value close to 0 (1). If a consistent composition is measured between the two variables, the two curves should overlap. The resulting comparison of the curves is shown Figure 5 for each of the hadronic interaction models. The systematic error bars correspond to the ones described in the previous section. The light yield uncertainty in the ice dominates our systematics.

A clear behaviour that can be seen in all of these plots is that the curves for both variables rise with S_{125} and thus with energy, indicating an increasingly heavy composition. In this energy range (from roughly 2.5 PeV to 100 PeV) this has been observed by all experiments. According to which hadronic interaction model is used, these plots show a varying agreement between the two observables. For both SIBYLL 2.3 and QGSJet-II.04, a consistent interpretation is obtained between the two parameters. In this case a composition measurement using an observable sensitive to shower age and the muonic component on the surface agrees with a measurement of the in-ice energy loss caused by the HE muons, which is of great importance. Results obtained with simulations using SIBYLL 2.1 and EPOS-LHC on the other hand show some discrepancy concerning these measurements. Namely the lower number of LE muons on the surface in SIBYLL 2.1 causes the measured slope of the LDF to give a heavier composition than the signal in deep ice. In the case of EPOS-LHC, the decreased number of HE muons combined with the $\sim 50\%$ increase in the LE muon number leads to the opposite inconsistency. From this it can be concluded that it is of crucial importance to understand and take into account the variations within certain models and in between models, especially when cosmic-ray composition results are compared where different properties of the extensive air showers are used to reconstruct the primary cosmic-ray mass.

More work is in progress to extend the energy range in this work to higher energies. In the full analysis, more data and simulations will be used. In addition a direct measurement of the surface muons [11] will be added as separate observable.

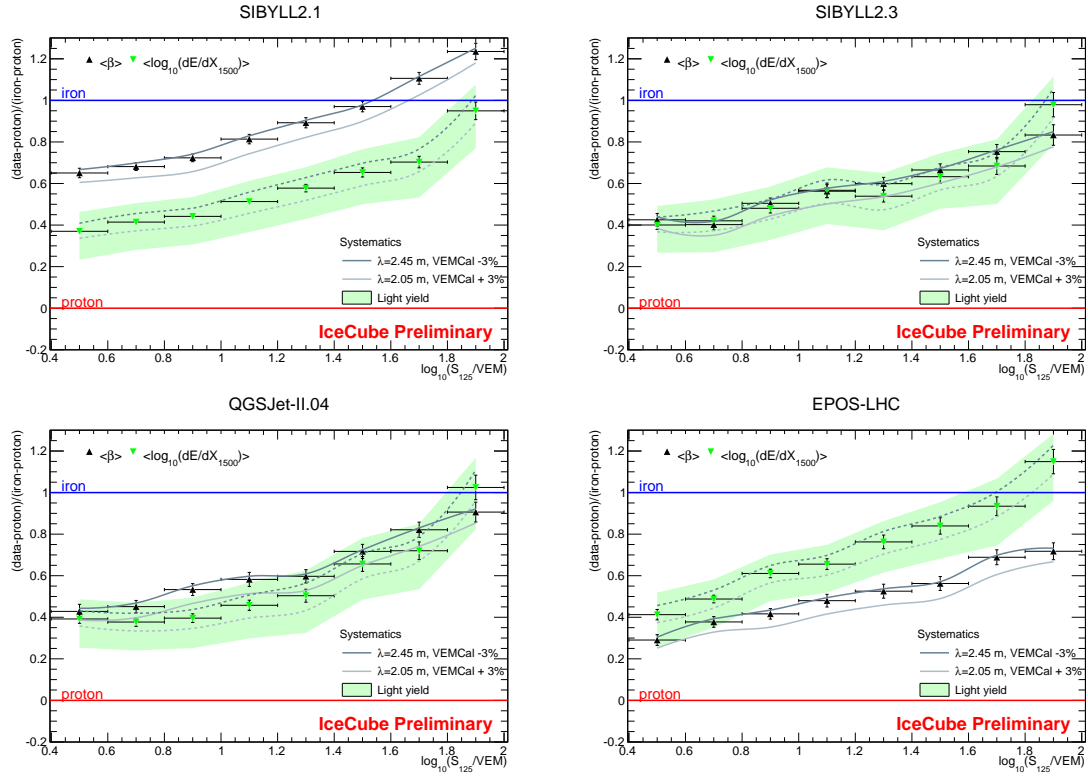


Figure 5: Distribution of the average of the β and $\log_{10}(dE/dX_{1500})$ measurements as function of S_{125} in the proton-iron space. Each figure shows the results obtained with a certain hadronic model. The green band shows the in-ice light yield systematic, while the solid and dotted grey curves indicate uncertainties mainly in the energy scale from IceTop reconstructions.

References

- [1] **IceCube** Collaboration, K. Rawlins, *J. Phys. Conf. Ser.* **718** (2016) 052033.
- [2] **IceCube** Collaboration, A. Achterberg et al., *Astropart. Phys.* **26** (2006) 155–173.
- [3] **IceCube** Collaboration, R. Abbasi et al., *Nucl. Instrum. Meth.* **A700** (2013) 188–220.
- [4] **IceCube** Collaboration, M. G. Aartsen et al., *JINST* **9** (2014) P03009.
- [5] D. Heck et al., *CORSIKA: A monte carlo code to simulate extensive air showers*, tech. rep., 1998.
- [6] A. Ferrari, P. R. Sala, A. Fasso', and J. Ranft, *CERN-2005-10* (2005). INFN/TC_05/11, SLAC-R-773.
- [7] E.-J. Ahn, R. Engel, T. K. Gaisser, P. Lipari, and T. Stanev, *Phys. Rev. D* **80** (Nov, 2009) 094003.
- [8] F. Riehn, R. Engel, A. Fedynitch, T. K. Gaisser, and T. Stanev, *PoS (ICRC2015)* **558** (2016).
- [9] S. Ostapchenko, *Phys. Rev.* **D83** (2011) 014018.
- [10] T. Pierog, I. Karpenko, J. M. Katzy, E. Yatsenko, and K. Werner, *Phys. Rev.* **C92** (2015) 034906.
- [11] **IceCube** Collaboration, H. P. Dembinski and J. Gonzalez, *PoS (ICRC2015)* **267** (2016).

GeV Solar Energetic Particle Observation and Search by IceTop from 2011 to 2016

The IceCube Collaboration[†], Pierre-Simon Mangeard[‡], Pradiphat Muangha[‡], Roger Pyle[‡], David Ruffolo[‡], and Alejandro Sáiz[‡]

[†] http://icecube.wisc.edu/collaboration/authors/icrc17_icecube

[‡] *University of Delaware, Newark Delaware USA*

[‡] *Mahidol University, Bangkok Thailand*

[‡] *Pyle Consulting Group, St. Charles Illinois USA*

E-mail: evenson@udel.edu

Only three Ground Level Enhancements (GLEs) produced by GeV-range solar energetic particles have been confirmed in the present solar cycle, and those have been quite small by historical standards. At the same time direct observations of high energy solar particles from spacecraft have become available. The combination of instruments at the Amundsen - Scott Station at the geographic South Pole offers an opportunity to span the two disparate sets of measurements. Operating at high altitude and low geomagnetic cutoff the neutron monitor at Pole has nevertheless traditionally been accepted as making a "ground level" observation. An enhanced array of bare neutron detectors and IceTop (surface ice Cherenkov detectors in the IceCube Neutrino Observatory) in principle allow spectral information to be extracted from events that previously were too small to use geomagnetic techniques to obtain spectra. We report our spectral measurements for the three confirmed GLE and compare them to other available data on these events. We also present preliminary results of an ongoing study of 34 particle events selected to have significant enhancements in the > 100 MeV channel in GOES data in terms of possible detections and sensitivity limits.

Corresponding author: Paul Evenson*

University of Delaware, Newark Delaware USA

*35th International Cosmic Ray Conference - ICRC2017
10-20 July, 2017
Bexco, Busan, Korea*

*Speaker.

1. Introduction

The only Solar Energetic Particle (SEP) events of relevance to radiation hazards at aircraft altitude are so called Ground Level Enhancements (GLE). GLE can also provide advance warning of lower energy SEP that are primarily responsible for damage to spacecraft [8]. With precision transport modeling [10] it is possible to infer the time profile of acceleration to GeV energies and investigate mean free paths and unusual transport conditions (such as magnetic bottlenecks and loops) in the interplanetary medium [2].

Spaceborne detectors [3, 1] now approach the energy range of ground based detectors. In fact AMS-02 has approximately the same collecting power as the South Pole neutron monitor. It has much better energy and composition sensitivity, but only “looks” in one constantly changing direction at a time. The duration of one orbit is much longer than the timescale of the evolution of anisotropy in a typical solar event. Therefore the network of ground based detectors will remain a vital partner for the life of AMS-02, and will continue observations beyond the planned end of the AMS-02 mission. It is important that systematic investigation of GeV solar particle events remain firmly rooted in this ground based network. Detectors such as IceTop, enhanced neutron detectors at the South Pole [4], and the new neutron monitor at Dome C [9] are important recent additions to this network.

Unfortunately just as these new tools have become available, the number of GLEs during the past solar maximum has been extremely low compared to that in previous solar cycles. Only three GLE have been reported; two are commonly accepted [7, 12] and one is considered problematic [9] because it was not detected by sea level instruments. A question of fundamental importance is whether the paucity of GLEs in the present solar cycle is due to the overall SEP flux of the events, or instead is a spectral effect. To investigate this question we have undertaken to use data from IceTop and from the neutron detectors at the South Pole to understand event systematics. In this paper we discuss our initial event selection and preliminary results. Characterization of the energy spectra and quantitative detection limits are a work in progress.

1.1 IceTop Tanks

IceCube is a cubic-kilometer scale neutrino detector completed in 2010 installed at the geographic South Pole [6]. Reconstruction of the direction, energy and flavor of the neutrinos relies on the optical detection of Cherenkov radiation emitted by charged particles produced in the interactions of neutrinos in the surrounding ice or the nearby bedrock. The Cherenkov light is measured by Digital Optical Modules (DOMs) containing photomultipliers deployed in the ice between depths of 1450 m and 2450 m. IceTop, the surface component of IceCube, is an air shower array with 81 stations. Each station consists of two Cherenkov detector “tanks” which are 2600 kg blocks of clear ice containing standard IceCube DOMs. One DOM in each tank is operated at high gain and the other at low gain in order to extend the dynamic range of the tank. To measure GeV cosmic ray fluxes we use count rates from two discriminators in each high gain DOM, termed SPE (Single Photo Electron) and MPE (Multi Photo Electron). The SPEs are set at selected thresholds ranging between 1 and 20 photoelectrons, while the MPEs are all set near 20 photoelectrons. Changing the discriminator level on a DOM “tunes” the response function of the DOM as illustrated in Figure

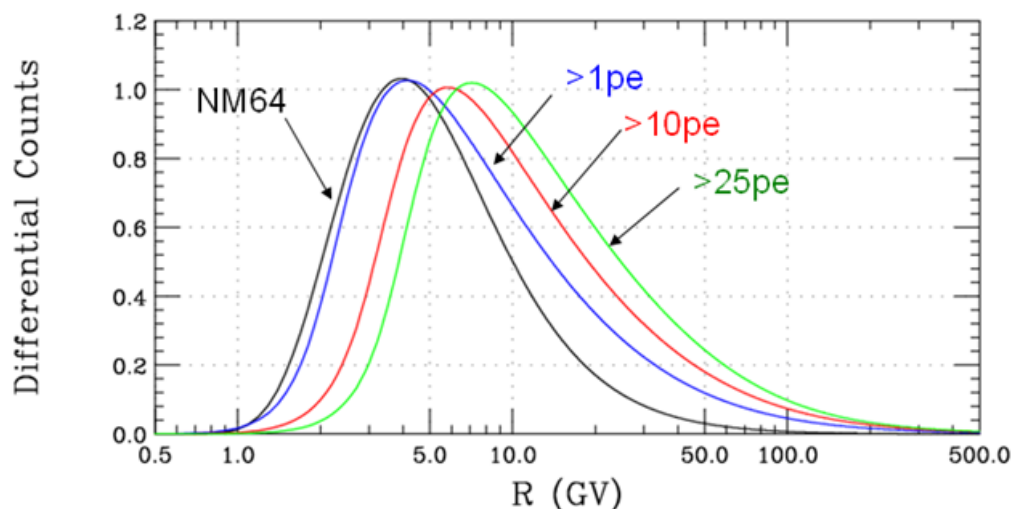


Figure 1: Illustration of response functions of neutron monitor and IceTop tanks for zero GV geomagnetic cutoff and the typical pressure altitude at the South Pole. Calculations were done using FLUKA and GEANT for galactic cosmic ray spectra and composition appropriate to solar minimum modulation conditions.

1. Comparing the counting rates of the various discriminators allows determination of the energy spectrum of the incident particles [7].

1.2 South Pole Neutron Monitor and Polar Bare

There is also a 3NM64 neutron monitor [5] at the South Pole with response (also shown in Figure 1) peaking at lower energy than any of the IceTop thresholds. Lead free neutron detectors at Pole, that we refer to as the “Polar Bares” although a more common name is “Moderated Neutron Detectors” respond to still lower energy [11]. The Bare to Monitor Ratio and the increase in the count rate of either have traditionally been used to identify small GLE [8].

2. Methodology

2.1 GOES Event Selection

In this analysis, we search for GLEs using five years of IceTop and South Pole neutron monitor data. High energy (above 1 GeV) particles responsible for GLEs are almost always part of a steeply falling but continuous spectrum extending to much lower energy. We therefore base our event selection on observations of lower energy protons by the GOES geostationary satellites. We use 5-minute averaged integral proton fluxes for energy thresholds of 10 MeV, 50 MeV, and 100 MeV. We chose events where the peak of GOES >100 MeV proton flux was 0.14 pfu (particle flux unit; $1 \text{ particle cm}^{-2} \text{ sr}^{-1} \text{ s}^{-1}$) because this selection produced cleanly defined onset times. A total of 34 events were found during 2011 to 2016, as listed in Table 2.1. The three known GLE are highlighted in the table. After the events were chosen based on the peak flux, the onset time was

taken as the first measurement clearly above the background. These onset times, as listed in Table 2.1, were used to search for further GLEs that may have escaped independent detection.

YYYY/MM/DD	HH:MM	YYYY/MM/DD	HH:MM	YYYY/MM/DD	HH:MM	YYYY/MM/DD	HH:MM
2011/03/21	03:45	2012/01/27	18:30	2012/09/28	01:15	2014/01/07	19:20
2011/06/07	06:50	2012/03/07	01:30	2013/04/11	07:55	2014/02/20	08:00
2011/08/04	04:20	2012/03/13	17:35	2013/04/24	23:45	2014/02/25	03:30
2011/08/09	08:10	** 2012/05/17 **	01:50	2013/05/22	13:20	2014/04/18	13:20
2011/09/06	03:00	2012/07/07	00:00	2013/09/30	02:30	2014/09/01	21:55
2011/09/06	23:05	2012/07/08	18:00	2013/10/28	18:30	2014/09/10	21:25
2011/09/23	03:20	2012/07/12	17:05	2013/11/02	08:35	** 2015/10/29 **	02:55
2011/11/04	00:05	2012/07/19	06:40	2013/12/28	18:50		
2012/01/23	04:10	2012/07/23	08:30	** 2014/01/06 **	08:00		

Table 1: List of events where greater than 100 MeV protons were clearly detected by the GOES spacecraft. Events previously identified as GLE are indicated with yellow shading and “**”. The times given are the onset times used in the analysis.

2.2 IceTop Analysis

Figure 2 shows GLE 71, which occurred on 2012 May 17, as observed by IceTop and the neutron detectors. In the left panel the top traces shows the summed counting rate of the 12 bare neutron detectors and the 3NM64 (kHz). Then there are traces the IceTop DOMs grouped in order of increasing threshold (i.e. decreasing count rate): SPEa, SPEb, SPEc, SPEd, and MPE. These are expressed as the average counting rate per DOM in kHz. The lower panel shows the GOES proton fluxes above three energy thresholds. The steep energy spectrum of the GLE is evident from the pattern of the increases which are quite pronounced at the low thresholds and nearly invisible at the high thresholds.

We use counting rate as a proxy for discriminator setting and also as a simple correction for snow accumulation on the tank. In other words we assume that the reduction in counting rate due to snow accumulation changes the response in the same way as a similar reduction in count rate due to increasing the threshold. This approximation is discussed in more detail by [7] where we also present a preliminary energy spectrum for this event.

In order to conduct a systematic and quantitative search for high energy particles we compare an interval where they might be expected with an immediately preceding interval assumed to contain only background. The dividing line between the two intervals and the length of the intervals were chosen to maximize the visibility of the three established GLE, and then were applied uniformly to the remaining 31 events to conduct the search. The dividing line is always 10 minutes prior to the GOES onset.

Figure 2 shows “base” and “pulse” intervals as well as the GOES onset indicated by the dashed line. We define two statistics, the first is the fractional change of a count rate ratio. For this, both the pulse and base intervals are taken to be 60 minutes. The rate ratio itself, defined by $R_S = (SPEa + SPEb)/(SPEc + SPEd)$, is computed for each minute as shown in the top right panel of Figure 2. For the survey, R_S is averaged over both pulse (R_{SP}) and base (R_{SB}) intervals. The fractional change in the ratio is then $(R_{SP} - R_{SB})/R_{SB}$.

The second statistic is formed from a plot of the fractional change in counting rate of each DOM as a function of the average counting rate of the DOM. This is illustrated in the lower right panel of Figure 2. In this case the averages were taken over 50 minutes. The statistic is the slope of a straight line fit to the distribution, also shown in the figure. (The linear fit appears as a curve on the linear vs. log axes of the figure) Although seemingly closely related, these two statistics are not tightly correlated for background events, as discussed below.

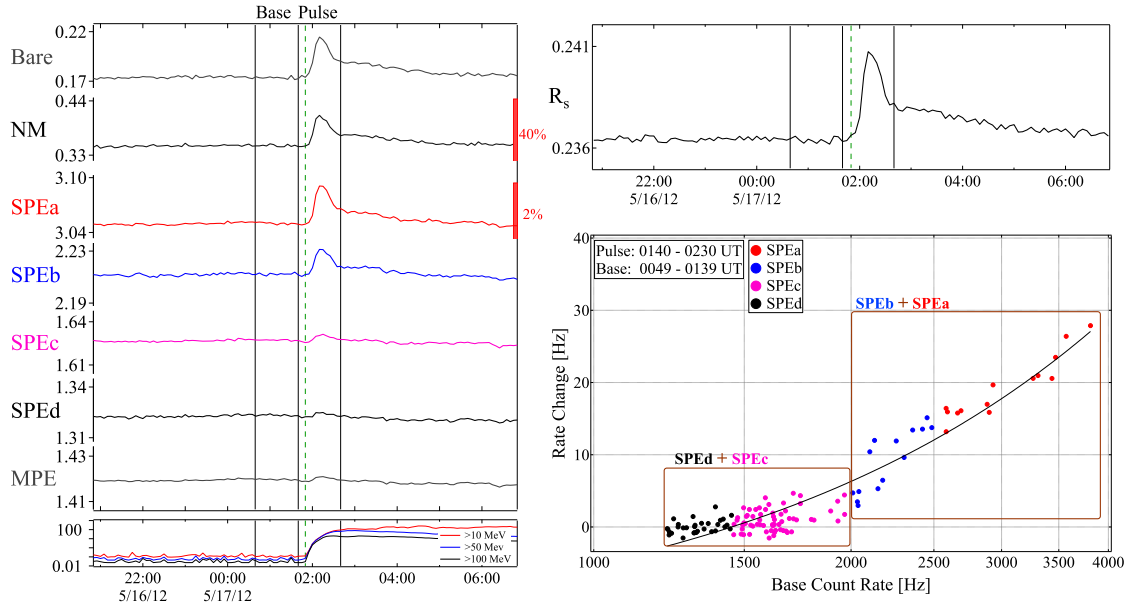


Figure 2: The ground level enhancement (GLE71) on 2012 May 17. Left: Observations at South Pole and GOES Spacecraft. Right Top: Analysis to produce ratio parameter. Right Bottom: Analysis to produce ratio parameter. (Horizontal axis on log scale and vertical axis on linear scale.) See text for details.

2.3 South Pole Neutron Monitor and Polar Bare Analysis

The Polar Bares respond to lower energy particles on average than the NM64. The fractional Bare to Monitor ratio and the fractional increase in the count rate of the monitors form a pair of parameters that have traditionally been used to search for small GLE. We use these two parameters, constructed for the same 60 minute intervals as the IceTop ratio statistic, as an alternate method of searching for small GLE, representative of the traditional approach.

3. Results

Figure 3 compares the IceTop analysis with the neutron monitor analysis as scatter plots of the two parameters defined for each. The May 2012 (GLE71) event stands out clearly. Both the January 2014 (GLE72) and October 2015 (GLE73) events lie outside the cluster near the origin if one considers the joint distribution of both parameters, although there are larger fluctuations in either parameter separately. As noted above, the two parameters are not tightly correlated in cases where there is no clear observation of energetic particles.

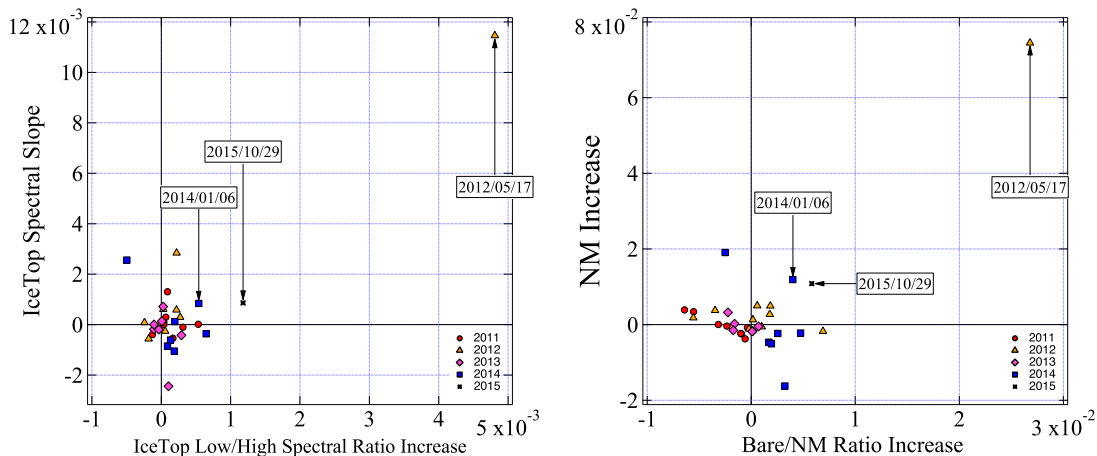


Figure 3: Left: IceTop spectral slope against IceTop spectral ratio. See text for details. Right: Neutron Monitor increase against Bare to Monitor Ratio.

The October 2015 event is barely detected, as the full analysis presented in Figure 4 shows. The identification of this event as GLE73 is supported by the simultaneous detection by the neutron monitor at Dome C in Antarctica [9]. Recognition as GLE73 is in fact debated within the community since it was not detected by any sea level neutron monitors. This therefore probably represents the smallest event that can be detected as a GLE.

Although the two search parameters for IceTop are mostly uncorrelated in the “background” region it is curious that the IceTop spectral ratio parameter clearly has more positive values than negative. It is tempting to speculate that this might indicate the presence of low fluxes of high energy particles as a general feature but we rather think that it is due to some kind of structure in the background.

An example of such a structured background would be the well known Forbush decreases, which have the property that they produce rapid decreases in the counting rate followed by slow increases. The net result is that for intervals chosen at random the count rate is more likely to be increasing rather than decreasing. We would have to investigate whether such an effect might be present in the IceTop ratio before drawing any conclusions. Unfortunately such an investigation is itself not well defined since solar particle events are seldom isolated events. Large events in particular often come in clusters accompanied by major, correlated perturbations of the solar wind.

In this search the monitor data are essentially statistics limited, with the South Pole monitor counting at roughly 300 Hz. In contrast, an IceTop DOM at MPE threshold counts at approximately 1.2 kHz, giving the entire array of 162 tanks at least a factor of ten better statistical accuracy. Unfortunately for this work the increased statistical precision has revealed true fluctuations in the background approximately the same size as the statistical fluctuations in the neutron monitors. Figure 4 shows this clearly, particularly for the higher thresholds where the rates during the pulse interval are clearly *lower* than during the baseline interval. In this case, however, the change in the spectral ratio is still giving a rather clear indication that solar particles are present.

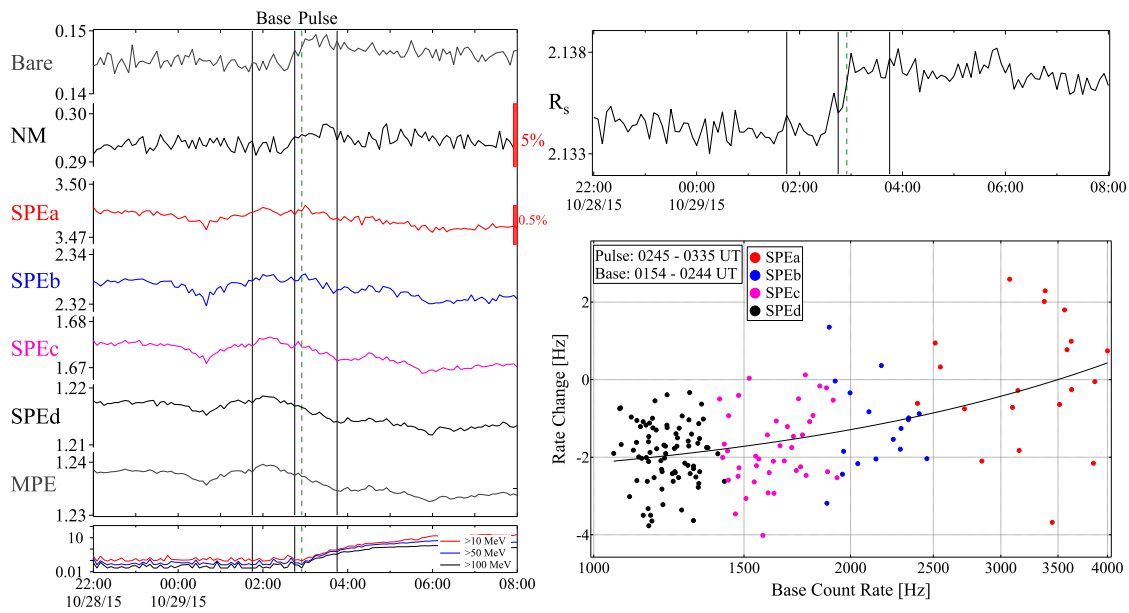


Figure 4: The small ground level enhancement (GLE73) on 2015 October 29.

4. Summary and Conclusions

Our analysis of 34 solar particle events selected for the presence of greater than 100 MeV protons at a GOES spacecraft revealed no definitive GLE other than the ones already known. GLE73, on 2015 October 29 is probably the smallest GLE that could be detected with any degree of certainty. A truly quantitative statement in terms of absolute particle fluxes is not possible because the visibility of the increase depends on the time structure of the event and the asymptotic direction of the detector. IceTop and the Antarctic neutron monitors have similar sensitivity limits for GLE detection although for different reasons. The monitors are statistics limited, but the greater statistical precision of IceTop has revealed true fluctuations in the background approximately the same size as the statistical fluctuations in the neutron monitors. The silver lining to this is that the better statistical accuracy of IceTop will allow a more detailed study of cosmic ray fluctuations, sometimes called “scintillations”, than has previously been possible.

5. Acknowledgements

Supported in part by US National Science Foundation awards PLR-1245939 and PLR-1341562 and their predecessors, as well as grant RTA5980003 from the Thailand Research Fund.

References

- [1] Adriani, O., G.C. Barbarino, G.A. Bazilevskaya *et al.*, Observations of the 2006 December 13 and 14 solar particle events in the 80 MeV/N \bar{U} 3 GeV/N range from space with the PAMELA detector, *Astrophysical Journal* **742** (2011) 102-112, doi:10.1088/0004-637X/742/2/102.

- [2] Bieber, John W., Wolfgang Droege, Paul A. Evenson, Roger Pyle, David Ruffolo, Udomsilp Pinsook, Paisan Tooprakai, Mani Rujiwarodom and Thirane Khumlumlert, Energetic particle observations during the 2000 July 14 solar event, *Astrophysical Journal* **567** (2002) 622-634.
- [3] Bindi, V., Solar energetic particles measured by AMS-02, *International Cosmic Ray Conference 34*, The Hague, Netherlands, (2015) PoS(ICRC2015)108.
- [4] Evenson, Paul, John Bieber, John Clem and Roger Pyle, South pole neutron monitor lives again, *International Cosmic Ray Conference 32*, Beijing, (2011).
- [5] Hatton, C. J., The Neutron Monitor, *Progress in Elementary Particle and Cosmic Ray Physics X* (1971), American Elsevier Publishing Company, New York.
- [6] **IceCube** Collaboration, M. G. Aartsen et al., The IceCube Neutrino Observatory: Instrumentation and Online Systems, *JINST* **12** (2017) P03012.
- [7] **IceCube** Collaboration, Ground level enhancement of May 17, 2012, observed at South Pole, Paper 0368, *International Cosmic Ray Conference 33*, Rio De Janeiro, (2013).
- [8] Oh, S.Y., J.W. Bieber, J. Clem, P. Evenson, R. Pyle, Y. Yi, and Y.K. Kim, South Pole neutron monitor forecasting of solar proton radiation intensity, *Space Weather* **10** (2012), S05004, doi:10.1029/2012SW000795.
- [9] Poluianov, Stepan, Ilya Usoskin, Alexander Mishev, Harm Moraal, Helena Krüger, Giampietro Casasanta, Rita Traversi, Roberto Udisti, Mini neutron monitors at concordia research station, Central Antarctica, *J. Astron. Space Sci.* **32(4)** (2015), 281-287 <http://dx.doi.org/10.5140/JASS.2015.32.4.281>.
- [10] Sáiz, Alejandro, Paul Evenson, David Ruffolo, and John W. Bieber, On the estimation of solar energetic particle injection timing from onset times near earth, *Astrophysical Journal* **626** (2005) 1131-1137.
- [11] Stoker, P.H., Spectra of solar proton ground level events using neutron monitor and neutron moderated detector recordings, *International Cosmic Ray Conference 19*, La Jolla **4** (1985) 114-117.
- [12] Thakur, N., N. Gopalswamy, H. Xie, P. Makela, S. Yashiro1, S. Akiyama, and J. M. Davila, Ground level enhancement in the 2014 january 6 solar energetic particle event, *Astrophysical Journal Letters* **790** (2014) L13-17.

Impulsive Increase of Galactic Cosmic Ray Flux Observed by IceTop

The IceCube Collaboration[†], Pierre-Simon Mangeard[‡], Pradiphat Muangha[‡], Roger Pyle[‡], David Ruffolo[‡], and Alejandro Sáiz[‡]

[†] http://icecube.wisc.edu/collaboration/authors/icrc17_icecube

[‡] *University of Delaware, Newark, DE 19716, USA*

[‡] *Mahidol University, Bangkok 10400, Thailand*

[‡] *Pyle Consulting Group, St. Charles, IL 60174, USA*

E-mail: evenson@udel.edu

On 2017 January 18 scaler rates in the IceTop detectors at the South Pole revealed an impulsive increase in the galactic cosmic ray flux lasting a few hours. In addition to the neutron monitor at Pole the event was detected clearly by the Mawson neutron monitor and faintly at Jang Bogo. No other neutron monitors appear to have seen the increase. The event was in many ways reminiscent of the 2015 June 22 event observed by the GRAPES muon detectors. Both events occurred during the declining phase of a Forbush decrease, at a time of increasing geomagnetic activity, and were observed by a limited number of neutron monitors with similar asymptotic directions. The magnitude of the impulse was in both cases such that the flux returned briefly to approximately the pre-decrease level. Distinctly unlike the 2015 June 22 event, a changing geomagnetic cutoff cannot explain the 2017 January 18 event because the cutoff at South Pole is nearly zero and the detector response is atmosphere limited. We therefore interpret the 2017 January 18 event in terms of the structure of the Forbush decrease and (possibly changing) asymptotic directions. With our interpretation of the January event in mind we also comment on possible alternative interpretations of the GRAPES event.

Corresponding author: Paul Evenson*
University of Delaware, Newark, DE 19716, USA

*35th International Cosmic Ray Conference
10-20 July, 2017
Bexco, Busan, Korea*

*Speaker.

1. Introduction

IceCube is a cubic-kilometer scale neutrino detector completed in 2010 installed at the geographic South Pole [3]. Reconstruction of the direction, energy and flavor of the neutrinos relies on the optical detection of Cherenkov radiation emitted by charged particles produced in the interactions of neutrinos in the surrounding ice or the nearby bedrock. The Cherenkov light is measured by Digital Optical Modules (DOMs) containing photomultipliers deployed in the ice between depths of 1450 m and 2450 m. IceTop is an air shower array with 81 stations located above the in ice installation. A station consists of two Cherenkov “tanks” which are 2000 kg blocks of clear ice using standard DOMs to measure Cherenkov radiation emitted by secondary charged particles. One DOM in each tank is operated at high gain and the other at low gain in order to extend the dynamic range of the tank.

To measure GeV cosmic ray fluxes we use count rates from two discriminators in each high gain DOM, termed SPE (Single Photo Electron) and MPE (Multi Photo Electron). The SPE are set at selected thresholds ranging between 1 and 20 photoelectrons while the MPE are all set near 20 photoelectrons. Setting the discriminator level on a DOM “tunes” the response function of the DOM. The array of different thresholds allows determination of the energy spectrum and time structure of variations in the interplanetary cosmic ray flux. See [4] for a more extensive discussion of the energy response of IceTop. There is also a 3NM64 neutron monitor [2] at the South Pole with response peaking at lower energy than any of the IceTop thresholds. Lead free neutron detectors with yet lower energy response that we refer to as the “Polar Bares” (although a more common name is “Moderated Neutron Detectors”) [9] are installed in the main station. For details of the neutron detectors at the South Pole see [1].

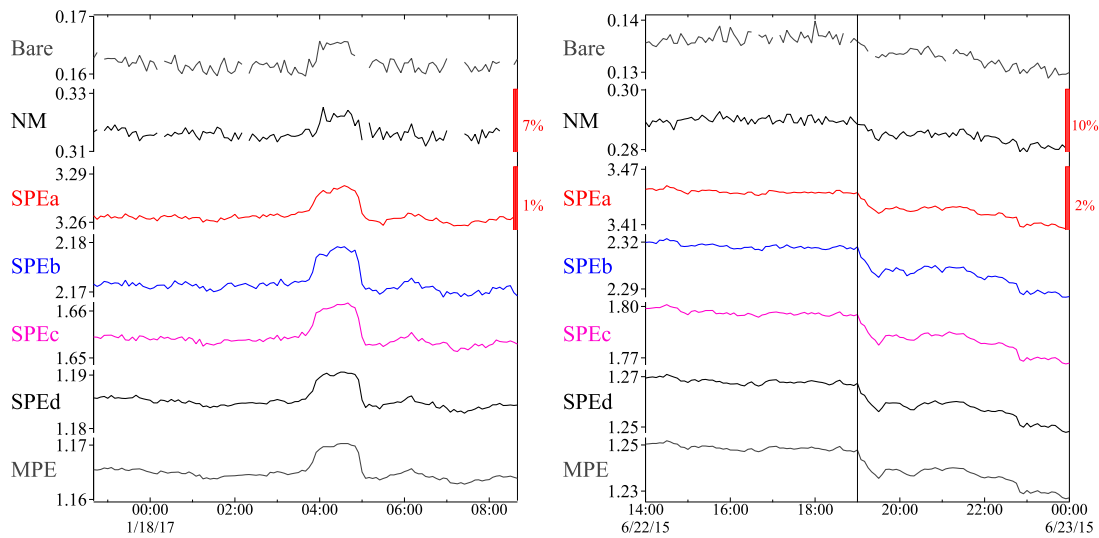


Figure 1: Left: Impulsive increase in cosmic ray flux seen by IceTop and the South Pole neutron detectors on 2017 January 18. Right: IceTop response at the time of the impulsive increase reported by GRAPES on 2015 June 22. All plots are logarithmic with rates expressed in kHz.

On 2017 January 18 IceTop observed the impulsive increase in the cosmic ray flux illustrated at the left in Figure 1. In this figure the top two traces show the total count rate of the moderated

neutron detectors and 3NM64 neutron monitor respectively, while the next five traces give the average counting rate of IceTop DOMs grouped in order of increasing threshold. The similar-sized increase at all thresholds in IceTop and neutron detectors indicate that the impulsive increase has a hard spectrum, very close to that of the galactic cosmic rays. A small enhancement was also seen at the nearby neutron monitors at Mawson and Jang Bogo, but no others. Thus it is evidently a highly anisotropic fluctuation in the galactic cosmic rays – as opposed to a Ground Level Enhancement (GLE) resulting from solar energetic particles (SEP).

The event seen by IceTop was in many ways reminiscent of the 2015 June 22 pulse event observed by the GRAPES-3 tracking muon telescope in Ooty, India [7]. Both the IceTop and GRAPES events occurred during the declining phase of a Forbush decrease, at a time of increasing geomagnetic activity, and were observed by a limited number of neutron monitors with at similar geographic locations. The magnitude of the impulse was in both cases such that the flux returned briefly to approximately the pre-decrease level. An explanation proposed for the GRAPES event [7] is a temporary reduction in the geomagnetic cutoff amounting to 0.5 GV to 0.7 GV depending on the incident direction of the particles.

On the right in Figure 1 we show data from the South Pole detectors at the time the pulse event was observed by GRAPES. Since any SEP event gives a much stronger increase at low cutoff rigidity the absence of an increase at South Pole definitively confirms that the event is not a classic GLE. The clear depression in count rates at the South Pole at the time of the start of the GRAPES pulse (vertical line) was presumably produced by the same magnetic disturbance. Since the cutoff is zero at the South Pole, and therefore cannot decrease, the lack of a pulse in and of itself does not contradict the explanation proposed [7] for the GRAPES event.

However, by the same logic, a changing geomagnetic cutoff cannot explain an increase such as seen on 2017 January 18. The only explanation for the 2017 January 18 event is a significant anisotropy in the interplanetary cosmic ray flux. Whether the anisotropy was transient in time or was a result of changing asymptotic directions due to the active geomagnetic conditions at that time cannot be decided. With this picture of the 2017 January 18 event in mind we propose that the GRAPES event also was a manifestation of interplanetary anisotropy rather than a cutoff variation. Primarily we argue that a cutoff variation would make predictions for the world network of neutron monitors that are not in accord with observations.

2. Geomagnetic Cutoff Variations

The Princess Sirindhorn Neutron Monitor (PSNM) on Doi Inthanon in Thailand is close to GRAPES, both geographically and in cutoff rigidity. At PSNM the vertical cutoff, in geomagnetic quiet conditions, is ≈ 16.7 GV, whereas the directionally averaged cutoff is ≈ 17.3 GV. The counting rate at PSNM at the time of the GRAPES event is shown at the top of the left panel in Figure 2. The timing and structure of the pulse at PSNM is similar to that of the GRAPES pulse. Using our calculated yield functions for PSNM [6] we also find that the magnitude of the increase at PSNM is quite consistent with a cutoff reduction of approximately 0.6 GV. As Figure 2 shows, all neutron monitors show the onset of a large Forbush decrease near this time. Because of the Forbush decrease the identification of a pulse is somewhat subjective but it is clear that only a other few neutron monitors show a pulse as well defined as that at PSNM. For the monitors where the pulse

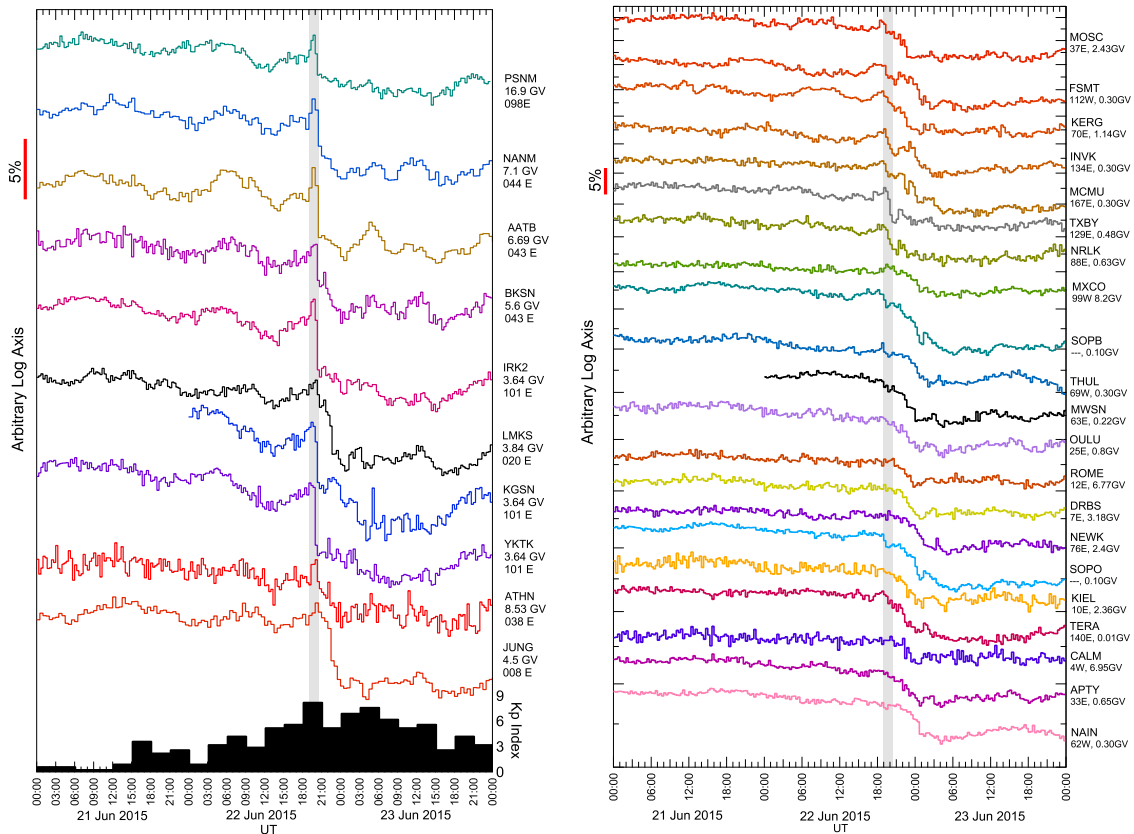


Figure 2: Left: Response of several neutron monitors having the largest increase at the same time as that observed by GRAPES on 2015 June 22. The Kp index of geomagnetic activity is shown in the lower panel. Right: Multiple neutron monitor observations ranked approximately by the intensity of the observed pulse. The approximate duration of the GRAPES pulse is indicated by the gray shading.

is clear (shown in the left panel of Figure 2) the Forbush decrease generally begins immediately and steeply following the pulse. For the other monitors the onset is not as sharp and is delayed by varying amounts. This behavior is characteristic of commonly observed Forbush decrease *precursors*. For a discussion and classification approach to such precursors, see[8].

We also find that a cutoff variation localized to the vicinity of the GRAPES detector is unlikely. In the commonly used Tsyganenko [11] model of the response of the magnetosphere to perturbation by interplanetary disturbances any variation in the geomagnetic cutoff is a fully global process. In this model the geomagnetic field cannot be described as a simple superposition of the interplanetary field and the internal (IGRF) field. Rather, the disturbance of the solar wind perturbs global current systems, and it is these current systems that affect the cutoff. Since these current systems are global, any change in the cutoff must also be global. The left panel of Figure 3 shows our calculation of cutoff changes predicted by the Tsyganenko model, performed by the method described in [5], as a function of Kp, the geomagnetic parameter that is the input to the Tsyganenko model.

Kp is an index computed from the range of fluctuations in the horizontal component of the magnetic field measured at ground level at a specifically defined array of locations. For an excellent discussion of why the single parameter Kp provides a good description of the state of the

magnetosphere see [10]. Note that it is an inescapable prediction of the Tsyganenko model that all locations on Earth have correlated changes in the geomagnetic cutoff, and indeed that cutoff changes are systematically larger for lower cutoffs.

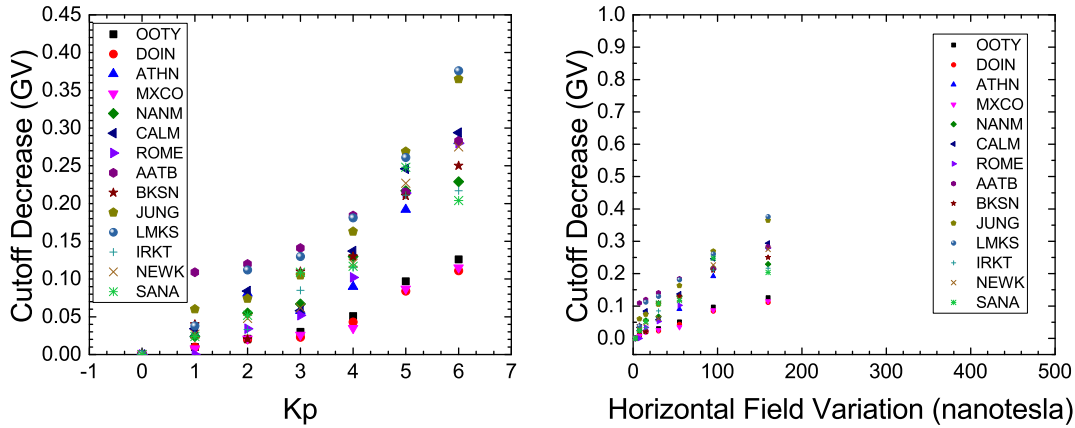


Figure 3: Cutoff reduction at various neutron monitors in the Tsyganenko model. Left: Plotted as a function of the single parameter in the model, integral values of the quasi logarithmic K_p . Right: Plotted as a function of the underlying linear magnetospheric parameter. The horizontal axis extends to 500 nT, which corresponds to $K_p=8$, the approximate value needed for extrapolation in the 2015 June 18 event. The cluster of points are the same as those in the left panel and thus indicate the values of K_p on this scale.

Unfortunately for the present analysis the Tsyganenko model relies on a fit to data to derive coefficients that describe all of the current systems that are assumed to follow K_p . Data above $K_p=6$ are too sparse to allow such a fit at these values. Consequently we cannot directly do the calculation for the $K_p=8$ level at the time of the GRAPES pulse. However the model employs physically meaningful parameters that describe specific magnetospheric current systems so there is no reason to assume that the model itself fails at that time.

The right panel of Figure 3 shows the calculated cutoff decrease plotted as a function of the range of variation of the horizontal surface field, which is the underlying linear parameter of the quasi-logarithmic K_p . The extent of the horizontal axis has been chosen to approximate the degree of extrapolation necessary to reach $K_p=8$. Linear extrapolation of the cutoff change at Ooty and Doi Inthanon (the lowest sequence of points on the figure) yields a somewhat smaller value than the 0.6 GV that would produce the effect seen at these stations, particularly considering that K_p changes from 6 to 8 at that time, not from 0 to 8. Exact agreement of the extrapolation with observation is not important to our argument. The key point is that the amount of extrapolation required is not so large that the model itself would fail in such a way as to modify the conclusion that cutoff changes are a global, not local, phenomenon.

3. Geographic Distribution

Figure 4 shows the distribution of neutron monitors at the time of the GRAPES event with symbols indicating our somewhat subjective classification of the appearance of a pulse at the monitor. Using the data in Figure 2 we have assigned (basically by eye) one of three categories to each

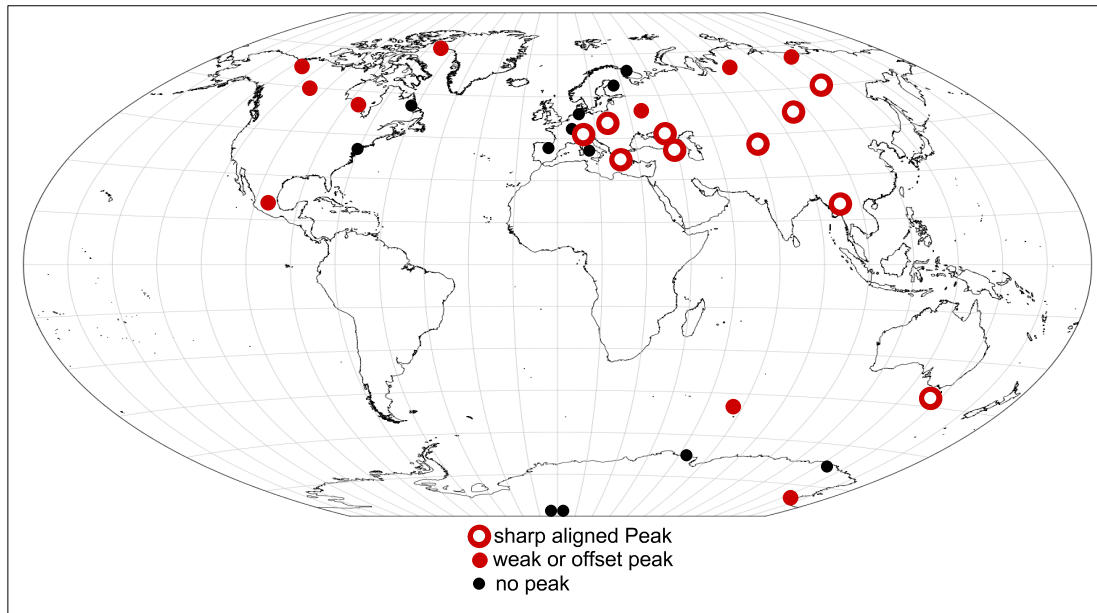


Figure 4: Geographic distribution of pulse visibility on 22 June 2015. Symbols indicate the location of neutron monitors classified as observing sharp aligned peaks, weak or offset peak, or no peak.

monitor: “sharp aligned peak”, “weak or offset peak”, or “no peak”. The geographic distribution of these categories is well organized by location, as expected for an anisotropy effect. According to Figure 3 changes in cutoff rigidity are not restricted to Asian longitudes. European stations have the strongest predicted cutoff changes yet most of them show no peak. This strongly argues against the interpretation of the GRAPES event in terms of a cutoff change.

4. Discussion and Conclusions

There is a general similarity in the morphology of the 2015 June 22 event observed by GRAPES and the 2017 January 18 event observed by IceTop. Both have a small, well defined but geographically localized increase in counting rate at the time of a magnetospheric disturbance. At the South Pole a lowering of the cutoff is impossible, so the only explanation for the 2017 January 18 event is anisotropy in the cosmic ray flux.

For the GRAPES peak on 2015 June 22 a cutoff change is possible, and the required magnitude of the cutoff change is consistent with an extrapolation of the Tsyganenko model. However the peak is not global as would be predicted by that model. The peak is also visible at several polar locations where the cutoff is so low that a change could not produce a visible pulse. Thus we favor anisotropy, rather than cutoff change as the preferred explanation. This anisotropy could either be temporary or could be a feature that is long lasting but only briefly observed because the asymptotic directions of the detector are changed by the geomagnetic disturbance. We also note that K_p is only defined in three hour intervals, and is clearly elevated over an interval more extensive than the GRAPES pulse. A more detailed look at the event, using a more fine-grained magnetospheric parameter, is

clearly required to isolate changes in the cutoff predicted by conventional models from those that might lie outside these models.

5. Acknowledgements

We acknowledge the NMDB database, founded under the European Union's FP7 programme (contract no. 213007) for providing neutron monitor data, and acknowledge individual monitors following the information given on the respective station information sub-page under www.nmdb.eu. Supported in part by US National Science Foundation awards PLR-1245939 and PLR-1341562 and grant RTA5980003 from the Thailand Research Fund.

References

- [1] Evenson, Paul, John Bieber, John Clem and Roger Pyle, South Pole neutron monitor lives again, *International Cosmic Ray Conference 32*, Beijing, (2011).
- [2] Hatton, C. J., The Neutron Monitor, *Progress in Elementary Particle and Cosmic Ray Physics X* (1971), American Elsevier Publishing Company, New York.
- [3] **IceCube** Collaboration, M. G. Aartsen et al., The IceCube Neutrino Observatory: Instrumentation and Online Systems, *JINST* **12** (2017) P03012.
- [4] **IceCube-Gen2** Collaboration, GeV solar energetic particle observation and search by IceTop from 2011 to 2016, *POS (ICRC2017) 132* (these proceedings).
- [5] Lin, Zhongmin, John W. Bieber, and Paul Evenson, Electron trajectories in a model magnetosphere: simulation and observation under active conditions, *Journal Of Geophysical Research* **100** (1995) 23,543 - 23,549.
- [6] Mangeard, P.-S., D. Ruffolo, A. Sáiz, S. Madlee, and T. Nutaro, Monte Carlo simulation of the neutron monitor yield function, *J. Geophys. Res. Space Physics* **121** (2016) doi:10.1002/2016JA022638.
- [7] Mohanty, P.K., K.P. Arunbabu, T. Aziz *et. al.*, Transient weakening of earth's magnetic shield probed by a cosmic ray burst, *PRL* **117** (2016) 171101.
- [8] Papailiou, M., H. Mavromichalaki, A. Belov, E. Eroshenko and V. Yanke, Precursor effects in different cases of forrush decreases, *Solar Phys.* **276** (2012) 337-350 DOI 10.1007/s11207-011-9888-1.
- [9] Stoker, P.H., Spectra of solar proton ground level events using neutron monitor and neutron moderated detector recordings, *International Cosmic Ray Conference 19*, La Jolla **4** (1985) 114-117.
- [10] Thomsen, M.F., Why Kp is such a good measure of magnetospheric convection, *Space Weather* **2** (2004) S11004, doi:10.1029/2004SW000089.
- [11] Tsyganenko, N.A., Global quantitative models of the geomagnetic field in the cislunar magnetosphere for different disturbance levels, *Planet. Space Sci.* **35** (1987) 1347-1358.

Performance of IceTop as a veto for IceCube

The IceCube Collaboration[†]

[†] http://icecube.wisc.edu/collaboration/authors/icrc17_icecube

E-mail: delia.tosi@icecube.wisc.edu

The IceCube Neutrino Observatory features a kilometer-cubed deep detector and a surface component, IceTop. IceTop consists of 162 ice-filled tanks equipped with optical sensors capable of detecting charged particles produced in air showers. While IceTop is well known for its cosmic-ray spectrum and mass composition measurements, it can also be used as a veto for IceCube. This role is becoming more important in the design of a larger surface array. High-energy neutrinos are absorbed by the Earth, therefore detecting neutrinos from the southern hemisphere is a priority. An efficient veto, however, requires suppressing the large background consisting of penetrating atmospheric muons and neutrinos. A surface array like IceTop can reduce the background by identifying particles which are generated in the same air shower as the muons in the deep detector. The capabilities and limitations of IceTop as a veto for cosmic rays will be presented.

Corresponding authors: Delia Tosi¹, Hershail Pandya^{*2}

¹*Dept. of Physics and Wisconsin IceCube Particle Astrophysics Center, University of Wisconsin, Madison, WI 53706, USA*

²*Dept. of Physics and Astronomy, University of Delaware, Newark, DE 19711, USA*

*35th International Cosmic Ray Conference — ICRC2017
10–20 July, 2017
Bexco, Busan, Korea*

*Speaker.

1. Introduction

The IceCube Neutrino Observatory is a particle detector located at the geographic South Pole [1]. The experiment features two components. The in-ice neutrino telescope (IceCube) consists of 86 strings each equipped with 60 digital optical modules (DOMs), installed at depths between 1450 m and 2450 m. The surface component (IceTop) includes 81 stations, each with two tanks 10 m apart located in proximity of the top of each in-ice string. Each tank contains frozen water and is equipped with two DOMs. The DOMs of both arrays feature photomultiplier tubes (PMT) able to detect, at single photon level, the Cherenkov radiation emitted by secondary charged particles. On the surface, these are charged leptons produced in hadronic or electromagnetic interactions in the atmosphere. In ice, these are either penetrating muons from showers, or particles produced by neutrino interactions in the Antarctic ice cap or in the bedrock.

The goal of the analysis presented in this paper is to study the veto capabilities of IceTop using air showers that are too low in energy to trigger the array, but which are coincident with muon events in IceCube. While the veto possibilities of IceTop were included in the original design of the array, a thorough study of its efficiency as a veto over a wide energy range is still underway.

Currently, the highest purity sample of astrophysical neutrinos is obtained isolating neutrino interactions starting in the instrumented volume of IceCube. In this sample, muon tracks are particularly important given their superior angular reconstruction, necessary for real time alerts and multi-messenger searches [2]. The immense majority of down-going muons entering IceCube are penetrating atmospheric muons or atmospheric neutrino-induced muons, and they constitute the main background in the search for astrophysical neutrinos. However, above a few hundred TeV muon energy, a muon track starting in the detector has a higher chance to be produced by the charged-current interaction of an astrophysical muon neutrino than by an atmospheric interaction, due to the harder spectral index of astrophysical neutrinos. The high energy starting track analysis [3] is highly effective in selecting astrophysical neutrinos, but it relies on using the outer shell of the IceCube detector as a veto, greatly decreasing the effective volume. A surface detector capable of identifying cosmic ray showers producing such tracks can effectively increase the detector volume of IceCube up to the surface, and extend the field of view towards the center of the Galaxy [4].

2. Method

2.1 Data Selection

The method presented here uses selection cuts substantially identical to those in the analysis presented in [5]. An offline filter selects events which have more than 1000 photoelectrons (PE) deposited in IceCube: this has a rate between 1 Hz and 2 Hz. Of these events we keep those which also have an *homogenized charge* $Q_{\text{toth}} > 1000$ PE, defined as the total charge calculated after removing those DOMs which have detected more than 50% of the total charge deposited. This last cut removes the so called *balloon events*, i.e. events where one DOM reports a disproportionate charge due to a muon track passing very close. We also require that the event is reconstructed as down-going, and that the muon track length in the detector is $L > 800$ m. Finally, the muon track trajectory extrapolated to surface needs to intersect the IceTop footprint at a *impact point* located inside the detector and at a distance $S > 62.5$ m from the perimeter of IceTop (see Fig. 1).

These cuts remove all the tracks with reconstructed zenith angle $\theta > 32^\circ$ and reduce the number of events drastically to 1.8% of the event selection we start with. The numeric values for L and S have not been yet optimized for this analysis.

The vast majority of the in-ice triggers selected with the above method are associated with cosmic ray showers. At sufficiently high energy these have clear signatures in IceTop: multiple DOMs detect photoelectrons (*hits*) induced by shower particles, allowing for the reconstruction of its energy and direction. As our focus is to link muon tracks with showers which have not necessarily triggered IceTop, we do not require an IceTop trigger and we use only information about the muon track obtained from the in-ice detector.

The muon direction is determined by a likelihood-based algorithm which fits the first arrival times and charge on all the DOMs in the detector, assuming an analytical parametrization of the Cherenkov light intensity as a function of distance to the muon track [7].

This reconstructed direction is then used as seed for a second fitting algorithm, which fits for the time of the interaction using only the time of the first unscattered photon and the total charge in each DOM. The combination of these steps provides better agreement between true and reconstructed values in simulation.

A proxy for the muon energy, called MuEx, is determined by fitting the expected number of photons via an analytic template which scales with the energy of the muon [6]. This energy estimator accounts for energy losses outside the detector and it is therefore more accurate than a simple sum of the DOM charges. A calibration of the energy proxy to the muon or muon bundle energy requires a high statistics simulation, not necessary for the goal of this analysis, therefore the values of MuEx are given in the following in arbitrary units.

The MuEx and zenith distribution of events remaining after the selection is shown in Fig. 6a and Fig. 6b for 10% of the data collected in 2012. The rise in event numbers up to $\log_{10}(\text{MuEx}) \sim 4$ is a threshold effect due to the use of $Q_{\text{toth}} > 1000$ PE for the event selection.

2.2 Signal simulation

Event rates for astrophysical neutrinos are estimated using NEUTRINOGENERATOR, a Monte Carlo simulation program based on ANIS [8]. Neutrinos are generated and propagated through the Earth using CTEQ cross section tables [9], and are forced to interact before passing through the detector volume; the true interaction probability is assigned to each neutrino interaction as a weight. For this analysis a general purpose dataset of muon neutrinos with a spectrum proportional to E^{-1} over an angular range of $0^\circ \leq \theta \leq 180^\circ$ and energy range of $10^2 \text{ GeV} \leq E_\nu \leq 10^7 \text{ GeV}$ was used. The same data selection criteria as explained in section 2.1 was applied. To obtain the signal

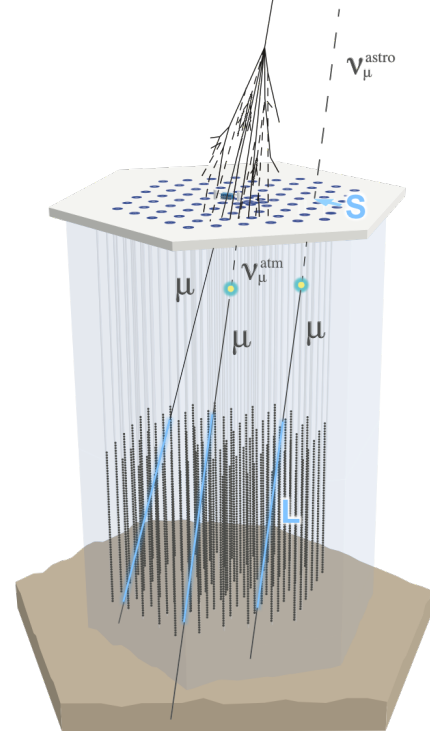


Figure 1: Illustration of the cuts used to select events for this analysis: $L > 800$ m and $S > 62.5$ m.

spectrum the surviving events were re-weighted to the best fit astrophysical neutrino spectrum of $\phi_{\nu+\bar{\nu}} = (0.90^{+0.30}_{-0.27}) \times 10^{-18} \text{GeV}^{-1} \text{cm}^{-2} \text{s}^{-1} \text{sr}^{-1} \cdot (E_\nu/100 \text{TeV})^\gamma$ with $\gamma = -2.13 \pm 0.13$ [10]. The calculated expected number of events for astrophysical neutrinos and cosmic rays is shown in Fig. 6. At $\log_{10} \text{MuEx} \sim 5$, a factor on the order of $\sim 10^5$ is required to reduce the background from cosmic rays to the level of astrophysical neutrinos.

The current simulation produced with NEUTRINOGENERATOR does not include IceTop hits, therefore with simulation it is not possible to develop cuts based on the temporal and spatial correlation of IceTop hits with in-ice muon tracks. To overcome this issue we process every recorded event of a certain time length in the final selection in the following way: we replace all the IceTop hits with a same duration snapshot of IceTop hits extracted from a fixed rate trigger recorded within hours from each recorded event. The fixed rate trigger is a 10 ms unbiased recording of the whole detector taken at a fixed rate (every 30 seconds). Given the long duration of the recording, fixed rate triggers contain a number of other naturally occurring triggers. For this analysis we do not use any fixed rate triggers which have also satisfied an IceTop trigger. The dataset obtained with this method resembles neutrino-like signals, and includes all the systematics of the detector, such as the temporal variation of IceTop DOMs hit rates (due to temperature and snow depth) and cross correlation of hits between DOMs in a single tank due to stray muons, and DOM inherent features like after-pulsing and pre-pulsing [11]. This sample is referred to in the following as the *randomized sample* or neutrino-like (ν -like) sample and is compared with the experimental cosmic ray data (cr-data) sample.

2.3 Data Processing

Given an event in IceCube, the muon track direction is assumed to represent the axis of the cosmic ray shower producing the muon. For each tank we calculate the perpendicular *lateral distance* from the shower axis and the expected arrival time of the shower at the tank, after extrapolating the muon track to the surface and using a data-derived model for the curvature of the shower front. If a tank did not record a hit or was not operational at the time of the event, we record its distance and we keep track of the tank status. If a tank has a hit, we record the *residual time* t_{res} , defined as the difference between the recorded and the expected time. In order to keep the normalization correct it is necessary to require at most one pulse per tank per event, so that the sum of tanks with or without hits and the tanks not operational at the event time is constant in all the events considered.

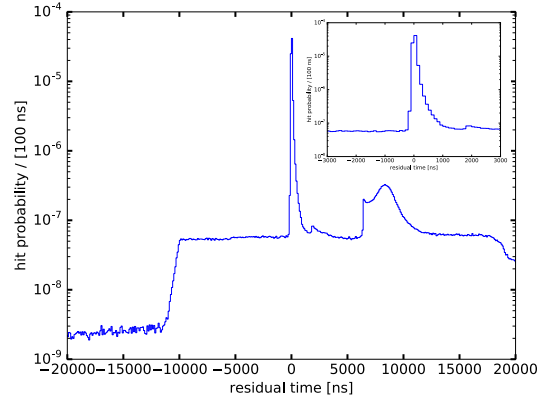


Figure 2: Template used to select one hit per tank per event, showing the distribution of all the hits residual times (see text) for all the events in the selection. The inset shows a zoomed-in version.

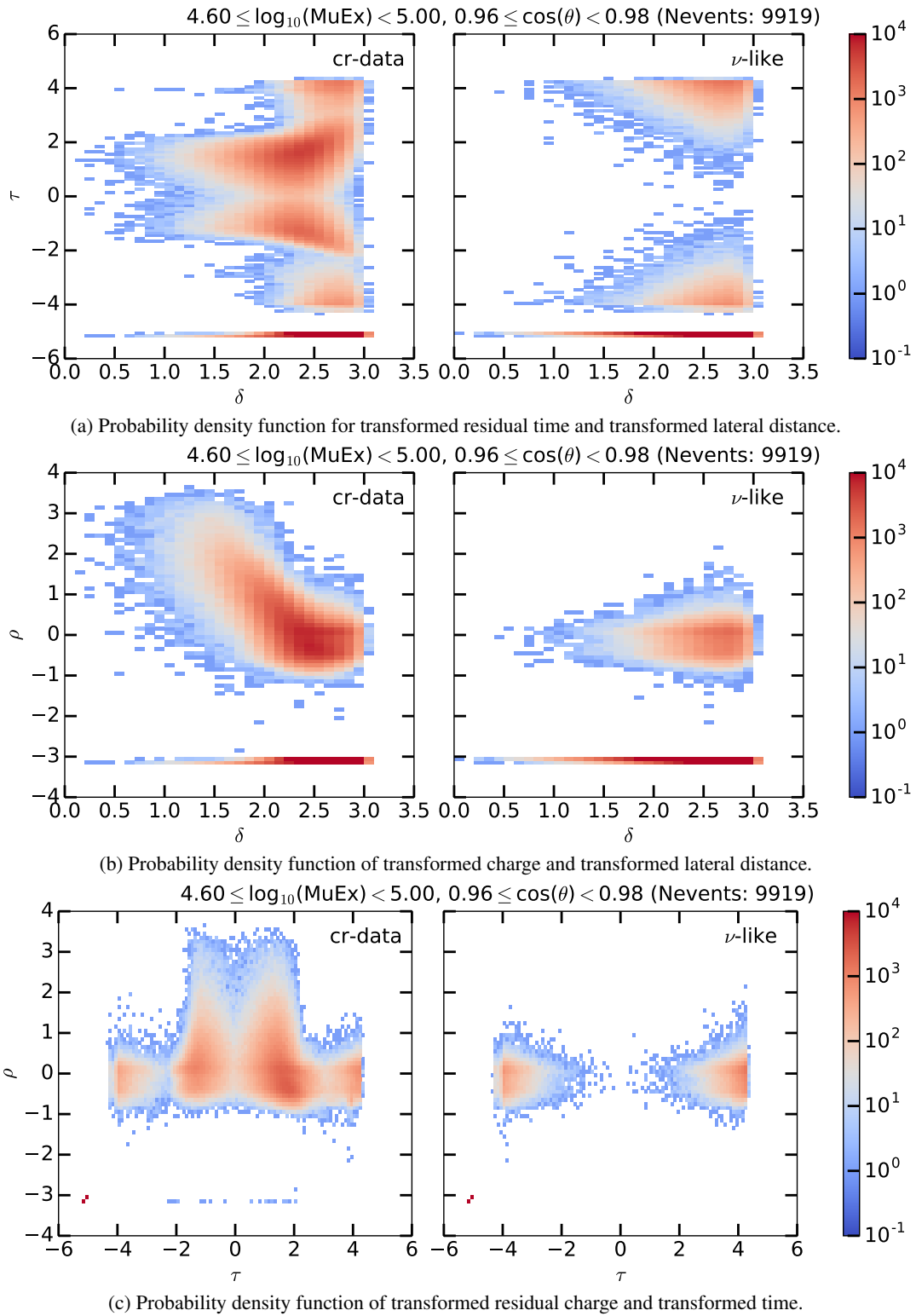


Figure 3: 2D-PDFs for one energy, zenith bin. The variables shown are residual time, lateral distance and charge detected by IceTop DOMs with the transformation of coordinates as explained in the text. The left column shows the experimental data, the right column shows the randomized sample. The bands at the bottom represent non-operational DOMs or DOMs which did not record a hit.

If the two DOMs in a tank have more than one hit, we remove all hits but the one which has the highest probability to be correlated with the cosmic ray shower. This probability is calculated from a one-dimensional probability density function derived from the residual times of all the hits. The data-derived template is shown in Fig. 2. The central spike corresponds to the shower front, while the bumps at later times are due to a combination of ADC's dead time and PMT after-pulses [1, 11].

For each hit surviving the selection, we also track the charge Q_i recorded by the DOM in tank i , which is expressed in units of *Vertical Equivalent Muon* (VEM) [12].

To increase the weight of hits near in time or space to the shower front, we use a logarithmic binning. Since residual times can be negative and have values between 0 and 1 ns, we apply a coordinate transformation and define $\tau = \text{sign}(t_{res}) \cdot \log_{10}(|t_{res}|+1)$. We use a similar coordinate transformation for the lateral distance (always positive by definition) since it can also have values ≤ 1 m. We call the new parameters *transformed residual time* τ and *transformed lateral distance* δ . As for the charge, we define the parameter *transformed charge* $\rho = \log_{10}(Q)$.

2.4 PDFs and LLH Ratio

Using the observables defined above $(\rho_i, \tau_i, \delta_i)$ we construct three two-dimensional PDFs as shown in Fig. 3 for one example energy and zenith bin for the experimental dataset (representing the cr-data sample) on the left and the randomized sample (representing the ν -like sample) on the right. From the comparison between each PDF for the two datasets, the cosmic rays signature is visible as a larger number of hits near the shower front and in the higher charge distribution (i.e. at small values of τ and δ and large values of ρ). The larger population of hits at large values of δ is due to geometry (a larger number of tanks is available at larger radius). The randomized sample shows the distribution of hits in the same variables for neutrino-like events. Sections of each PDF are shown in the corresponding linear variables in Fig. 4. For a given event, a log-likelihood (LLH) ratio is constructed using three sets of PDFs. For example, the LLH ratio (LLHR) using the τ_i vs.

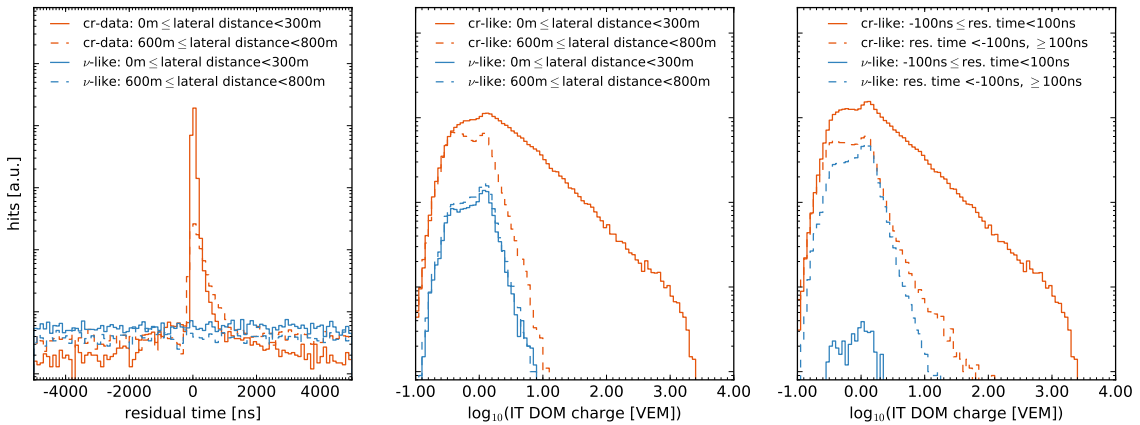


Figure 4: Each plot shows the equivalent of a slice for each two-dimensional PDF as shown in Fig. 3, for cr-data and ν -like samples and for two selected ranges of lateral distance or residual times, close or far from the shower front. The cr-data sample shows more hits and larger charge near the shower front than the ν -like sample.

δ_i PDF is constructed as follows:

$$\text{LLH Ratio} = \log_{10} \left(\frac{L(\{(\tau_i, \delta_i)\} | H_{CR})}{L(\{(\tau_i, \delta_i)\} | H_\nu)} \right) \quad (2.1)$$

where the individual log-likelihoods are defined as

$$L(\{(\tau_i, \delta_i)\} | H) = \prod_{i=1}^{N_{\text{Tanks}}} P(\tau_i, \delta_i | H) \quad (2.2)$$

Here $P(\tau_i, \delta_i | H)$ is the probability of having a tank with transformed residual time τ_i and transformed lateral distance δ_i in the PDF constructed using hypothesis H ($H = CR$ or ν). The LLHR distribution is shown for each template and for one example energy and zenith bin in Fig. 5.

Given each LLHR distribution we calculate the LLHR cut value that retains a predefined fraction (for example 100% and 90%) of the randomized sample events in the distribution. The three distributions are treated as independent, so the fraction of neutrinos retained as a result is 100% in the first case. In the second case, the fraction of neutrinos retained depends on energy and zenith bin; overall 80% neutrinos are retained. We then count how many cosmic rays pass such cuts as a function of zenith angle and muon energy proxy. We then rescale the number of passing events taking into account that the sample analyzed corresponds to $\sim 1/11$ of the livetime of the 2012 dataset. The effect of such cuts on the distribution of events at the final selection is shown as a function of the muon energy proxy (integrated over all the zenith angles) in Fig. 6a and as a function of the cosine of zenith angle (integrated over all the energies) in Fig. 6b. Where no events pass the LLHR cuts, we show the 68% confidence level upper limit.

3. Results

The preliminary veto efficiency, calculated with the log-likelihood method presented here, is shown vs energy and vs zenith in Fig. 7a-7b. With a 80% (100%) retaining fraction of astrophysical neutrinos, in the energy bin between $4.6 \leq \log_{10}(\text{MuEx}) < 4.8$ ($4.8 \leq \log_{10}(\text{MuEx}) < 5.0$), none of the 7622 events in the sample passes the cuts. At this energy and above we show therefore the 68% upper limit. In the energy bin between $4.4 \leq \log_{10}(\text{MuEx}) < 4.6$ ($4.6 \leq \log_{10}(\text{MuEx}) < 4.8$), 11 (6) events out of 48197(26803) pass the cuts, with the method achieving a background passing rate (equivalent to $1.0 - \text{veto rejection efficiency}$) of 2.3×10^{-4} (2.2×10^{-4}). No events are found in the selection with $\log_{10}(\text{MuEx}) \geq 6.2$.

A further optimization of the cuts is possible, and other methods to combine the three different log-likelihood discriminators are being investigated. More statistics will be added in order to improve the veto efficiency at high energy, where the current estimate is statistically limited. The method will be used to explore requirements for a future extended veto.

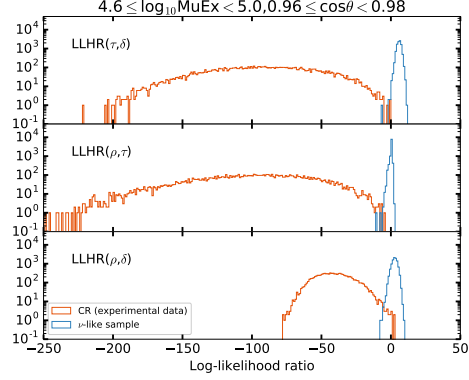


Figure 5: Log-likelihood ratio for one energy and zenith bin, for the three two dimensional PDFs shown in Fig. 3.

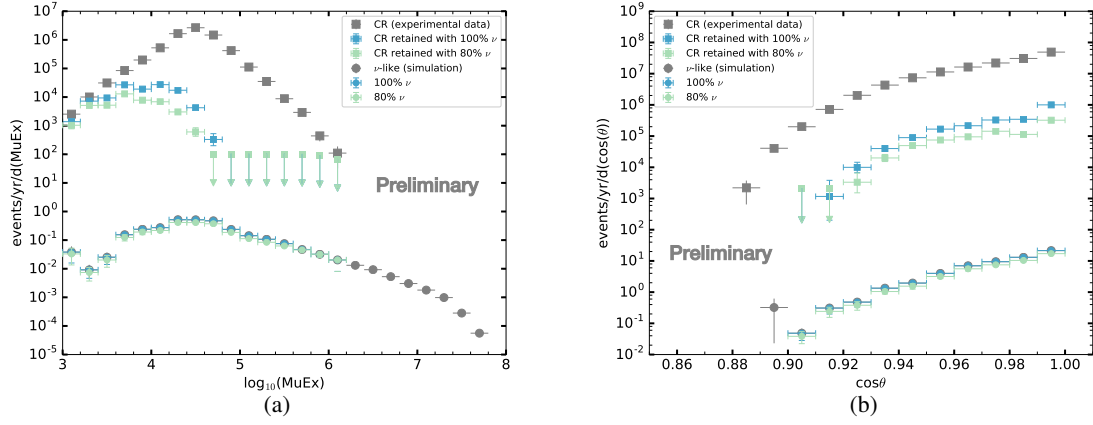


Figure 6: Event rates for background (data) and signal (calculated with simulation), versus in-ice muon energy proxy (a) and versus cosine of zenith angle (b) at the final selection level and after applying a cut which retains 100% and 80% neutrinos. The rise in event numbers up to $\log_{10}(\text{MuEx}) \sim 4$ is due to the selection of events being based on a different energy proxy (see section 2.1). Arrows indicate upper limits.

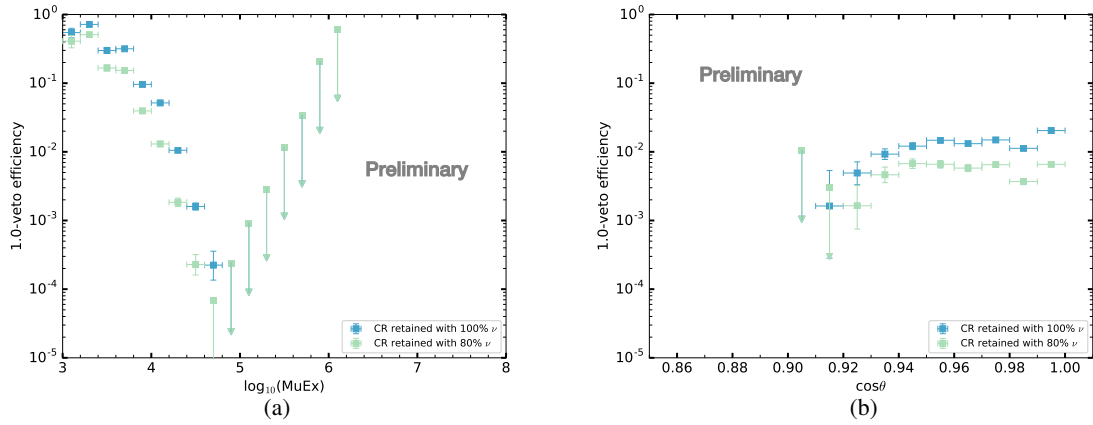


Figure 7: Veto efficiency calculated from analyzed sample, versus in-ice muon energy proxy (a) and versus cosine of zenith angle (b). The arrows denote upper limits.

References

- [1] IceCube Coll., M. G. Aartsen et al., *J. Inst.* **12** P03012 (2017).
- [2] IceCube Collaboration, *PoS (ICRC2015)* 022 (2015).
- [3] IceCube Coll., *PoS (ICRC2017)* 981 (these proceedings).
- [4] IceCube Collaboration, *PoS (ICRC2015)* 1156 (2015).
- [5] IceCube Coll., *PoS (ICRC2015)* 1086 (2015).
- [6] IceCube Coll., M. G. Aartsen et al., *J. Inst.* **9** P03009 (2014).
- [7] AMANDA Coll., J. Ahrens et al., *Nucl. Instrum. Meth.* **A524** 169-194 (2004).
- [8] A. Gazizov and M. P. Kowalski, *Comput. Phys. Commun.* **172** 203-213 (2005).
- [9] R. Gandhi, C. Quigg, M. H. Reno, I. Sarcevic *Phys. Rev.* **D58** 093009 (1998).
- [10] IceCube Coll., M. G. Aartsen et al., *Astrophys. J.* **833** 3 (2016).
- [11] IceCube Coll., R. Abbasi et al., *Nucl. Instrum. Meth.* **A618** 139-152 (2010).
- [12] IceCube Coll., R. Abbasi et al., *Nucl. Instrum. Meth.* **A700** 188 (2013).

Solar atmospheric neutrino search with IceCube

The IceCube Collaboration[†]

[†] http://icecube.wisc.edu/collaboration/authors/icrc17_icecube

E-mail: seongjin.in@gmail.com

Cosmic rays interacting in the solar atmosphere can produce high energy neutrinos, which could be detected with IceCube. Neutrinos are produced through the decay of pions and kaons, similar to cosmic ray air showers in the Earth's atmosphere. Due to the lower solar atmospheric density, the neutrino spectrum from the Sun is expected to be harder as mesons tend to decay before they can interact or encounter any significant energy loss. The solar disk neutrino flux could be visible over the atmospheric backgrounds at energies above a few hundred GeV. We present IceCube's sensitivity as determined by a dedicated analysis for solar atmospheric neutrinos.

Corresponding authors: Seongjin In^{1*} and Carsten Rott¹

¹Department of Physics, Sungkyunkwan University, Seobu 16419, Suwon, South Korea

*35th International Cosmic Ray Conference — ICRC2017
10–20 July, 2017
Bexco, Busan, Korea*

*Speaker.

1. Introduction

Interactions of cosmic rays with the nuclei of the solar atmosphere (photosphere and chromosphere) produce energetic photons. This phenomenon has been described in detail by Seckel et. al. in 1991 [1] and has been recently observed by Fermi-LAT [2]. However, the observed solar disk emission of gamma rays exceeds the theoretical model estimates by an order of magnitude. The gamma-ray flux anti-correlates with the solar activity and there is evidence that the emission spectrum extends beyond 100 GeV [3].

Cosmic ray interactions in the solar atmosphere are also expected to produce energetic neutrinos (figure 1), which could be detected by terrestrial neutrino telescopes [4]. Solar atmospheric neutrino and gamma-ray observations are important to understand solar magnetic fields and cosmic ray propagation in the inner solar system. Solar atmospheric neutrinos provide a natural background to solar dark matter searches and limit their sensitivity as recently pointed out [5, 6, 7].

The IceCube observatory, located at the South Pole is the largest neutrino telescope in the world [8]. Construction of the full detector, consisting of 86 strings (IC86), was completed in 2010. The detector is operating very stable and has opened up a new window to the Universe through the observation of high-energy astrophysical neutrinos. Muon neutrinos above a few hundred GeV can be reconstructed with sub degree precision. This excellent angular sensitivity gives IceCube also discovery potential for solar atmospheric neutrinos. Previous IceCube analyses have searched for neutrinos in direction of the Sun in an effort to find self-annihilating dark matter [9, 10]. As the Sun is opaque to neutrinos above a few hundred GeV generated in its center, these analyses were not optimized to look for high energy neutrinos.

In this work, we present the first IceCube analysis that searches for solar atmospheric neutrinos. We first identify an event sample that is well suited for this analysis, the selection is described in section 2. In section 3, we predict the signal and backgrounds based on our simulations. In section 4, we optimize selection criteria and compute sensitivities, before concluding in section 5.

2. Identification of optimal event sample

For our analysis we reuse an existing IceCube event sample. It has the benefit that we can use a sample, which is already well understood and makes our analysis more robust. For the selection of the optimal event sample we do a comparison of signal and background predictions based on effective areas of the corresponding samples.

2.1 Signal and background flux

High energy cosmic ray particles entering the solar atmosphere interact with atmospheric nuclei to produce hadronic cascades. When propagating through the atmosphere the cascade products

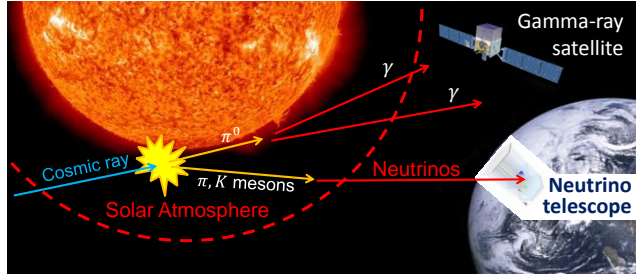


Figure 1: Schematic of solar atmospheric neutrino emission from cosmic ray interactions in the solar atmosphere.

decay or interact to produce secondary cascades. Neutrinos can be produced from decays of pions and kaons in the cascades. The processes are similar to the well understood cosmic ray air showers in the Earth atmosphere. However, due to the lower matter density of the solar atmosphere hadrons are more likely to decay than to interact again. This results in a harder neutrino energy spectrum compared to atmospheric neutrinos from the Earth atmosphere.

A theoretical prediction for solar atmospheric neutrinos was given by Ingelman and Thunman (IT) [4], which we adopt as our benchmark signal (see figure 4 of [4]). As background we take the atmospheric neutrino spectrum as determined by IceCube [11]. Since IT only reports the total neutrino flux we apply a factor of 1/3 to correct for neutrino oscillations resulting in equal predictions for ν_e and ν_μ . In figure 2 (left) we report signal and background neutrino fluxes as expected from an opening angle around the Sun motivated by the kinematic angle between neutrino and leading lepton and IceCube's angular uncertainty. We use the following energy and flavor dependent angular uncertainties:

$$A(E, \nu_i) = \begin{cases} \sqrt{100 + 900/E[\text{GeV}]}^\circ & \nu_e, \text{ for all energies} \\ 30^\circ / \sqrt{E/\text{GeV}} & \nu_\mu, E < 900\text{GeV} \\ 1^\circ & \nu_\mu, E > 900\text{GeV} \end{cases} \quad (2.1)$$

Based on the comparison in the figure 2 (left) we expect that the muon neutrino sample will have better sensitivity for our analysis.

2.2 Event expectation in IceCube

We estimated the expected number of events with previous IceCube analyses; We compare the effective area of the 3 year solar WIMP analysis [10] and the 7 year likelihood point source analysis [12] in figure 2 (right). For our comparison we only consider up-going events in order to use the Earth as a veto for atmospheric muon backgrounds. The solar WIMP analysis is optimized for low energy neutrinos from the direction of the Sun. Its effective area was not computed for

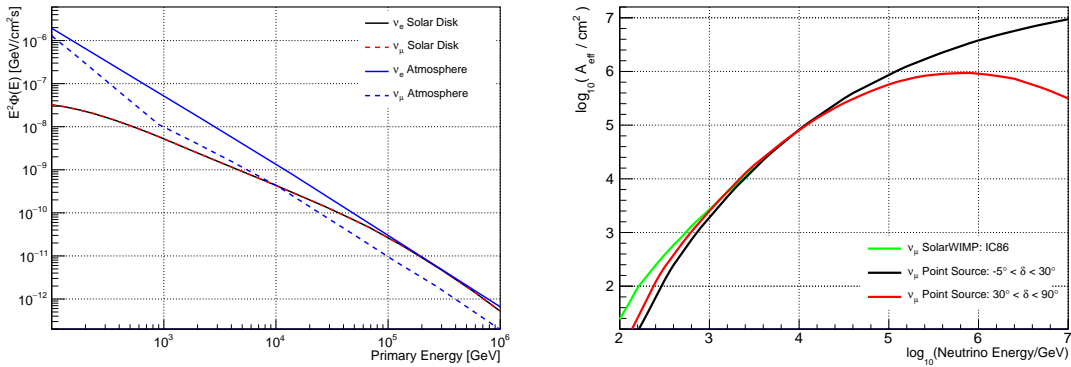


Figure 2: Left: The energy spectrum of atmospheric neutrinos (background) and solar atmospheric neutrinos (signal). An energy dependent search cone with the size of the kinematic angle between lepton and neutrino is applied for backgrounds (blue dotted- ν_μ and blue solid- ν_e). The spectra of signal (red- ν_μ and black- ν_e) is identical after the neutrino oscillation applied and apply a 68% of reconstruction efficiency. Right: Effective areas of solar WIMP analysis line (green) up to $10^{3.5}$ GeV, point source analysis for each declination angle ranges (red and black).

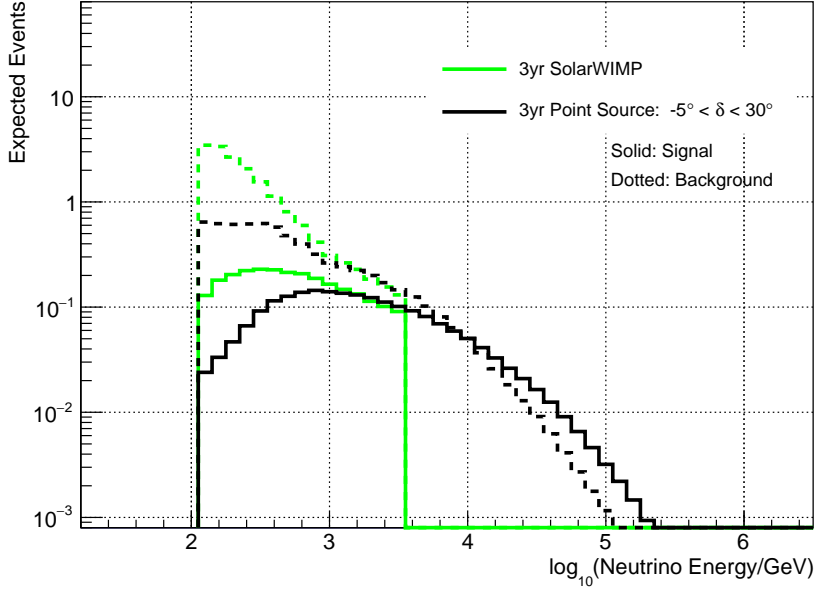


Figure 3: Expected solar atmospheric (solid lines) and atmospheric background (dotted lines) neutrino events as a function of primary neutrino energy. As the solar WIMP analysis focused on low energies where the signal flux is harder, more signal events could be shown, but also more background. With point source sample, the signal and the background are competitive on high energies.

energies above a few TeV and is expected to fall off around 5 TeV due to a selection cut on the number of hit optical sensor modules. The point source analysis is a full sky analysis that extends to high energies. We use the effective area for the $-5^\circ < \delta < 30^\circ$ declination cut.

We estimate the number of signal and background events as function of true muon neutrino energy using the effective areas and the neutrino flux from figure 2. We assumed that the signal is uniformly distributed within the radius of the Sun (0.25°) and 68% of the signal can be reconstructed in the direction of the Sun within the cone opening angle.

Figure 3 shows the energy distribution of the expected events with 3 years of IceCube data. The actual livetimes of the samples are 528.3 and 630 days, for the solar WIMPs (green) and point source sample (black), respectively. The solar WIMP analysis yields a higher signal acceptance than the point source analysis however most events are expected in the low energy region $\sim O(100\text{GeV})$. Overall the signal to background ratio for the solar WIMP analysis ($S/B = 0.147$) is less favorable compared to the point source analysis ($S/B = 0.309$). We decide to use the point source sample for our analysis as it is expected to yield the best sensitivity.

3. Monte Carlo Simulation

According to the estimate in section 2 we now use the point source Monte Carlo (MC) simulation samples for our analysis. For the signal simulation, we re-weighted the simulation to the theoretical model of the signal in [4]. In this section, we describe the signal and background simulation results.

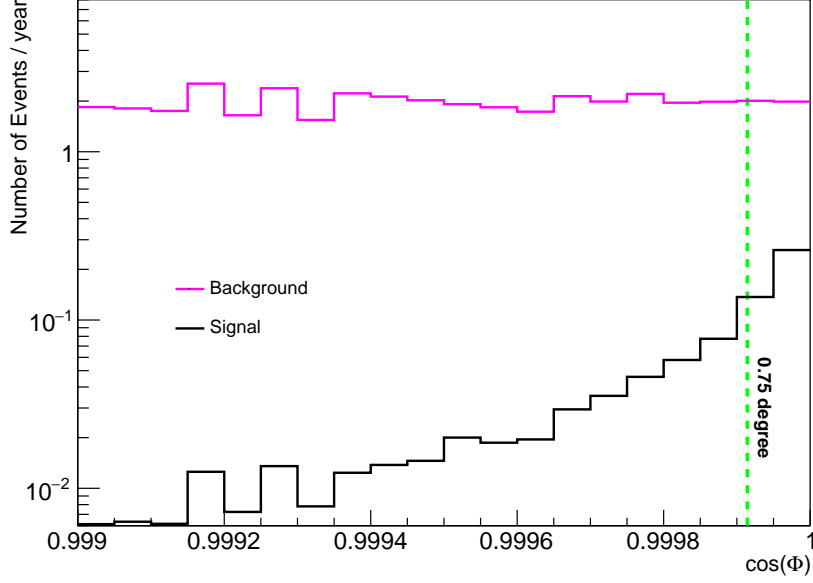


Figure 4: The expected number of events as a function of the reconstructed angular distance from the Sun. The Sun is located at $\cos(\Phi) = 1$. The magenta line is the simulated background and black is the re-weighted signal.

3.1 Atmospheric Background Neutrinos

We simulated ν_μ in the IC86 configuration from 100 GeV to 1 EeV for the whole sky. Our theoretical model for atmospheric neutrinos is the Honda 2006 flux from [13]. As mentioned in section 2, the Earth can be used as a μ veto and we only used the up-going samples. In our simulation we predict 66319.4 ± 0.6 atmospheric ν_μ up-going events per year.

3.2 Solar Atmospheric Neutrinos

The IT spectrum is our benchmark signal and we used the parameterization in [4]. Table 2 and eq 3.1 are taken from table 2 and eq.15 in [4] for the ν_μ flux.

$$\Phi(E) = \begin{cases} N_0 E^{-\gamma-1} / (1 + AE) & E < E_0 \\ N'_0 E^{-\gamma'-1} / (1 + AE) & E > E_0 \end{cases} \quad (3.1)$$

For the signal samples, the simulations are re-weighted into eq 3.1. Since the declination of the Sun is from 23.44° to -23.44° at South Pole, the zenith angle (Θ) of the Sun is fixed according to eq 3.2.

$$\Theta = (90^\circ - 23.44^\circ * \cos(360/365 * day)) \quad (3.2)$$

The azimuth angle is randomly scrambled. Only events which are within the solar angular extension of 0.25° are selected. We expect 2.85 ± 0.01 signal events in 3 years of data. Note that we only consider upgoing events, which limits our selection to 1.5 years, when the Sun is below

	N_0	γ	A	E_0	γ'	N_0'
$\nu_\mu + \bar{\nu}_\mu$	1.3×10^{-5}	1.98	8.5×10^{-6}	3.0×10^6	2.38	5.1×10^{-3}
$\nu_e + \bar{\nu}_e$	7.4×10^{-6}	2.03	8.5×10^{-6}	1.2×10^6	2.33	5.0×10^{-4}

Table 1: Fitting Parameters for the Ingelman & Thunman spectrum [4] and used in this analysis.

the horizon. Figure 4 shows our background and signal distribution along the reconstructed angular distance with respect to the position of the Sun. As the signal events are spread within 0.25° , the signal events are concentrated in the last bin (see figure 4).

4. Sensitivity Estimate

4.1 Selection Cut Optimization

We conduct an optimization of the opening angle and energy cuts to improve our sensitivity. As a first effort, we calculated S/\sqrt{B} as a function of the cone opening angle and the reconstructed energy cut, in figure 5. The highest (black star) S/\sqrt{B} is found with an opening angle cut of 1.5° and an energy cut of 430.0 GeV. The z-axis of figure 5 is flat below a few hundreds of GeV, because the reconstructed energy dominantly has spread at TeV region. For the best sensitivity, we apply these cuts to our samples. Note that we did not simulate neutrino events with energies below 100 GeV. Sometimes these events could reconstruct to higher energies and skew our optimization. We

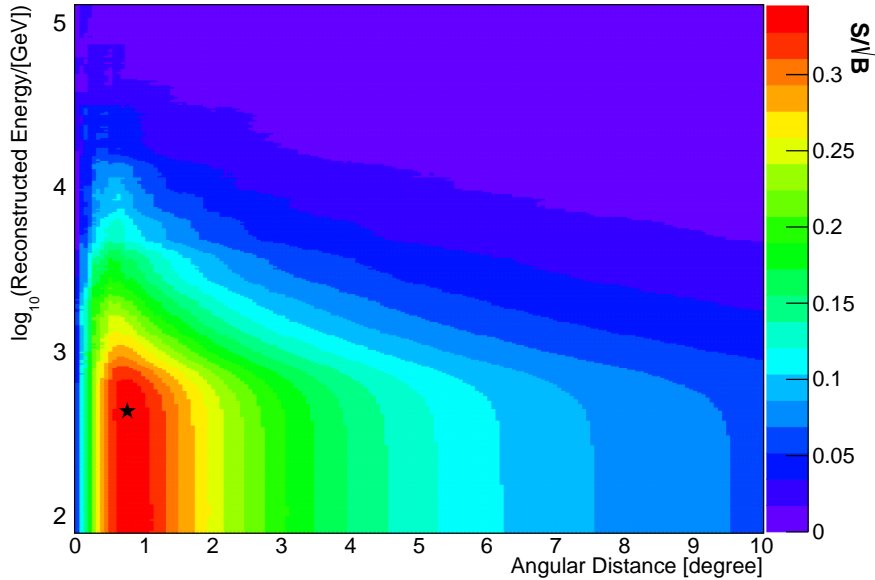


Figure 5: Signal(S) and background(B) ratio plot for the corresponding angular distance from the Sun and energy cut. The color bar represents S/\sqrt{B} . The black star indicates the optimal selection cut, which yields the highest S/\sqrt{B} of 0.34.

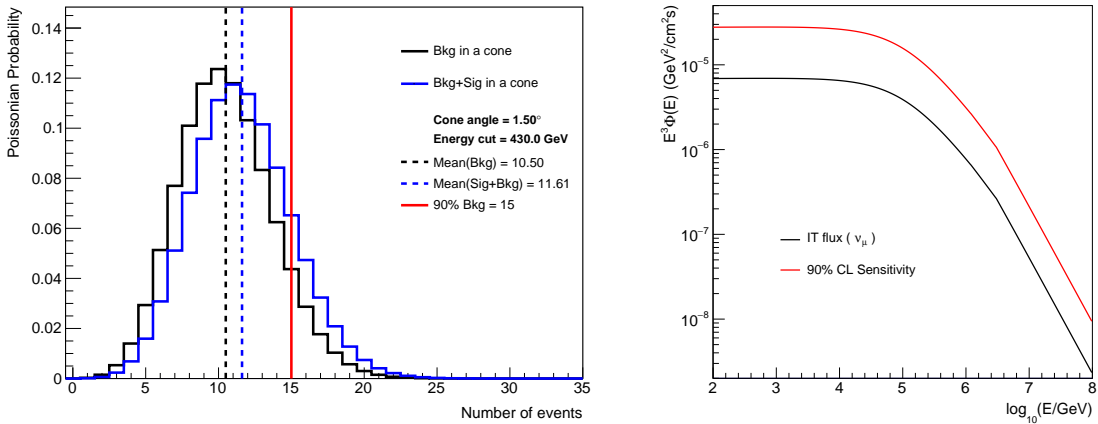


Figure 6: Left: Poisson distribution for the expected number of background events (black), signal+background (blue) within a 1.5° opening angle cone. The vertical black dotted and blue dotted lines are the median of each distribution. The vertical red line denotes the 90% lower quantile of the background only distribution. Right: Red line is the 90% confidence level sensitivity. The black line is the IT spectrum scaled down by a factor of 3 by the effect of neutrino oscillation.

estimate that the contribution of these events is less than 4% of our event sample above the optimal selection cut.

4.2 Sensitivity

The estimated number of background events can be utilized to calculate a sensitivity to the solar atmospheric neutrino flux. We calculate a sensitivity at 90% confidence level using a Poisson distribution. According to the cuts in section 4, simulated events are selected with reconstructed energies above 430 GeV and reconstructed direction within 1.5° from the Sun. With these cuts, 10.5 ± 0.18 background events (n_{bkg}) and 1.12 ± 0.19 signal events (n_{sig}) are expected in 3 years from the direction of the Sun.

The left hand side of figure 6 shows a probability density function for pure background, background and the expected signal ($n_{bkg+sig} = 12.11$) and the medians of these distributions. The lower 90% quantile of the pure background distribution is found at $n_{90} = 15$. The right-hand side of figure 6 is the statistical sensitivity of IceCube from the point source up-going simulation sample. The black line represents the IT spectrum taking into account neutrino oscillations. Given that the 90% confidence level sensitivity exceeds the expected signal no observation is expected with the current analysis. However with an improved event selection the signal might be in reach. For simplicity we used a cut and count analysis, for the actual analysis we are developing a log-likelihood method similar to the approach used in the solar dark matter analysis [10].

5. Summary

We looked at the sensitivity of IceCube to solar atmospheric neutrinos. We have estimated the expected number of signal and background events from the direction of the Sun with the effective areas of previous IceCube analyses in section 2. We determined that the point source analysis

is better suited compared to the solar WIMP analysis. We calculated the signal and background expectations using the point source analysis [12] MC simulation sample.

With up-going MC simulation samples of the point source analysis, we estimated the number of signal and background events using the optimized cuts. For the optimization of the cuts, we used S/\sqrt{B} to determine the cone cuts and the energy cuts. The maximum value of S/\sqrt{B} is 0.34 at a 1.5° opening angle cut and a 430 GeV energy cut. This yields $n_{sig} = 1.12$ and $n_{bkg} = 10.5$ events in 3 years. The IceCube sensitivity for the solar atmospheric neutrino flux is obtained (figure 6). The sensitivity is expected to further improve in the future by using a log-likelihood analysis method, expanding the analysis to include additional neutrino flavors, and by utilizing down-going events. Further selection cut optimization could also help to distinguish the signal better from backgrounds.

It should be noted that there is a considerable uncertainty on the neutrino flux prediction from the Sun [4, 7, 5], making the outcome of this search less predictable. The analysis carries importance to help understand solar magnetic fields and cosmic ray propagation in the inner solar system. An observation of the solar atmospheric neutrino could be the first high energy astrophysical point source. Solar atmospheric neutrinos also pose a background for solar Dark Matter searches [7, 5, 6] and this analysis can help quantify it.

References

- [1] Seckel. D, Stanev T. and Gaisser. T. K., *Astrophys J.* **382** (1991) 652-666.
- [2] **Fermi-LAT** Collaboration, A.A. Abdo et al., *Astrophys J.* **734** (2011) 116.
- [3] Kenny C.Y. Ng, John F. Beacom, Annika H.G. Peter and C. Rott, *Phys. Rev.* **D94** (2016) 023004.
- [4] G. Ingelman and M. Thunman, *Phys. Rev.* **D54** (1996) 4385-4392.
- [5] C.A. Argüelles, G. de Wasseige, A. Fedynitch and B.J.P. Jones, [astro-ph/1703.07798].
- [6] Kenny C. Y. Ng, John F. Beacom, Annika H. G. Peter and C. Rott, [astro-ph/1703.10280].
- [7] J.Edsjö, J.Elevant, R.Enberg and C.Niblaeus, [astro-ph/1704.02892v1].
- [8] **IceCube** Collaboration, M.G. Aartsen et al., *JINST* **12** (2017), P03012.
- [9] **IceCube** Collaboration, M.G. Aartsen et al., *Phys. Rev. Lett.* **110** (2013) 131302.
- [10] **IceCube** Collaboration, M.G. Aartsen et al., *Eur. Phys. J.* **C77** (2017) 146.
- [11] **IceCube** Collaboration, M.G. Aartsen et al., *Phys. Rev.* **D91** (2015) 122004.
- [12] **IceCube** Collaboration, M.G. Aartsen et al., *Astrophys J.* **835** (2017) 151.
- [13] M. Honda, T.Kajita, K.Kasahara, S.Midorikawa and T. Sanuki, *Phys. Rev.* **D75** (2007) 043006.

High-Energy Atmospheric Muons in IceCube and IceTop

The IceCube Collaboration[†]

[†] http://icecube.wisc.edu/collaboration/authors/icrc17_icecube

E-mail: frederik.tenholt@icecube.wisc.edu

High-energy atmospheric muons can yield information about the prompt contribution to atmospheric lepton fluxes. Relevant to studying the flux of astrophysical neutrinos, this also complements results from collider experiments in the forward region. A machine-learning based selection has been developed, identifying high-energy ($E_\mu \gtrsim 1$ TeV) leading muons which dominate the energy losses detected in IceCube. The sample is then analyzed in two ways. First, the correlation between the muon energy in ice and the muon energy at its production in the atmosphere, which can be derived from simulations based on Monte-Carlo methods, is used for estimating the differential energy spectrum of atmospheric muons in the energy range between 6 and 400 TeV. The best-fit power law index describing the atmospheric muon flux is found to be consistent with the result of a previous analysis. Second, dedicated simulations are used to show a proof-of-concept for reconstructing the effective Feynman- x of atmospheric muons by combining information from IceCube and IceTop. A robust correlation between true and reconstructed effective Feynman- x is found, enabling future studies of this quantity with the IceCube Neutrino Observatory.

Corresponding authors: Frederik Tenholt^{*1}

¹ *Fakultät für Physik & Astronomie, Ruhr-Universität Bochum, D-44780 Bochum, Germany*

*35th International Cosmic Ray Conference — ICRC2017
10–20 July, 2017
Bexco, Busan, Korea*

*Speaker.

1. Introduction

IceCube is a 1 km³ neutrino detector installed in the ice at the geographic South Pole [1] between depths of 1450 m and 2450 m, completed in 2010. Reconstruction of the direction, energy and flavor of the neutrinos relies on the optical detection of Cherenkov radiation emitted by charged particles produced in the interactions of neutrinos in the surrounding ice or the nearby bedrock. In 2013, the IceCube Collaboration found evidence for an astrophysical flux of neutrinos [2]. Since atmospheric leptons are the main background to such a flux, a detailed understanding of them is essential. One important aspect is the contribution of prompt decays from short-lived hadrons, that is, from charmed mesons and unflavored vector mesons [3]. Because of their short lifetime, these intermediate air shower particles usually decay before interacting, yielding harder lepton spectra than those induced by light mesons like π^\pm and K^\pm [4]. With a rate of about 2100 s⁻¹, muons originating from extended air showers are the most frequent particles triggering IceCube and hence represent the main background for the detection of neutrinos. At the same time, however, muons provide an excellent basis for measurements themselves. After a description of the simulations in Section 2 and a presentation of the machine-learning based selection used for selecting high-energy leading muons in Section 3, a measurement of the differential energy spectrum of high-energy atmospheric muons detected in IceCube and IceTop is presented and discussed in Section 4. The production of high-energy atmospheric muons depends on the energy E_{cr} of the primary cosmic ray inducing the extended air shower and the fraction of this energy that is transferred to the muon. We define this fraction as the effective Feynman- x in the laboratory system:

$$x_{\text{F,eff}}^{\text{lab}} \equiv \frac{E_\mu}{E_{\text{cr}}} \quad (1.1)$$

with the muon energy E_μ at its production in the atmosphere. A machine-learning approach for reconstructing $x_{\text{F,eff}}^{\text{lab}}$ combining information from IceCube and IceTop is presented in Section 5, followed by the conclusions and an outlook in Section 6.

2. Simulations

The starting point for all simulations used in this analysis are primary cosmic rays on the level of the atmosphere that are weighted to a model of the spectrum and composition of cosmic rays based on the available cosmic ray data. Here, the parametrization implementing the Hillas model with three populations and a mixed third population (H3a) [5] is used. The air shower development is then simulated using the CORSIKA [6] package with Sibyll 2.1 [7] for the high-energy and FLUKA [8, 9] for the low-energy hadronic interactions. The following simulation steps, including the propagation of the particles through the ice, the photon emission and the IceTop and IceCube detector simulations, are accomplished using standard IceCube software packages. Two different simulation types are used: standard IceCube simulations covering the five most important element groups H, He, CNO, MgAlSi and Fe over an energy range of $5 < \log_{10} E_{\text{cr}}/\text{GeV} < 11$ and with about 3.5×10^9 simulated showers. These simulations are used for the event selection described in Section 3 and the unfolding of the muon energy spectrum in Section 4. The second type of simulations uses a kill-threshold principle, where only showers that are capable of producing a

36 high-energy muon exceeding a certain energy and/or effective Feynman- x are propagated, leading
 37 to a better efficiency in simulating showers with a single high-energy muon. Also, on the contrary to
 38 the standard simulations, the kill-threshold simulations contain the electromagnetic component of
 39 the shower as well as the IceTop response, which are necessary for the machine-learning algorithm
 40 presented in Section 5.2.

3. Event Selection and Data Sample

41 In this section, the event selection used in Section 4 and 5 is presented. After cuts that ensure a
 42 minimum quality of the sample (Section 3.1), a machine-learning approach implementing a random
 43 forest [10] classification is described in Section 3.2. The data sample used in Section 4 corresponds
 44 to a detector livetime of 168.2 days, which is also chosen as the normalization of the simulations.

3.1 Minimum Quality Cuts

45 In order to obtain the desired sample containing high-energy events with successful reconstructions
 46 for direction and energy that traverse IceCube as well as IceTop, the minimum quality cuts in Table
 47 1 are applied to data and simulations.

No.	Cut	Purpose
(1)	$Q_{\text{tot}} > 1000$ photo-electrons	Select high-energy events
(2)	Directional reconstruction [11] successful	Required for (3)
(3)	$r_{\text{IceTop}} < 500$ m	Select events traversing IceTop
(4)	Energy reconstruction [12] successful	Muon energy proxy
(5)	$L_{\text{track}} \geq 720$ m	Remove short tracks

Table 1: Overview of the minimum quality cuts using the total charge Q_{tot} deposited in IceCube, the distance r_{IceTop} between the intersection of the trajectory with the surface plane and the center of IceTop and the track length L_{track} inside the detector (as determined by the energy reconstruction [12]).

3.2 Random Forest Classification

48 High-energy track events in IceCube originating from atmospheric muons usually contain a large
 49 number of muons. Since the number of muons in a muon bundle is not directly measurable it is
 50 difficult to associate the total measured energy in-ice to the true energy of a single high-energy
 51 muon. In order to ensure a good energy reconstruction, we define signal and background as the
 52 following:

$$\text{signal} \equiv \text{single muon event} := \frac{E_{\mu,\text{max}}}{E_{\mu,\text{bundle}}} > 0.5, \quad (3.1)$$

$$\text{background} \equiv \text{muon bundle event} := \frac{E_{\mu,\text{max}}}{E_{\mu,\text{bundle}}} \leq 0.5, \quad (3.2)$$

53 with the energy $E_{\mu,\text{max}}$ of the most energetic muon in the muon bundle and $E_{\mu,\text{bundle}}$ as the total
 54 energy of the muon bundle. Muons with an energy $\gtrsim 30$ TeV at the surface will almost always be

55 the leading muon in the shower (compare [13]). The correlation and ratio of reconstructed and true
 56 energy of the most energetic muon in the shower for single muon events after the minimum quality
 57 cuts are shown for the standard simulations in Figure 1.

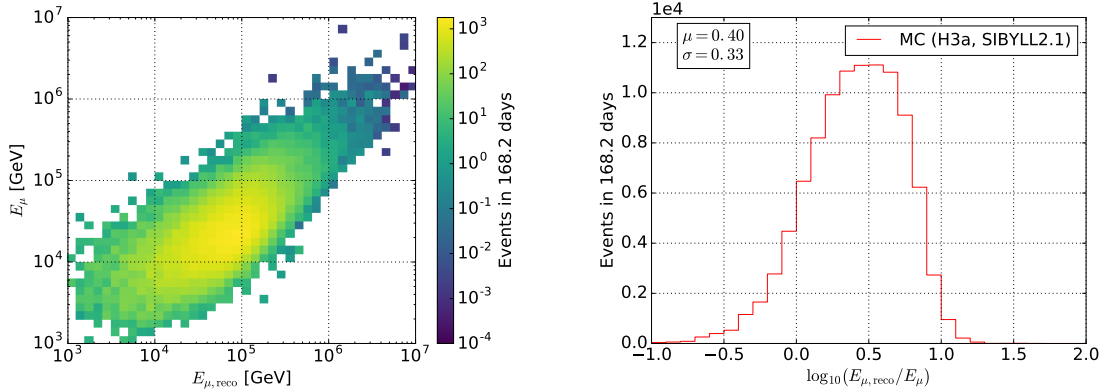


Figure 1: Correlation (left) and ratio (right) of reconstructed and true energy of the most energetic muon in the shower for single muon events after the minimum quality cuts using standard simulations.

58 The Pearson product-moment correlation coefficient between true and reconstructed muon energy
 59 is $r_{\text{Pearson}} = 0.75$ with the mean of the ratio on a logarithmic scale $\mu = 0.40$ and the standard
 60 deviation of the distribution $\sigma = 0.33$. In order to obtain a sample of single muon events, the
 61 standard simulations are used to train a random forest classifier that separates between single muon
 62 events and muon bundle events. Before training the model, two additional straight cuts on the
 63 ratio $q_{\text{max}}/Q_{\text{tot}}$ between the maximum charge q_{max} deposited in a single digital optical module
 64 (DOM) divided by the total charge Q_{tot} deposited in IceCube and on the direct length L_{dir} of the
 65 track given by DOMs that are hit within a certain time window around the first hit of an event are
 66 applied. The first cut, $q_{\text{max}}/Q_{\text{tot}} < 0.4$, removes events where the total brightness in the detector is
 67 dominated by a single DOM and which are not appropriately described by simulations. The second
 68 cut, $L_{\text{dir}} > 440\text{m}$, ensures a decent track reconstruction. For the random forest classification, the
 69 implementation from scikit-learn [14] is used. The random forest is trained using 16 attributes,
 70 200 estimators and 4 features per node. The resulting separation power can be seen in Figure 2 for
 71 the standard simulations after the minimum quality cuts and the two additional cuts described in
 72 this section. For a score $\gtrsim 0.5$ the sample is dominated by single muon events. In order to ensure
 73 the robustness of the model, a 5-fold cross-validation yielding values for purity and efficiency
 74 depending on the chosen cut on the random forest score is implemented; the resulting values can
 75 be seen in Figure 3.

4. Differential Energy Spectrum

4.1 Unfolding

76 Whereas for the differential energy spectrum of atmospheric muons their energy at production in
 77 the atmosphere is of interest, the muon energy is actually measured in-ice. In order to account
 78 for effects like a limited energy resolution and stochastic energy losses during the propagation

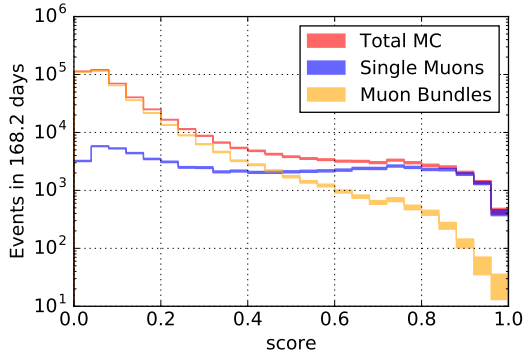


Figure 2: Distribution of the classification score for the standard simulations after the minimum quality cuts and the two additional cuts described in this section.

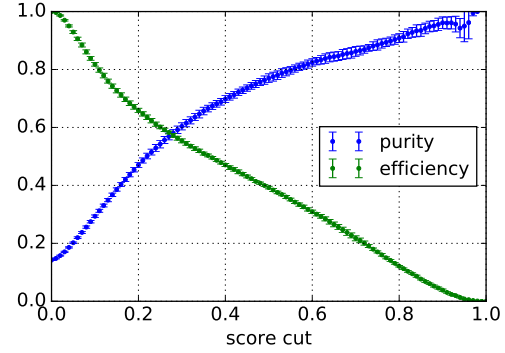


Figure 3: Result of the 5-fold cross-validation of the random forest model showing purity and efficiency as functions of the chosen cut on the random forest score.

79 of the muons through the ice, the resulting spectrum of the observed muon energy is unfolded
 80 using the software package TRUEE [15]. The unfolding is applied to the data after applying a cut
 81 (score > 0.55) on the output score of the random forest from Section 3.2, resulting in a purity of
 82 $(79.7 \pm 1.3)\%$ and an efficiency of $(35.1 \pm 0.5)\%$. The unfolding is performed in 9 logarithmic
 83 energy bins with five bins per decade in the energy range $3.8 < \log_{10} E_{\mu}/\text{GeV} < 5.6$ and uses the
 84 three observables $E_{\mu,\text{reco}}$, L_{dir} and θ_{zen} . The chosen parameters for the unfolding are 4 degrees of
 85 freedom and 9 knots. These parameters determine the strength of the regularization (see [15] for a
 86 detailed discussion) and were found to work well. In order to estimate the uncertainty of the result
 87 due to limited statistics in the simulations, the unfolding is repeated ten times using resampled
 88 simulation datasets, yielding an uncertainty σ_{MC} , which is then combined with the statistical error
 89 σ_{stat} to obtain the overall uncertainty in each bin:

$$\sigma_{\text{stat/MC}} = \sqrt{\sigma_{\text{stat}}^2 + \sigma_{\text{MC}}^2}. \quad (4.1)$$

4.2 Acceptance Correction

90 Only events that trigger IceCube and pass all selection steps are represented in the final sample and
 91 thus represented in the unfolded spectrum. In order to correct for the limited acceptance due to
 92 these effects, an external simulation dataset [16] is used for obtaining the surface flux predicted for
 93 Sibyll 2.1 in the zenith range that is covered by the sample after applying all cuts ($\cos \theta_{\text{zen}} > 0.88$).

4.3 Spectrum

94 The unfolded datapoints with errorbars $\sigma_{\text{stat/MC}}$ compared to different predictions and a previous
 95 all-sky result can be seen below. Figure 4 compares the datapoints to the simulated conventional
 96 muon flux at the surface from [16], a semi-analytical prediction for the prompt contribution to the
 97 muon flux based on the model by Enberg, Reno and Sarcevic [17] using the reweighting approach
 98 discussed in [13] as well as a best-fit linear combination of these two contributions. Figure 5,
 99 on the other hand, compares the unfolded datapoints ($\cos \theta_{\text{zen}} > 0.88$) to the best-fit power law
 100 from [13] describing the average all-sky flux above approximately 15 TeV. The difference in the

101 normalization between the result presented here and the result from [13] can be explained by the
 102 zenith dependency of the conventional flux, which is in good approximation inversely proportional
 103 to $\cos \theta_{\text{zen}}$ [13].

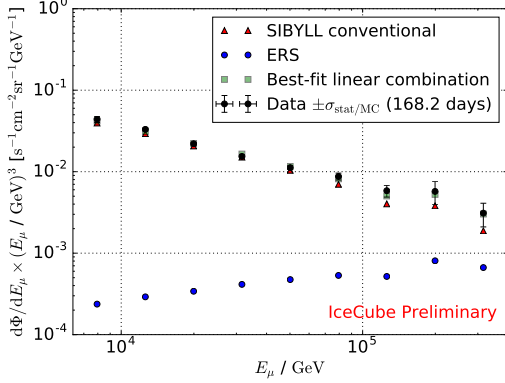


Figure 4: Plot showing the unfolded datapoints (black points), a prediction for the conventional flux from [16] (red triangles), for the prompt flux based on the model from [17], using the reweighting described in [13] (blue points), and the best-fit linear combination (green squares). All datapoints describe the flux in the zenith range $\cos \theta_{\text{zen}} > 0.88$.

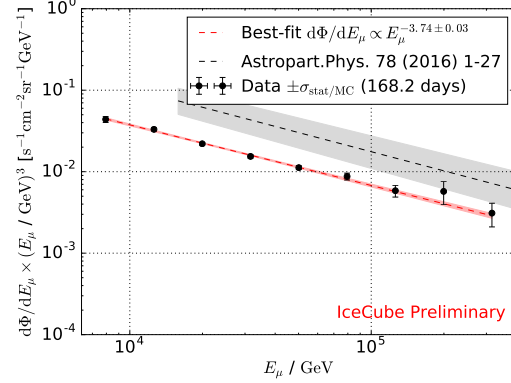


Figure 5: Plot showing the same unfolded datapoints as in Figure 4 (black points), a best-fit power law describing the data (dashed red line) and, for comparison, the best-fit power law from [13] for the average all-sky flux (dashed black line). Shaded areas indicate the uncertainty of the fit parameters (for [13] this includes systematic uncertainties).

104 The unfolded data points are also fitted to a power law with the best-fit in the zenith range $\cos \theta_{\text{zen}} >$
 105 0.88 and the energy range $3.8 < \log_{10} E_{\mu}/\text{GeV} < 5.6$ as the following:

$$\frac{d\Phi}{dE_{\mu}} = 9.0_{-0.3}^{+0.3} \times 10^{-17} \text{ s}^{-1} \text{ cm}^{-2} \text{ sr}^{-1} \text{ GeV}^{-1} \times \left(\frac{E_{\mu}}{50 \text{ TeV}} \right)^{-3.74 \pm 0.03},$$

106 with $\chi^2/\text{ndof} = 3.6/7$. In order to compare the datapoints against the conventional and prompt
 107 predictions in Figure 4, a superposition of the form

$$f(E_{\mu}) = a_{\text{conv}} \times \left(\frac{d\Phi}{dE_{\mu}} \right)_{\text{conv}} + a_{\text{prompt}} \times \left(\frac{d\Phi}{dE_{\mu}} \right)_{\text{prompt}}$$

108 is fitted to the data. The best-fit result yields $a_{\text{conv}} = 1.05 \pm 0.03$ and $a_{\text{prompt}} = 1.58 \pm 0.91$ with
 109 $\chi^2/\text{ndof} = 6.0/7$.

5. Effective Feynman-x

5.1 Phase Space

110 In Figure 6, the phase space in true Monte-Carlo variables with respect to primary cosmic ray
 111 energy and effective Feynman-x and after the minimum quality cuts is shown for single muon
 112 events (left) and muon bundle events (right).

113 Single muons, carrying most of the energy in the bundle, are also found at larger values of the effective
 114 Feynman-x ($x_{\text{F,eff}}^{\text{lab}} \gtrsim 10^{-3}$) and small primary energies ($E_{\text{cr}} \lesssim 10^8 \text{ GeV}$). Muon bundle events,
 115 on the other hand, are shifted towards higher primary energies and smaller effective Feynman-x.

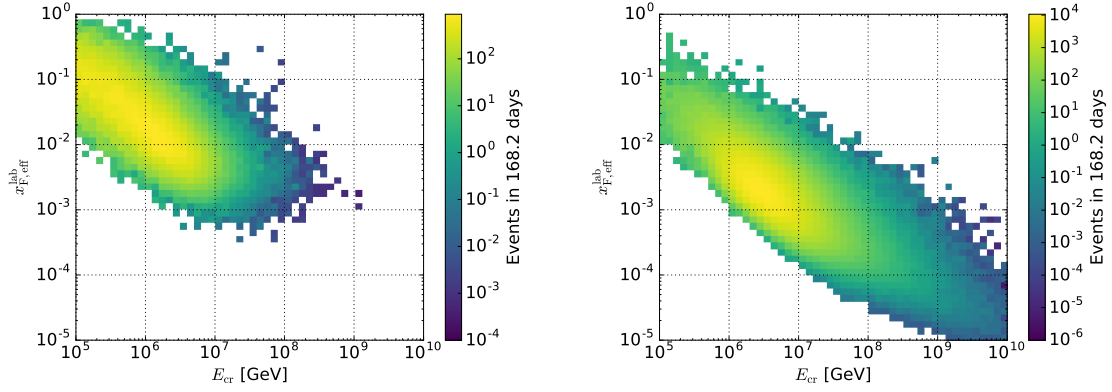


Figure 6: Phase space in true MC variables primary energy and effective Feynman- x for single muon events (left) and muon bundle events (right) for the standard simulations after the minimum quality cuts.

5.2 Reconstruction

116 The effective Feynman- x of atmospheric muons is reconstructed using a machine-learning based
 117 regression. The regression is trained using the dedicated simulations described in Section 2 after
 118 applying a cut (score > 0.8) on the output score of the random forest from Section 3.2, resulting
 119 in a purity of $(90.8 \pm 1.5) \%$ and an efficiency of $(12.1 \pm 0.3) \%$. Again, the implementation from
 120 scikit-learn [14] is used, employing 23 overall features, 400 estimators and 6 features per node. The
 121 resulting correlation and ratio between reconstructed and true effective Feynman- x can be seen in
 122 Figure 7. The Pearson product-moment correlation coefficient of true and reconstructed effective
 123 Feynman- x is $r_{\text{Pearson}} = 0.62$ with the mean of the ratio on a logarithmic scale $\mu = 0.11$ and the
 124 standard deviation of the distribution $\sigma = 0.27$.

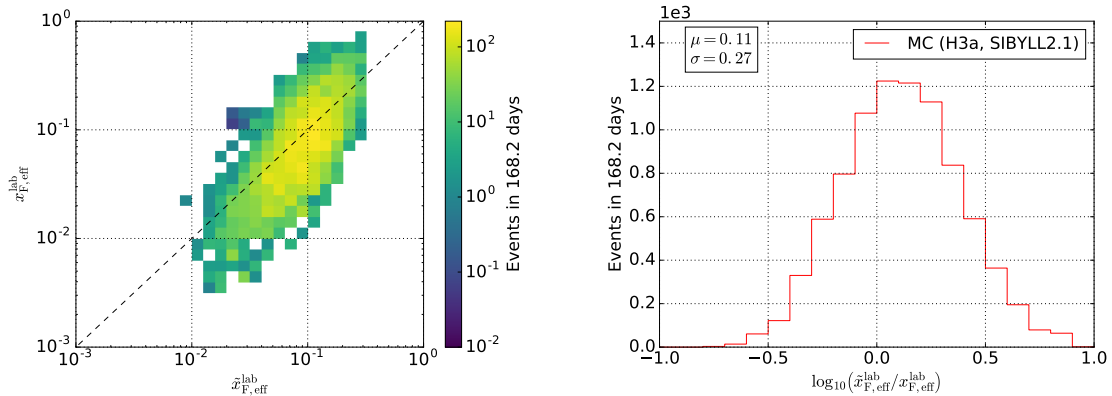


Figure 7: Correlation (left) and ratio (right) of reconstructed and true effective Feynman- x after the minimum quality cuts, the additional cuts described in Section 3.2 and a cut on the random forest classification score (score > 0.8) using the dedicated simulations described in Section 3. The dashed black line in the left plot indicates a line through the origin.

6. Conclusion and Outlook

125 High-energy atmospheric muons were studied with respect to their differential energy spec-
 126 trum and the fraction of energy they take from the primary cosmic ray. The differential energy
 127 spectrum in the zenith range $\cos \theta_{\text{zen}} > 0.88$ and the energy range $3.8 < \log_{10} E_{\mu}/\text{GeV} < 5.6$, us-
 128 ing 168.2 days of detector livetime, was found to follow a power law with $d\Phi/dE_{\mu} \propto E_{\mu}^{-3.74 \pm 0.03}$,
 129 which is in agreement with the all-sky result from [13]. A linear combination of conventional
 130 (Sibyll 2.1) and prompt (ERS) predictions was fitted to the unfolded data points, yielding $a_{\text{conv}} =$
 131 1.05 ± 0.03 and $a_{\text{prompt}} = 1.58 \pm 0.91$ as best-fit multiples of these predictions. The stated un-
 132 certainties are statistical only and do not contain systematic effects. A multivariate method was
 133 presented, capable of reconstructing the fraction of the primary cosmic ray energy that is trans-
 134 ferred to the most energetic muon in the shower with a correlation coefficient of $r_{\text{Pearson}} = 0.62$ and
 135 the standard deviation of the ratio of true and reconstructed values $\sigma = 0.27$. In the future, these
 136 studies will be extended by using more data, by increasing the effective livetime of the simulations
 137 and by studying systematic uncertainties on the hadronic interaction models, the mass composition
 138 of cosmic rays, ice-properties and the snow effect on IceTop.

References

- [1] **IceCube** Collaboration, M. G. Aartsen et al., *J. Instrum.* **12** (2017) P03012.
- [2] **IceCube** Collaboration, M. G. Aartsen et al., *Science* **342** (2013) 1242856.
- [3] J. I. Illana et al., *Astropart. Phys.* **34** (2011) 663–673.
- [4] A. Fedynitch et al., *Eur. Phys. J.* **99** (2015) 08001.
- [5] T. K. Gaisser, *Astropart. Phys.* **35** (2012) 801–806.
- [6] D. Heck et al., *Tech. Rep. FZKA 6019* (1998).
- [7] E.-J. Ahn et al., *Phys. Rev.* **D80** (2009) 094003.
- [8] T. T. Böhlen et al., *Nucl. Data Sheets* **120** (2014) 211–214.
- [9] A. Ferrari et al., *CERN 2005-10 (2005), INFN/TC 05/11, SLAC-R-773* (2005).
- [10] L. Breiman, *Mach. Learn.* **45** (2001) 5–32.
- [11] J. Ahrens and et. al., *Nucl. Instr. Meth. Phys. Res.* **A524** (2004) 169–194.
- [12] **IceCube** Collaboration, R. Abbasi et al., *Nucl. Instr. Meth. Phys. Res.* **A703** (2013) 190–198.
- [13] **IceCube** Collaboration, M. G. Aartsen et al., *Astropart. Phys.* **78** (2016) 1–27.
- [14] F. Pedregosa et al., *J. Mach. Learn. Res.* **12** (2011) 2825–2830.
- [15] N. Milke et al., *Nucl. Instr. Meth. Phys. Res.* **A697** (2013) 133–147.
- [16] A. Fedynitch, J. Becker Tjus, and P. Desiati, *Phys. Rev.* **D86** (2012) 114024.
- [17] R. Enberg, M. H. Reno, and I. Sarcevic, *Phys. Rev.* **D78** (2008) 043005.